Title

PORE SHAPE, SIZE, GROWTH, ACTIVATION ENERGY, AND THE KINETICS OF STRUCTURAL CHANGES IN GLASS-LIKE CARBONS

Author

Henry, L.G.

Publication Date

1985-10-01

Lawrence Berkeley Laboratory
UNIVERSITY OF CALIFORNIA

Materials & Molecular Research Division

PORE SHAPE, SIZE, GROWTH, ACTIVATION ENERGY, AND THE KINETICS OF STRUCTURAL CHANGES IN GLASS-LIKE CARBONS

L.G. Henry
(Ph.D. Thesis)

October 1985

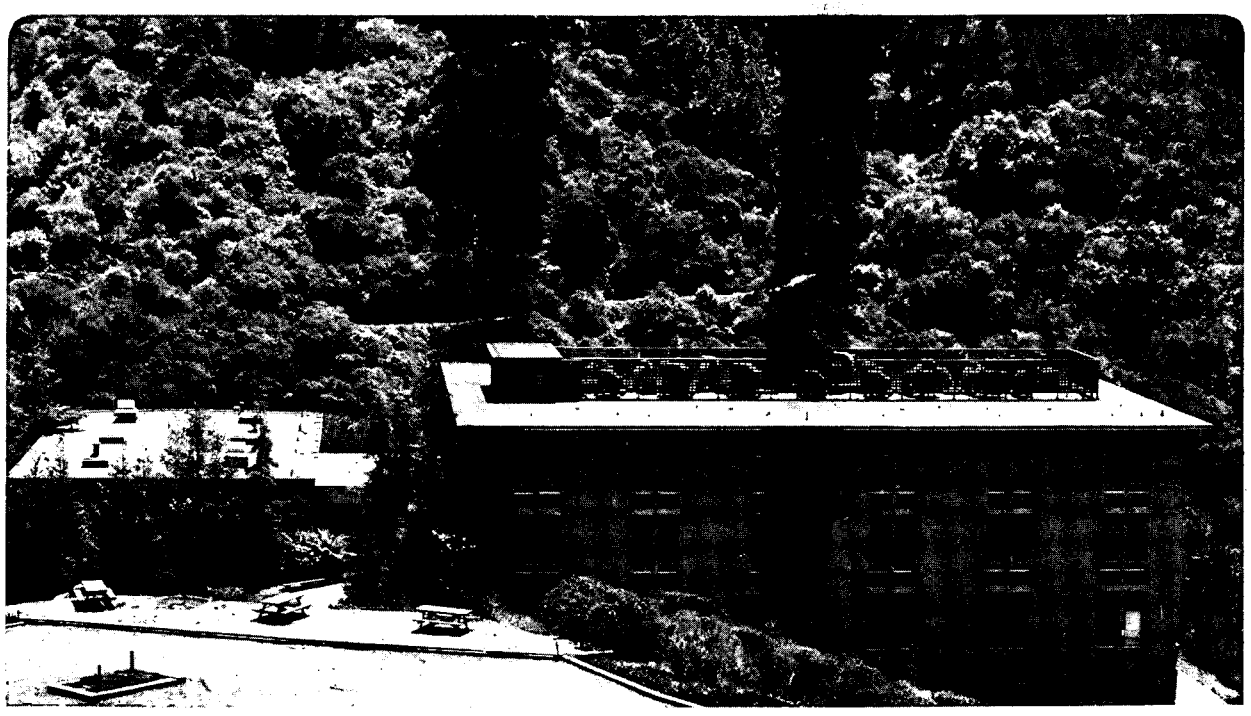

Prepared for the U.S. Department of Energy under Contract DE-AC03-76SF00098

DISCLAIMER

LBL-18021

Ph.D. Thesis

PORE SIZE, SHAPE, GROWTH, AND THE KINETICS OF STRUCTURAL CHANGES IN GLASS-LIKE CARBONS

LEO G. HENRY

Ph.D

IN

MATERIALS SCIENCE AND ENGINEERING

MATERIALS AND MOLECULAR RESEARCH DIVISION
LAWRENCE BERKELEY LABORATORY
UNIVERSITY OF CALIFORNIA
BERKELEY, CA 94720

July 1985

This work was supported by the Director, Division of Materials Sciences, Office of Energy Sciences of the the U.S. Department of Energy under Contract No. DE-AC03-76SF00098.

TO:

My MOTHER and FATHER, who insisted that I "go for the gold".

BERNADETTE, my wife, whose tolerance and patience made this thesis possible.

MALENE and NILAJA, my daughters, who did not quite understand what I was doing, but knew why I was doing it.

OTTO and EVELYN, my parents-in-law, whose encouragement was always present.

Berkeley, July 1985

CONTENTS

PORE SHAPE, SIZE, GROWTH, ACTIVATION ENERGY, AND THE KINETICS OF STRUCTURAL CHANGES IN GLASS-LIKE CARBONS

LEO G. HENRY

DOCTOR OF PHILOSOPHY
IN
MATERIALS SCIENCE AND ENGINEERING

MATERIALS AND MOLECULAR RESEARCH DIVISION
LAWRENCE BERKELEY LABORATORY
UNIVERSITY OF CALIFORNIA
BERKELEY, CA 94720

ABSTRACT

The pore size, shape, structure and coarsening in glass like carbon (GLC) samples heat-treated at temperatures (HTT) in the range 1000 to 2800°C and for heat-treatment times (HTt) up to 156 hours, have been investigated using small angle x-ray scattering (SAXS) and Wide Range x-ray Diffraction (WRXD), Wide Range Neutron diffraction (WRND) and total neutron scattering techniques.

Small angle x-ray scattering studies indicate that the pore size increases with both increasing heat-treatment temperature (HTT) and time (HTt) at and above 2000°C. Below 2000°C however, the changes are due only to temperature. The non-linetic changes in the pore size represented by the radius of gyration, parameter R_g, range from 9.0 to 23.7Å. The kinetic changes above 2000°C are analyzed using the theory of bulk diffusion controlled growth of precipitates modified for application to pore growth in GLC. The results show the expected $t^{1/3}$ dependence of R_g. The average Rg increases with HTT with

an activation energy of 76 ± 4Kal/mole, and confirms the hypothesis that vacancy migration is the mechanism governing the coarsening of the pore structure. The SAXS scattering data also indicated that the pores can be modeled as oblate ellipsoids, and that the axial ratio, $\nu(=b/a)$ only ranged from 0.30-0.25, that is, there is virtually no change in pore shape in the temperature range studied (1000-2600°C).

The WRXD and WRND results showed that in the range 1200 to 188°C HTT, $\bar{d}_{002}$ remained unchanged at 0.37 ± 0.003nm for heat treatment times up to 158 hours. Above 1800°C, $\bar{d}_{002}$ decreased but did not fall below 0.341 ± 0.003nm even after 4 hrs. at 2600°C. The defect free size L_a, and extent of layer stacking L_c, increased isothermally in the range 1200-1800°C, but both increased with time and temperature at higher temperatures reaching a maxima of 6.41nm and 2.15nm respectively at HTT of 2600°C. Between 1200°C and 1800°C HTT, the strain, ε decreased non-kinetically from 0.24 to 0.15, but at higher temperatures, the strain was also time dependent and decreased to 0.10 at 2600°C.

The total neutron cross-section (NCS) measurements showed that the ratio of hydrogen to carbon atoms ($n_H n_C$) decreased with increasing HTT and HTt, and the WAND data showed that the background, which is strongly affected by the presence of hydrogen, also decreases with increasing HTT and HTt. The NCS data also indicates that most of the hydrogen is lost when the HTT exceeds 2000°C. Between 1200 and 1800°C, n_H/n_C decreased from 0.036 to 0.020 and between 2000 and 2600°C there was a further decrease to 0.014.

A graph of $\overline{R}_g$ vs HTT at t = 0 shows that there are actually three regions of interest. Between 1200 and 1500°C, $\overline{R}_g(o)$ increases with HTT, a plateau is found between 1500 and 200°C, and at higher HTT, $\overline{R}_g(o)$ again increases monotonically. In the first region there is a rapid decrease in hydrogen content and thereafter the changes are much slower. The plateau is associated with the relief of stresses generated by the residual pyrolysis gases. In the region above 2000°C the changes are associated with annealing processes, and irreversible dimensional changes due to the large anisotropy in the thermal expansion coefficients. The mechanism of pore growth is associated with vacancy migration in the layer plane direction in the graphite-like layers.

1. INTRODUCTION

The progress of structural transformation in glass-like carbons (GLC) as a function of isothermal heat treatment time (HTt) can be followed by both Wide Angle X-Ray Diffraction (WAXD) and Small Angle X-Ray Scattering (SAXS) measurements made at room temperature. These GLCs are a convenient prototype of the class of non-graphitizable or hard carbons, so called because they do not attain the graphite structure (Fig. 1.1.A) even after exposure at extremely high temperatures (~ 3000°C) and very long times (~ 150 hrs). They are made mainly by the pyrolysis of thermosetting resins such as polyfurfuryl alcohol, phenol formaldehyde and phenol benzaldehyde [1-5]. The material is very brittle (K_{IC} = 10.5 $Mm^{-3/2}$ x 10^{-5}) [6-8], mechanically hard (1-3GN/m^2 DPH) [1,9], strong (40 - 60 MN/m^2 ultimate tensile strength) [1,16-18], impermeable (10^{-6} to 10^{12} cm^2/sec in He) [13-15] and has a chemical inertness and oxidation resistance greater than that of graphite [1,16-18]. Currently, its principal commercial uses are as a material for heating elements, crucibles, susceptors, electrodes, electron gun or filaments, in biomedical implant applications and as a glaze to cheaper impure carbon or graphite and refractory parts [19-23]. A more complete review on such properties and uses are to be found in an LBL publication by Baker [24].

Microscopically however, the GLC structure resembles that of graphite [19] (but there are significant differences as discussed later). The fact that the WAXD profiles (Fig. 1.2.B) of the material is dominated by SAXS was first demonstrated by Bragg and Hammond [25].

Further SAXS analyses showed that the material obeyed Porod's [26-28] Fourth Power Law for heat treatments above 2500°C, and showing a positive deviation [29-33] from the law at lower temperatures < 2500°C.

The broad and diffuse peaks observed in the Wide Range Diffraction (WRD) patterns (Fig. 1.2.B) correspond to the (00l) reflections in graphite, and the (hk) bands found in disordered carbons [2,52-56]. All these studies concur with the model proposed by Jenkins et al. [1]. The material is seen (Fig. 1.2.A) to consist of ribbons or laths of highly strained and defective turbostratic carbon of apparent crystallite size (defect free distance) in the range 15 - 50Å. These laths twist, turn, split - and - join, and interlace with each other to form closed slit-shaped pores of radius of gyration, R_g = 10-20Å in size. Some indication of the shape and sizes of these pores have been found using lattice imaging from transmission electron microscopy [2,34-38]. These images were observed for temperatures above 1800°C (Fig. 1.3-1.6) using the 002 reflection [38].

Both WAXD and SAXS data has been used extensively to measure such parameters as the average interlayer spacing, $\bar{d}(002)$, defect free distance ("crystalite size") L, radius of gyration, $\bar{R}_g$, and Specific Surface, S_p (surface area per volume, S/V). Previous work [39-46] in WAXD analysis has shown that the profiles must be corrected before meaningful analysis can be made, and that these patterns contain only a few broad (00l) reflections and overlapping (hk) bands.

Preliminary investigations [47] of the structural changes in GLC materials took no account of the non-kinetic factors when the L_c (layer stacking size), and L_a (layer diameter) parameters were used to obtain an activation energy, ΔH, of 215 ± 40 kcal/mole. There have been no other reported studies of the kinetics of structural changes in GLCs, so far as this author knows.

Bose's [48] study of the closed pore structures in both soft and hard carbons fell short of investigating the temperature/time changes of pore size and/or pore growth as they are related to the radius of gyration parameter. Since pyrolytic Graphite (PG), a representative of graphitizable (soft) carbon, has oriented slit-shaped pores and has been interpreted in terms of a theory of scattering by oriented ellipsoids [Bragg et al. [49]], it seems likely that the same could be applied to the GLC materials, where the slit-shaped pores are oriented in all directions. No attempt was made to analyze the data from R_g, and analysis for surface area (S/V) was performed only for temperatures above 2000°C, resulting in an activation energy, ΔH, of 64 ± 10 kcal/mole [48].

Bose et al.[50] did not analyze their R_g data because it was felt that there was an ambiguity associated with R_g where the meaning of pore shape is not simple. Hoyt and Bragg [51] however, attempted a pore growth analysis using the R_g parameter, from GLC samples heat-treated at 1600°C, 1800°C, and 2500°C. They obtained an activation energy of 53 kcal/mole, and their analysis indicated that R_g should be proportional to t (time) to the 1/3 power. However, no correction

was made for the non-kinetic temperature factor, nor for the added intensity component resulting from the density fluctuations [29-32] within the matrix of the carbon material. These fluctuations have been shown to increase with disorder, that is, with decreasing HTT, and are especially large at temperatures below 2500°C.

The purpose of this research is to investigate the low temperature (< 2000°C) region for non-kinetic and/or kinetic structural changes and to analyze the kinetic changes above 2000°C. Specifically, it is intended to determine not only the changes in (001) reflections and (hk) band d-spacings, and the apparent "crystallite" sizes (defect free distances) L_c and L_a, but also the changes in pore size and pore shape as a function of both heat treatment temperature (HTT) and time (HTt). The kinetics of the pore growth are to be analyzed to obtain an activation energy using R_g, and the results compared with that previously obtained using S/V analysis. Fortuitously, the comparison of the x-ray and neutron diffraction data have revealed a heretofore unappreciated role of hydrogen in affecting the structural properties of the GLC.

2. THEORETICAL BACKGROUND

2.1 WIDE RANGE DIFFRACTION (WRD) PROFILES

Compared to the narrow reflections obtained from well ordered graphite, where the interlayer spacing d_{002} is equal to 0.335nm, the diffraction profiles of disordered carbons such as GLCs are broadened because the lattice spacing are not so well defined and the correlation distance is small. The 00l reflections are also displaced towards smaller diffraction angles, and the hkl reflections are replaced by hk bands which are also displaced toward large angles. The hkl peaks do not appear because the disordered graphitic sheets do not possess the ideal ABABA... stacking sequence. As discussed below the diffraction patterns must be corrected [41-46] before analysis can be made for the structural parameters, such as interplanar d-spacings and "crystallite sizes", L. These corrections although applied to both X-ray and Neutron diffraction patterns, are much more extensive for the x-ray data. Ideally the profiles must be corrected for instrumental distortions, for distortions caused by the penetration of the x-rays deep into the body of the specimen, for the incoherent (Compton) background scattering and for the strong small angle scattering. The resulting profile is then multiplied by the appropriate trigonometric (Lorentz and polarization) factors. Finally, the correction is made for the variation of the atomic scattering factor across the broad peaks. The result thus obtained is the lattice interference function which can then be subjected to analysis for structural parameters.

2.1.1 GENERAL WRD THEORY

2.1.1.1 X-RAY CASE

For polycrystalline samples (disordered carbons) with broad reflections, the observed slit collimated X-ray intensity, $I_{(obs)}$ diffracted at any angle can be written as:

$$I_{obs}(2\theta) = [C_1 \times L_p \times ABS(2\theta) \times f^2 \times I_{corr}(2\theta)] + J_{saxs}(2\theta) + I_{air}(2\theta) + I_b(2\theta) \quad (1)$$

where

C_1 is a constant (defined in Appendix A);

L_p = $[(1 + \cos 2\theta)/\sin^2\theta]$ is the modified Lorentz Polarization factor [57];

$ABS(2\theta)$ = $[1-\exp(-2\mu \times t/\sin\theta)]$ is the absorption factor for reflection geometry [58]);

μ is the linear absorption coefficient for coherent radiation;

t is the thickness of the sample;

f is the atomic scattering factor (which also contains the Debye-Walker factor, $\exp(-2W)$.

I_b is the background scattering which can be written as $I_{bc} + I_{bi}$, the coherent and incoherent (Compton) background scattering respectively [59,137]).

J_{saxs} is the small angle x-ray scattering intensity for slit collimated intensity.

I_{air} is the intensity due to air scattering [60,61].

I_{corr} is the corrected interference function which contains the desired information such as d-spacings, "crystallite" sizes, strain broadening and lattice defects.

2.1.1.2 NEUTRON CASE

For the neutron case, the profile equation has been discussed by several authors [62,63,161,162] and the observed intensity can be written as:

$$I_{hkl}(2\theta) = [I_A \times C_2 \times (1/(\sin\theta \times \sin 2\theta) \times C_3 \times C_4 \times (j \times N_C \times B \times F^2)/(\sin\theta \times \sin 2\theta) \times I_{corr}(2\theta)] + I_{sans}(2\theta) + I_b \quad (2)$$

where

C_2 is a constant (defined in Appendix B)

$I_{hkl}(2\theta)$ is the diffracted intensity of the peak assuming that there is no overlap between the reflection profiles.

I_A is the intensity for negligible absorption

A is transmission or attenuation factor

C_3 is $= \exp(-\mu\, xt/\sin\theta) \times \exp(-2W)$

C_4 is $= (2/B) \times [(Ln/Pi)^{1/2}] \times \exp[-(4Ln2/B^2) \times (2\theta_1 - 2\theta)^2]$

t is the thickness of the specimen

μ is the linear absorption coefficient

$\exp(-2W)$ is the Debye temperature correction factor

j is the multiplicity factor

N_c is the number of unit cells per unit volume

F is the structure amplitude factor per unit cell

$2\theta_i$ is the Bragg position of the ith reflection

B is the full width at half maximum intensity (Caglioti et al. [163]).

I_b is the background scattering.

When the experiment is conducted in an evacuated system there is no air scattering, and since neutrons do not possess a charge, there is no electromagnetic interaction and hence, except for magnetic samples there is no polarization factor. The background, b is determined by interpolation across the base of the diffraction peak [161,162]. The factor is independent of scattering angle [63] in contrast to the rapid increase with atomic number for x-rays, and the change with scattering angle [57,64], that is, the form factor for neutron scattering is a straight line dependence with scattering vector, $Q = (\frac{4\pi}{\lambda} \cdot \sin\theta.)$ The above equation is related to the geometrical arrangement where a parallel-sided slab of material is placed in the symmetrical transmission position to intercept adequately the whole of the monochromatic beam. In some cases, the samples are enclosed in a thin metal box, (usually of aluminum) which produces negligible absorption and scattering.

For both methods however, inaccuracies will arise due to incomplete separation of the peaks or to a rapid variation of background intensity (x-ray case) in the region of a diffraction peak. An example of the latter problem is the scattering in GLC where hydrogen is responsible for the high background (above instrumental) in the neutron case, but in the x-ray case, carbon atoms produce the incoherent (2θ dependent) scattering. This is discussed further in Sections 2.3, 3.3, 4.3, and 5.1.

2.1.2 ANALYSIS OF X-RAY LINE PROFILES

X-ray diffraction (XRD) line profiles from crystalline materials are usually narrow and thus fairly simple to analyze, and the experimental procedure has been standardized [58]. However, GLCs do not give sharp peaks, the incoherent background scattering is significant [64,71], and the strong contribution from the small angle scattering which makes the 002 peak very asymmetric has been reported by several investigators [25,29-32,65-68]. This material, a non-graphitizable carbon, has a diffraction pattern with very few 00l peaks and hk bands, all of which are very broad. They are so distorted that the profiles must be corrected before an analysis can be made in terms of the contributions of particle size, strain, and other defects to the broadening of the line profiles.

A modified version [41,71] of the systematic procedure [39], for obtaining distortion free line profiles is used. The use of reflection geometry requires an extremely long sample when obtaining data in the small angle region. In addition, theory assumes the use of a parallel beam so a divergent beam (experimental) contributes to the distortion of the data. The x-ray beam also penetrates the low density GLC samples to an appreciable depth causing a displacement of the x-ray patterns (low specimen absorption) towards smaller angles [69,70]. The use of flat samples of finite length combined with slit-collimated divergent beams therefore reduces the available irradiated volume and causes a departure from focusing conditions; therefore, at certain small angles, some of the incident x-ray beam misses

the sample completely and intensity is lost [41]. The angular distribution of the intensity scattered from air is continuous and decreases with $\sin\theta/\lambda$. Errors due to this air scattering, and the counting losses due to resolving time in the counters, must all be corrected for.

The sequence of corrections [41,71] used is as follows: correct for resolving time (counting losses), irradiated volume, air scattering, low specimen absorption, incoherent (background) scattering [137] and small angle scattering. The resulting profile is then multiplied by the inverse of the polarization factor and the inverse of the atomic scattering factor squared. Each peak is then multiplied by the appropriate Lorentz factor if the 00l peaks and hk bands do not overlap. For overlapping peaks, a "peel off" analysis (which includes using the appropriate Lorentz factor) must be performed. Details of analysis before "peel off" can be found elsewhere (Henry and Bragg [41]). The "peel off" procedure as it applies to GLC can be found in Section 2.1.4.

2.1.3 ANALYSIS OF NEUTRON PROFILES

Neutron diffraction line profiles from crystalline materials are much simpler to analyze than those from x-ray diffraction because, as stated earlier, for the neutron case there is no angular variation of the form factor, b (the nuclear scattering factor [62,63,72], but as in the x-ray case there is a temperature factor [130]. Since the wavelengths used, typically ranging from 0.1 to 10Å, are commensurate with atomic spacings in materials, thermal neutrons

diffract coherently according to the same Bragg law utilized for x-rays. For neutrons, the transmission method is used because neutrons are highly penetrating, and hence thick samples are needed for usable intensity. High vacuum conditions are employed to eliminate air scattering. Thus the only corrections needed before the "Peel off" analysis are for the background scattering, and for small angle neutron scattering (SANS). The polarization factor is non-existent and the absorption factor is negligible [63]). Whereas the SANS removal follows the same procedure as that for the SAXS removal, the background scattering, that is the incoherent diffuse background scattering caused by isotropic incoherence, and by spin incoherence, does not vary with scattering angle, and is removed by subtracting it from the raw data before the SANS has been removed [130].

2.1.4 "PEEL OFF ANALYSIS"

In order to study the intensity profile of any particular reflection, it is necessary to separate it from the total scattering curve [46]). The data is corrected (described in Section 2.1.2) up to and including both the atomic scattering factor and the polarization factor, but not the Lorentz factor. The "Peel off" procedure, which includes resolving the overlapping of the very broad reflections, is fully described by Short and Walker Jr., [46], and its application to one of the GLC samples is briefly described below. The procedure assumes: (i) that the (002) peak has zero intensity at about 10° 2θ on the low angle side. This has been shown to be so for many carbons;

(ii) that the intensity of the (hk) bands falls off to zero at some angle on the lower side of the peak given by the following equations developed by Warren and his co-workers [53,54]:

$$\text{(i) } A = 2 \times (\pi)^{1/2} \frac{L_a}{\lambda} (\sin\theta - \sin\theta_0) \qquad (3)$$

(ii) F(A) is some function of Å (analytical values for F(A) are tabulated in Appendix C.)

The position of the zero intensity is obtained when F (A) = 0. The high angle side of the (002) peak can now be obtained. This angle is obtained by multiplying the corrected intensity by $\sin\theta\ (\sin\theta=\sin\theta_0)^{1/2}$. The (004) peak is removed analytically, after which the (10) band is subtracted. This procedure is repeated for the (10) and (20) peaks. In this way, each peak is removed individually after which appropriate formulae for particle size can be applied to the pure diffraction curves.

2.1.5 INTERLAYER (001) and 2-DIMENSIONAL (hk) REFLECTIONS

The lattice and interlayer spacings, obtained from the angle at which the corresponding peaks are diffracted, are calculated only after each peak has been stripped (peeled) from the total profile, and has been made symmetrical by dividing through by the appropriate Lorentz factor. For the 001 profiles, this latter factor is $= 1/\sin^2\theta$. The $\cos\theta$ term has been dropped because it related to the line breadth [57]. For the hk bands, the Lorentz factor [53,54] is given by: $\text{Lorz1} = 1/\sin\theta(\sin\theta + \sin\theta_0)$ where θ_0 is the true position of the peak; but this applies to the low angle side of the

band. On the high angle tail of the two-dimensional reflection, the factor is given by: $Lorz2 = 1/\sin\theta(\sin^2\theta - \sin^2\theta_o)^{1/2}$. The d-spacings can now be calculated using the Bragg equation, $2d \sin\theta = \lambda$. Details of the above method of analysis as it relates to GLC was referenced and discussed in Section 2.1.4.

2.1.6 PARALLEL LAYER GROUP DIAMETER L_a AND LAYER GROUP THICKNESS, L_c

The crystallite size (defect free distances) in the c (height) and a (diameters) directions, can be obtained from measurements of the broadening of the appropriate diffraction peaks. The Scherrer (1918) expression $L = (K\lambda/(\beta_{1/2}\cos 2\theta)$ relating the crystallite size L, to the line broadening β, the wavelength, the angle of diffraction θ, and the Scherrer constant, K, is used throughout. The value of the constant K depends not only on the indices of the reflecting plane, but also on whether simple or integral line breadths are used, and also on the fraction of the peak height being used to measure the line breadths. These factors have been thoroughly investigated by Klug and Alexander [58], Randall et al. [74], and Warren [54] and are utilized throughout this dissertation. In summary, they reported that for the 001 peaks, K = 0.89 at half max peak height but = 0.57 at 3/4 maximum. For the hk bands, K = 1.84 for half maximum, K = 1.02 for 3/4 max and = 0.94 for 2/3 maximum.

2.2 SMALL ANGLE X-RAY SCATTERING (SAXS)

2.2.1 GENERAL SAXS THEORY

It is well established that interference effects in x-ray scattering at extremely small angles are due to diffraction from the small particles (homogeneities) in a solid matrix and is little affected by atomic structure (Guinier et al. [75]. However, it was Krishnamurti ([76]) who pointed to the strong scattering in the very small angle region from amorphous carbon materials such as charcoal, coke and anthracite. The same scattering was observed for dilute solutions of cane sugar, gelatin and colloidal dextrin, hence the scattering was ascribed to the randomly distributed sugar molecules. Because colloidal dimensions (10 - 10,000Å) are large compared to x-ray (wavelength = 1.548Å) the angular range is correspondingly small. In 1965, Bragg [25] reported the same small angle scattering phenomenon for the pores in glass-like carbons and for dilute solutions of silica solvents.

The basic assumptions are that the solution of identical particles of constant electron density must be dilute enough to eliminate interparticle interference such that each makes independent contributions to the total scattered intensity. Lord Rayleigh's [77a,b] equation considers particles having spherical symmetry:

$$I(h) = I_o\,(\Delta\rho)^2 * V^2 * \left[\frac{3\,[\sin(hR_o) - hR_o * \cos(hR_o)]}{(hR_o)^3}\right]^2 \qquad (4)$$

where $\Delta\rho$ is the electron density difference between matrix and particle (pore).

V is the volume of the particle.

R_o is the particle radius.

I_o is the incident beam intensity.

Guinier's (1938) postulate that the total scattering is simply the sum of the scattering from each particle for dilute systems was extended [75] to consider the case for the smallest angle (i.e. $h \rightarrow o$) called the Guinier approximation. Hence the above equation (4) becomes:

$$I(h) \underset{h \rightarrow o}{=} I_o (\Delta\rho)^2 x \exp(-h^2 R_g^2/3). \qquad (5)$$

It is easy to show that the radius of the spherical particle R_o, and the radius of gyration, R_g, are related, i.e., $R_g^2 = \frac{3}{5} R_o$. The Guinier approximation has been shown to be true regardless of particle shape and symmetry, and has a high angle limit of $hR = 2.0$, beyond which the approximation is not valid. A plot of log $I(h)$ versus h^2 gives a straight line at small h, the slope of which gives information about the geometry of the system and the size of that geometry. Specifically, R_g, which corresponds to the radius of gyration in mechanics, is the root mean square of the distances of all electrons from the center of gravity, and is therefore a measure of the spatial extension of the particle.

Porod [78,79] on the other hand, considered the intensity of the scattering at large angles, and arrived at an asymptotic law given by the equation:

$$I(h) \underset{h \rightarrow \infty}{=} [I_o(\Delta\rho)^2 \, 2P I^* S]/h^n \qquad (6)$$

where

h = ((4PI*sinθ)/λ) is the scattering vector

S is the total surface area of the interface between the phases,

n = +4 for point collimation (Porod's Law).

Rearranging:

$$h^4 I(h) = I_0(\Delta\rho)^2\ 2PI*S = K_p \qquad (7)$$

shows that the curve will asymptotically reach a constant value, the Porod Law Constant, K_p, which is proportional to the total internal surface area. The assumptions here are that the two phases are isotropic, of constant electron density (i.e. strictly invariant with the phase boundaries and sharp electron density transition from one phase to the other). Experimental demonstration of the above laws have been provided by several investigators (Van Nostrand and co-workers [28a,b], Debye et al. [27].

2.2.2 DENSITY FLUCTUATIONS

Perret and Ruland [29,30,80,81], in their SAXS studies of rayon-based carbon fibres, non-graphitizable carbons (NGC), pan-based fibres, and glass-like carbons, reported that although the Porod Curves [ln J_{obs} (h) versus ln (h)] tended towards a linear relation for higher values of h, none of the curves corresponded exactly to the h^{-3} (slit collimation), dependence. J(h) is the slit collimated intensity. Following the method of Schiller and Mering [82], Perret and Ruland [29] showed also that although the h^3 J_{obs} versus h^2 plots yielded a linear relation at higher h-values, the slope in this region was positive in-

stead of zero indicating that the experimental intensity curves had an added component which varied as h^{-1}. The fact that the exponents are higher than the theoretical value of -3 expected for sharp density transition between voids and the dense material indicates the existence of a component due to density fluctuations within the matrix. This deviation from Porod's Law they attribute to one dimensional density fluctuations produced by statistical variations of the size and shape of the layers in a given stack of graphite-like layers. They then modified Porod's Law Equation to include this added intensity, i.e.,

$$J_{obs}(h) = b_1 * h^{-3} + b_2 * h^{-1} \qquad (8)$$

where the first term, $b_1 h^{-3}$ is the well known Asymptotic Porod Law for large h, but the second term they attribute to the general constant diffuse scattering stemming from the general electron density fluctuations in the matrix. These fluctuations are thought to occur at greater than interatomic distances and in the direction of the parallel stacking of the layers. The constants b_1 and b_2 can be obtained from the intercept and slope of the plot. Subtraction of the term in h^{-1} will yield the corrected intensity, J_c for zero fluctuation in the carbon material.

In 1971, Ruland [83] showed that the finite width of the density transition produces negative deviations, while the density fluctuation within the phases produces positive deviations. He further argued that provided there is no correlation between the density fluctuation of one phase and that of the other, nor between the fluctuation of a phase and

the shape and size of its boundaries, the corresponding intensity components are simply additive to the SAS of the ideal system. Separation of these components have been shown previously (Luzzati et al. [84] to be experimentally feasible, and proved theoretically by Wendorff and Fischer [85].

Further quantitative determination of these effects have been shown to be feasible by Perret and Ruland [86] and Vonk [87]. That the intensity at relatively large h-values was due essentially only to the fluctuation component of the SAS was experimentally shown to be so by Ruland and co-workers [88-90]. The fluctuation component was separated from the scattering at smaller h-values by extrapolation of the I_{obs} versus h plot to h = 0. The resulting intensity without the fluctuation component was then multiplied by h^4 and then h^4 $(I_{obs} - I_{fl})$ plotted against h^2. They found that the presence of a finite width of the boundary region showed up at large h-values as a linear decreasing part of the plot. Similarly, the presence of density fluctuations should show up as a linearly increasing part of the plot. These fluctuations have been shown to decrease with increasing HTT for GLC by Perret and Ruland [30,90] and by Jenkins and Walker Jr.[32].

2.2.3 PORE SIZE, STRUCTURE AND COARSENING

The total pore volume in GLC has been found to depend only on HTT and not on HTt [50]. However, the pore sizes increase [25,92] and specific surface decreases [31,50] with both HTt and HTT. It has

been established that pore growth occurred by the migration of vacancies such that the larger pores grow at the expense of the smaller pores in the system. Here, the size and shape of the pores depend on the inherent strain present in the material with the high concentration of structural defects acting as excellent sinks for migrating vacancies. This is easily seen to be so since the pores are bounded by tangled and very low energy 002 crystallographic planes (graphitic laths). Hence, pore growth should depend on structural changes and reduction in strain energy more so than on overall decrease in surface energy, as was suggested by Bose et al. [50]. To test the Vacancy Migration Growth mechanism proposed by Bose and Bragg [50], Hoyt and Bragg [51] proposed using the change (with temp. and time) in average radius of gyration, R_g, of the pores in GLC. They suggested that the pore coarsening in GLC be likened to the steady state particle (precipitate) coarsening in alloy systems where such processes are controlled by volume diffusion compelled by the reduction of interfacial area (energy) between particles and matrix. Here, the coarsening rate is proportional to the inverse third power of time [rate α $1/t^3$], where competitive growth takes place among precipitates (of various sizes and shape) randomly dispersed in the matrix. The volume fraction of the precipitate directly affects the rate, and the density decrease due to mass loss, hence the total pore volume could remain constant with HTt, but will definitely change with HTT. In order to understand what changes are taking place, it is useful to consider the Liftshitz, Slyozov and Wagner (LSW) theory [93] of bulk diffusion which deals with controlled

second stage growth of precipitates in a super saturated alloy system. This is the same as steady state precipitate coarsening and the relationship can be written as:

$$(\bar{r})^3 - (\bar{r}_i)^3 = \frac{8\gamma DC_o\phi\ (t-t_o)}{9\nu RT} \qquad (9)$$

where

r is the average radius

r_i is the initial average radius

R = 1.987 kcal/mole, the gas const.

T is the absolute temperature in deg/Kelvin.

γ(erg/cm^2) is the interfacial energy between matrix and solute (isotropic assumption).

Co (mole/cm^3) is the equilibrium solubility of ppts or mole fraction in equilibrium with a plane interface

D (cm^2/sec) is the diffusion coefficient of ppt species.

ϕ (cm^3/mole) is the molar volume of solute or precipitate or pores

ν is the stoichiometric factor or weight fraction of solute particles.

The above theory is based on several assumptions:

(i) anisotropy is ignored and particles are assumed to be spherical.

(ii) interactions between grains are ignored since their dimensions are small compared with the mean distance between them.

(iii) fluctuation effects play a negligible part in the second stage of coalescence where the growth of the larger grains occur at the expense of the smaller ones.

(iv) elastic strain that results from a difference between the specific volume of the grains and the matrix are also ignored.

(v) solute atoms diffuse to the spherical particles under steady state condition. However, it must be noted that if the growth of a grain produces an elastic deformation on its surroundings, then there is an effect on the diffusion rate.

(vi) the volume fraction, ϕ of the dispersed phase is infinitesimally small.

Experimental evidence consistent with the above LSW theory was provided by Ardell and Nicholson [95,96,97] when they showed that the rate of the mean particle size increased with the third power of aging time. Because the experimental particle or pore size distributions were broader than the LSW theory predicted, Brailsford [10] Ardell and co-workers [95-100] all considered the volume fraction ϕ, that is, the diffusion geometry (radius of influence) around the particles. They found that the coarsening rate, r increases as ϕ decreases [98], but the basic rate ($\bar{r} \alpha t^{1/3}$) is maintained. This is called the MLSW theory [99]. This theory was later modified to consider the effect of encounters between growing pores (LSEM theory) where we have both direct contact between pores and a "welding" (particles joining) effect. These considerations have been found suitable for high ϕ) (up to ~0.5) and will reduce to the LSW theory at $\phi = 0$. Here again the basic rate ($\bar{r} \alpha t^{1/3}$) is maintained.

In general, growth originates from the concentration gradients existing around the particles caused by the thermodynamic demand, (Gibbs - Thomson equation) where the concentration at the surface of particles in equilibrium with large particles is lower than that with smaller particles. Since the solute atoms flow through these concentration gradients both from the surface of the smaller particles to the matrix and from the matrix to the surface of the larger particles we can say that the average radius of the particles (pores) changes. If we further assume that the pore shape remains the same (constant), and the interparticle distance >>2r, then $r = K \times R_g$, where K is a constant, and R_g, the electronic radius of gyration. We can rewrite equation

$$(\bar{R}_g)^3 - (\bar{R}_{g_o})^3 = \frac{8\gamma D \; C_o \; \phi(t-t_o)}{9 \; \nu \; K \; R \; T} \tag{10}$$

$$T[(\bar{R}_g)^3 - (\bar{R}_{g_o})^3] = K(D) \times D \times (t-t_o) \tag{11}$$

where

$$K(D) = 8\gamma C_o \phi / 9\nu KR \tag{12}$$

and

$$D = D_o \exp(-\Delta H/RT) \tag{13}$$

D_o is the diffusion coefficient.

$$\text{Hence } T[(\bar{R}_g)^3 - (\bar{R}_{g_o})^3] = K(D) \times D \exp(-\Delta H/RT)\,(t-t_o). \tag{14}$$

Thus the slope of plots of $T(\bar{R}_g)^3$ vs time when plotted vs 1/T would enable us to calculate the activation energy, ΔH. We can now write a differential type coarsening equation including all the above considerations:

$$\frac{d(\bar{r})^3}{dt} = \frac{1}{\nu} \times \frac{6\gamma DC_o}{KC_B RT} \tag{15}$$

where C_B is the atomic fraction of solute atoms in the precipitate

or

$$(\bar{r})^3 - (\bar{r}_o)^3 = K(\phi) \quad (t - t_o) \tag{16}$$

where $k(\phi)$, the rate constant $= \left(\frac{1}{\nu} \times \frac{6\gamma DC_o}{KC_B RT} \right)$

recall

$$\bar{r} = K(\bar{R}_g).$$

Finally

$$T[(\bar{R}_g)^3 - (\bar{R}_{g_o})^3] = K(\phi)\ D\ (t - t_o) \tag{17}$$

where

ν increases as ϕ decreases.

and

$\nu = \frac{27}{4}$ for $\phi = 0$, i.e. for steady state.

It can be assumed then that the kinetics of pore growth in GLC follows the modified LSW theory of diffusion controlled coarsening.

2.2.4 ACTIVATION ENERGIES IN GRAPHITE

Based on atomic interactions between the carbon atoms and the bond energies within single crystal graphite hexagonal layers, Diennes [104] proposed several mechanisms for the activation energy, ΔH, one of which incorporated self diffusion vacancies migrating parallel to the layers (basal planes), that is, perpendicular to the c-axis.

The theoretical value of this migration energy has been calculated to be 71.4 kcal/mole, and the vacancy formation energy was calculated to be 119.4 kcal/mole. These values were based on the Graphite's heat of sublimation value of 124 kcal/mole.Pauling [105]. Since these values were obtained using single crystal graphite, they are applicable only to volume diffusion. Diennes [104] ΔH values, re-calculated by Kanter [106] using the more reliable for the heat of sublimation (170 kcal/mole - Coulson [107], are ΔH = 93 kcal/mole for migration, and ΔH = 170 kcal/mole for formation. Coulson et al. [108] pointed out that the energy of formation for a single vacancy is not the same as the sublimation energy; an idea which previous investigators had used to arrive at their experimental values. Coulson's value for ΔH(= 10.74eV = 247.7 kcal/mole) is also based on the experimental sublimation energy (170.4 kcal/mole-Knight and Rink [109], but is much higher than previous values. It was pointed out however (Coulson and Poole, [110] that divancies are formed with energies release of approximately 4-6 eV and so previous values could be representative of divancy formation. Kelly [111] cited by Thrower [112] obtained a theoretical vacancy formation energy of 166 kcal/mole, and Nicholson et al. [113] extended the defect molecule formation vacancy calculations of Coulson et al. [103] to allow for symmetry relaxation around the vacancy. The value calculated was 8.75eV which is lower than that of Coulson, but higher than experimental estimation.

Experimental verification for the energy of vacancy formation has been attempted by Smoluchowski [114], Kanter [106], Rasor et al. [165], Baker et al. [115], and Nicholson et al. [113]. Their values ranged from 6.6 to 8.75 eV/atom (152.2 to 201.8 kcal/mole). On the other hand, the migration energies investigated by Felman et al. [120], Baker et al. [115], Henson et al. [119] and Thrower [112] ranged from 3.5 to 3.9 eV/atom (57.7 to 90 kcal/mole). Coulson and Poole [110] pointed to the fact that experimental values are lower than theory because divancies form with energy release of 4 to 6 eV/atom and hence are more stable than single vacancies. Bose et al [49,51] on the other hand obtained a value of 64±10 kcal/mole from specific area kinetics in GLCs.

2.2.5 SURFACE AREA

It was mentioned (Section 2.2.1) that the total surface area can be obtained from analysis of a plot of I_{saxs} versus h^n, however the actual calculation is not as straightforward as the equation below would suggest i.e.

$$h^4 I_{saxs} = I_o(h)*(\Delta\pi)^2*2\pi*S \qquad (18)$$

The product $h^4*I(h)$ reaches a constant value K_p, (the Porod Asymptote) at large h. In general, this equation is strictly valid only when the electron density transition at the interface is sharp (Porod [78,121]. This shows up in the $h^4 I(h)$ versus h plot as a zero slope at large h Schiller and Mering [82], Perret and Ruland [29,80]). The slope

is negative however if the interface is not sharp (Ruland [83,90]), that is, if there is a finite thickness between the phases, and positive if there are density fluctuations within the matrix (Perret and Ruland, [29,80,81,30], and Ruland, [83,90]. This has been discussed in Section 2.2.2.

Since most of the experimental intensity data are not obtained in absolute units, but in relative units, a surface area per volume, S/V is more easily interpolated from the data. Here, the integrated intensity, called the Porod Invariant, Q_p is related to the volume (Porod [78,121], that is:

$$Q_p = 2c(1-c) \int_0^\infty h^2 I(h)\, dh = 4\pi^2 * C(1 - C)\, (\Delta\rho)^2 * V \qquad (19)$$

where $C = (\rho_A - \rho_B)/\rho_A$ is the fraction of volume (occupied by the pores or particles) responsible for the scattering. Here, ρ_A is the theoretical density, and ρ_B is the density of the material. Combining and rearranging equations (18) and (19)

$$\frac{S}{V} = \pi * C(1-C) * \lim_{h \to \infty} - \frac{h^4 I(h)}{\int_0^\infty h^2 I(h)\, dh} \qquad (20)$$

and

$$S_p = \frac{S}{V} = \frac{\pi\ c(1-c) * K_p}{\int_0^{h_o} h^2 I(h) dh + \int_{h_o}^{h} h^* \frac{K_p}{4}\, dh} \qquad (21)$$

where h_o is the point beyond which Porod's Law is valid. Here K_p, the Porod Asymptote, is extrapolated from the plot of $h_4 * I(h)$ versus h^2, and Sp is the specific surface area.

The first integral in the denominator of equation (21) above is just the integrated intensity (area under the curve) of the plot of $h^2*I(h)$ vs h in the region h = o to h = h_o. The second integral, when evaluated can be written as: Integral = K_p/h_o, where h_o is the predetermined point from the $h^2*I(h)$ vs h plot.

From the above, it is seen that the surface area of any system can be obtained once the fraction of the volume (occupied by pores or particles) responsible for the scattering is known. The case for the particles or pores can be likened to Babinet's Light Principle of Reciprocity where the hollow in a sphere can be considered a phase. An example is GLC where the electron density contrast between the pores and the surrounding matrix is much stronger than the electron density variations within the matrix. Hence, the excellent scattering properties of the material.

2.2.6 PORE SHAPE

Bragg and co-workers [49,25,92,34] in their studies of the pore structure of PG and GLC, established that the pores in PG are oriented, oblate ellipsoids of revolution, and that those in GLC are closed and have sharp edges and corners. Further evidence for the shape and orientation in non-graphitizable carbons (NGC) produced from polyacrylonitrile is given by Perret and Ruland [29,23] when they showed that the scattering (after correction for density fluctuation) from the NGC materials [29] obeyed Porod's 4th Power Law up to relatively large values of h. This implied that the density transition

between the dense carbon material and the pores had to be sharp (width of zone < 0.3A). Hence they concluded that the pore walls are formed by planes of graphitic layers and are probably of irregular polyhedra shape. For Glassy Carbon however, they had [23] suggested that the shapes of the pores are needle-like with sharp edges. Earlier, Bragg et al [49] had shown that the number of voids in PG is about equal to the number of "crystallites". They concluded that since the voids probably occur in association with the "crystallites", then they most probably lie between the layers of "crystallites" and are probably pyramidal in shape.

Let us now assume that the pores in GLC can also be approximated to ellipsoids of revolution, mainly because the data shows that shape of the $h^4I(h)$ versus h^2 curve does not follow the theoretical scattering curve for spherical pores. Malmon's [123] calculations for the scattering by ellipsoids shows that the scattering is a maximum at zero angle and falls off rapidly as the angle increases, but in a manner characteristic of the shape of the ellipsoids. The original equation for ellipsoids derived by Guinier [75] and Roess and Schull [124] considered the scattering from an ellipsoid of revolution with semi-axes a_1, a_2, ν_A, where $\nu(= a_2/a_1)$ is the aspect or axial ratio, that is, the ratio of the semi-axes of revolution to the equatorial radius.

$$I(h) = \int_0^{\pi} 2\,[ha_1\,(\cos^2\theta + \nu^2\sin^2\theta)^{1/2} * \cos\theta\, d\theta. \qquad (22)$$

Numerical solutions have been obtained for several axial ratios by Guinier [75], Roess and Schull [124], Schmidt [126], Porod [127], and Mettelback and Porod [127]. Guinier however, demonstrated that the scattering curves from all particles with the same radius of gyration, R_g, have the same limiting shape as $h \dashrightarrow \infty$. This was experimentally shown to be so by Hamzeh and Bragg [124] and Bose and Bragg [125] in their work on PG.

Malmon, on the other hand, paid particular attention to the larger scattering vectors, h, by plotting I(h) as a function of $h\bar{R}_g$ where $\bar{R}_g = [(2 + \nu^2)/5]^{1/2} * a_1$. Here, a_1 is the smallest dimension of the ellipsoids in a system which satisfied the conditions of random orientation, mono-dispersity, and no interaction (dilute solution) between particles which consist of a single macromolecular species. In this way Malmon was able to show that the distinguishing features between oblate and prolate ellipsoids are to be found at the larger scattering vectors. For poly-disperse systems however, the scattering curve represents a weighted average of the scattering from each component. Hence, in the smaller angular regions, the intensity is weighted towards the larger particles, and towards the smaller particles out at the larger angles. Such scattering has been investigated by Roess and Schull [124], Schmidt and co-workers [127,128,129] for ellipsoids. Their calculations were for dilute solutions of uniform charge density particles. They inferred from the above that although the semi-axes are different in size, the axial ratio, ν, is the same for any solution.

Schmidt's [127] scattered intensity equation is

$$P_h(h,\nu) = \int_0^\infty Nn(R)*R^6*I(hR)dR \tag{23}$$

where Nn(R) is the distribution function of the equatorial radius R; the R^6 term occurs because I(hR) is proportional to the square of the particle volume. Integration and evaluation result in the following:

$$Po(h,\nu) = (1/5)\ (1 + X^2)^{-1}\ [(1 + \nu^2X^2)^{-2} + A(X)\ x\ T(\nu,X)] \tag{24}$$

where $X = 2h/a$

and $h = 4*\pi*\sin\phi/lambda$

a is a constant

$$A(X) = (1 + x^2)^{-1}\ [2 + 0.5X^2] \tag{24A}$$

$$T(\nu,X) = (1 + \nu^2X^2)^{-1} + (1 + X^2)^{-1}*D^{-1}\ *\tanh^{-1}D \tag{24B}$$

$$D(\nu,X) = X(1 - \nu^2)^{1/2}\ *(1 + X^2)^{-1/2} \tag{24C}$$

$$\tanh^{-1}D = 1/2\ *\ Ln[(1+D)/(1-D)]. \tag{24D}$$

The above equation then can be used for comparison against experimental results. The overall result however of the polydisperse nature of any system of ellipsoids is to average out the oscillations (which are dependent on the particle size) such that they become relatively small or completely absent not only as ν increases, but also as the scattering vector increases.

2.3 TOTAL NEUTRON CROSS SECTION

When neutrons encounter other atoms many reactions occur. These reactions depend on the cross section of the atoms and the energy of the neutron used. The transmission through the sample is simply the ratio of the intensity of the beam passing through sample I_s, to that intensity I_o incident on the sample. The intensity of the incident beam is reduced in passing through the sample because the incident neutrons are absorbed and/or scattered by the target particles. The total cross section, σ_T is given by

$$\sigma_T = \sigma_S + \sigma_A \tag{25}$$

where

σ_S is for the case where the neutron is simply scattered and re-emerges as a neutron

σ_A is when the neutron is truly absorbed with the production of quantum of radiation or some other particle.

The transmission T from any sample is related to the total cross section by the following:

$$\frac{I_s}{I_o} = T = \exp\left[-N(\Sigma_j * \sigma_j) * X\right] \tag{26}$$

where

X is the distance in the medium through which the beam has travelled.

N is the number of atoms per unit volume

$\Sigma_j * \sigma_J$ is the summation of the cross section coefficient of the various reactions which can take place.

$N(\Sigma_j * \sigma_j)$ is the linear absorption coefficient of the material at the given neutron energy.

For our carbon material (GLC), the cross section per unit mass σ/m is given by

$$(\sigma/m)_{tot} = K\ (\sigma_C\ n_C + \sigma_H\ n_H) \qquad (27)$$

where n_C and n_H are the number of carbon and hydrogen atoms per unit mass respectively; σ_C and σ_H are the total scattering cross section for carbon and hydrogen, and K is a constant to be determined using a sample where it is assumed that $n_H = 0$. From the above equation, the ratio n_C/n_H can be determined for the GLC sample.

The neutron cross section is not only atom dependent but also energy dependent. Hence according to Bacon [63] the neutron cross section for hydrogen compared to that for carbon is in the ratio of 170:1 for neutrons having a wavelength of 0.108nm (1.08Å) which corresponds to 0.07eV. Here σ_H = 81 barns and σ_C = 5.6 barns.

For the experiments done at ANL however, the energy used was 300 MeV, hence σ_C = 5.5 barns and σ_H = 25 barns. For the samples done at NBS (no energy was quoted), but σ_C = 4.8 barns (10^{-24} cm^2) and σ_H = 50 barns.

It is seen then that the amounts of hydrogen present in the sample obtained from cross section measurements can be determined semi-quantitatively, then related to the background scattering in the material as obtained from the wide angle diffraction data. This residual amount

of hydrogen that remains after carbonization or graphitization has been shown to be in the range 100–1000 ppm in carbons and 5 – 200 ppm in graphites (Meyer et al., [132]). It was also shown that the hydrogen content decreased with increasing HTT, but the materials had to be heated in the range 3700 – 4200°C to remove the remaining hydrocarbons.

3. EXPERIMENTAL PROCEDURE

3.1 PRELIMINARY: MATERIALS

The Glass-like carbon material used in this work was prepared by Polycarbon Inc., of North Hollywood, California under license from Lockheed Missiles and Space Corp., and received a final heat treatment temp(HTT) of 1000°C for one hour, thus removing most of the aromatics and other gases. However, some hydrogen is left. The material, received in plate form had an as-received bulk density of 1.53 gm/cm^3, and an interlayer spacing of 0.346 ± 0.003nm.

Specimens, nominally 5.0 x 2.5 x 0.2cm, were cut from the plate, weighed, measured for length, width and thickness, and scribed with gauge lines (Mehrotra Ph.D. thesis [133]). They were then heated in a vertically mounted Astro Graphite (Model 2560 - 1000) furnace which utilized a graphite heating element. The furnace was modified so that a graphite carousel could hold 10 samples at a time. The samples were fitted into vertical radial slots in the cylindrical graphite sample holder. The initial method, of holding the sample above the hot zone (which has a 200-300°C difference) until the heat-treatment temperature was reached, then plunging the carousel into the zone, was found to be unsatisfactory. Most of the samples either cracked or broke. Finally, the samples were held in the hot zone during the ramp-up time which is approximately 30 minutes to get to 1000°C. The temperature was measured with a disappearing filament optical pyrometer, and an automatic temperature controller was used to maintain the temperature to ± 10°C.

Heating rates were 15°C/min up to 1000°C, then 6-7°/min. above 1000°C. The samples were heated in the range 1000 -2600°C and for times up to 150 hours. Each sample was dropped from the hot zone (after the appropriate time) by specific incremental rotation of the carousel. The samples fell into a He-atmosphere quench chamber. Specimens were re-weighed, measured for length, thickness and width, then ground (on both sides to avoid warping) to 0.16cm thickness for maximum transmission during x-ray measurements. These were then hand polished using 600 grit papers (thickness tolerance of 0.0001). Details of the procedure including temperature control can be found elsewhere [134].

3.2 WIDE ANGLE X-RAY DIFFRACTION PROFILES

The wide ANGLE X-RAY DIFFRACTION (WAXD) experimental data were obtained with a General Electric XRD5 Diffractometer employing a copper tube (with large focal spot) at 45KV and 35mA in conjunction with a nickel filter pulse height discrimination. Collimation was provided by a 1° source slit, H.R. Soller slit, and 0.1° detector (receiving) slits. The samples were scanned in reflection in the range two theta = 1.0 to 160° with goniometer speed 0.2° per min; chart speed 0.06" per min, and time constant of 0.5sec. In the region below 8° two theta, all intensity measurements were made using fixed count ($N \geq 10{,}000$) and 0.1° two theta increments. At still smaller angles of 3° and less, correction for counting losses due to resolving time in the counters were done using multiple foils technique [58]. The air-

scattering, which has a continuous decreasing angular distribution with increasing sinθ [58], was obtained by measuring the air scatter in the absence of the specimen and multiplying the result by an appropriate geometric factor [60,61].

The incoherent x-ray scattering from the GLC samples were measured [59,135] at the largest scattering angle (150° 2θ) possible for the radiation (Cu K_α = 1.5418Å) used. The fixed count method was used, and the experimental details are to be found in [137] (see Appendix D for relevant equations). Results of the measurements on Pyrolytic Graphite and GLC 2700°C are shown in figures 3.2.A,B., and the extrapolated incoherent scattering down to zero angle is shown in fig. 3.2.C.

3.3 WIDE ANGLE NEUTRON DIFFRACTION

The neutron (wavelength = 0.719Å and 1.542Å) diffraction patterns were obtained at the National Bureau of Standards (NBS), Reactor Radiation Division. A resolution, ΔQ ($Q = 4\pi \sin\theta/\lambda$) was obtained using an annealed polycrystalline copper specimen. Data were collected from 5° to 105° two theta, using fixed count and using 0.2°, 2θ increments, then normalized to the total mount (weight) of sample present. The samples were normalized to the 1200°C sample, hence the 1800, 1200 and 2600° samples has the following multipliers: 1.09, 1.06, 0.847 respectively. These numbers represent the increase of the relative values thickness times the width for the sum of all samples at that annealing temperature. The length of each sample was essentially selected by the beam and was nearly constant for all cases. The data is first corrected for these factors before any analysis is done.

3.4 SMALL ANGLE X-RAY SCATTERING

3.4.1. APPARATUS: THE 10-METER SAXS CAMERA

The GLC samples, thinned to 0.16cm using a diamond wheel, were cut to 10mm squares, then taped over 1.0mm holes on a circular wheel in an automatic sample changer capable of exposing 12 samples per setting. Data were collected at the National Center for Small Angle Scattering Research (NCSASR) at the Oak Ridge National Laboratory. A 10-meter SAXS Fig. 3.4.A camera which utilized 1.54Å copper radiation from a rotating anode x-ray generator was operated at 35K and 30mA. The 10-meter camera also utilizes a PG crystal monochromator, pinhole collimation, and two-dimensional position sensitive proportional counter (electronic resolution 0.1 x 0.1/cm). Data from both the Guinier and Porod regions, were easily obtained because the SAXS camera was designed so that the focal spot-to-sample and sample-to-detector distances can each be varied in 0.5m increments up to and including 5.0m. This allowed a system resolution in the range 0.4 to 4.0 millirads. The beam size at the specimen was 0.1 by 1.0cm (fixed). The K range covered $3 \times 10^{-3} \leq K \leq 0.03 nm^{-1}$ (Cu Kα). The maximum flux at the sample is 10^6 photons/sec on sample-irradiated area of $0.1 \times 0.1 cm^2$. (45KV and 100mA). The background on the detector can account for up to 45 cps electronic noise distributed uniformly over the detector and the parasitic slit edge scattering typically was 20 to 160 cps, depending on the sample to detector distance, beam stop size and other factors. The experiments were done

at room temperature (about 21°C), under vacuum. The data were recorded in the memory of a minicomputer which had built-in program routines for automatic background and detector sensitivity corrections. For more details, see the NCSASR USERS Guide, [165]. The procedure for the reduction of the raw data before analysis is discussed in Section 3.4.4, and a schematic diagram of the relative positions of the detector, sample chamber, slits and source is shown in Fig. 3.4.B.

3.4.2 MEASUREMENT OF SAMPLE TRANSMISSION

The first set of data to be collected is that of the incident beam using the Special Carbon Black Standard,* $I_o = I_{carbon}$, with no sample in the beam. The x-ray generator voltage and current are set to 20KV and 10mA respectively. Intensity is measured for a period of about 100 seconds. Secondly, the samples are placed in front of the monochromator slit in the beam near the x-ray source, and the intensity measured, I_{csam}, for the same period. The x-rays are now switched off and the background intensity called the dark current, I_{dc}, is measured over the same period of time.

For weakly scattering systems, the transmission is given by:

$$T = \frac{I_{csam} - I_{dc}}{I_{carbon} - I_{dc}} . \qquad (28)$$

---

*Special Carbon Black Standard - material was impregnated with polyethylene.

The Carbon Black Standard is now removed from the beam (computer controlled) and the intensity re-measured for the sample alone, I_{sam}. If $I_{sam} > 0.10 \times I_{carbon}$, (as is the case for Carbon Black), the transmission must be re-calculated using:

$$T_{true} = \frac{I_{csam} - T_{carbon} * I_{sam}}{I_{carbon}} \qquad (29)$$

where $T_{carbon} = 0.50$

3.4.3 INSTRUMENTAL DATA

During data collection there are unavoidable contributions to the detector counts from cosmic radiation, parasitic scattering from collimation slits, and non-uniform efficiency of the detector. To correct for these, the following measurements are made: First, the background intensities of the "dark current" and "empty beam" are obtained. The "dark current" intensity, I_{dc}, is obtained with the x-rays off, and intensity collected for between 100 - 300 seconds. The "empty beam" intensity, I_{mt}, is obtained with the x-rays on, the carbon standard and the sample out of the beam, and intensity collected for the same time as above. If data is to be collected from a liquid or powder, the empty sample cell is used instead. The sensitivity intensity, I_{sens} is obtained using a radioactive isotope (Fe-55) in the sample chamber, with the x-rays off, and counting for longer times to improve statistical accuracy.

3.4.4 REDUCTION OF RAW DATA

The experimentally obtained data must be corrected for "dark current" and "empty beam" and then for the sensitivity variation of the detector. The empty beam is also corrected for dark current, and the sensitivity is corrected for empty beam and dark current, before both are used to correct the raw data from the samples.

The appropriate equation used to arrive at the corrected intensity, I_{samc}, is given by:

$$I_{samc} = [I_{sam} \times I^*_{sam}] + I_{dc} + [T_{sam}*(I_{mt} - I_{dc})] \qquad (30)$$

and

$$I^*_{sam} = [\, I_s*1000/MON_s - (I_{dc}*1000/MON_s)*(t_s/t_dc)]*1/I_{sens} - T_s/T_e\ (I_{mt}x1000/MON_{mt})-I_{dc}*1000/MON_{mt}*t_{mt}/T_{dc}\ ]*1/I_{sens} \qquad (30A)$$

where

I_s = intensity from sample

I_{dc} = intensity for the dark current (no x-rays).

I_{mt} = intensity for no specimen (x-rays are on).

T_s = transmission factor for the sample.

T_e = transmission for empty beam (taken as one).

MON_s = monitor counts for the sample.

MON_{mt} = monitor counts for the empty beam.

MON_{DC} = monitor counts for dark current.

t_s = time for sample data collection.

t_{mt} = time for empty beam data collection.

t_{dc} = time for dark current data collection.

and MONITOR counts are used for normalizing all the data for 1000.

3.5 NEUTRON CROSS-SECTION

The measurements of the total cross-sections of the GLC samples at four HTTs and one HOPG sample (no heat treatment) were carried out at the National Bureau of Standards (NBS) and also at the materials Science and Technology Division of Argonne National Laboratory (ANL). Neutron energy of about 300MeV was used for both sets of samples. At this energy, carbon has a total cross section of 5.5 barns and for hydrogen, it is 25 barns. Since the diffractometer is not calibrated in an absolute sense, the cross section was compared to a known standard in order to interpret them. It was assumed that the highly Oriented Pyrolytic Graphite (HOPG) sample was pure carbon ($n_C = 0$) and hence used as the standard.

4. EXPERIMENTAL RESULTS

4.1 X-RAY DIFFRACTION PROFILES

4.1.1 RAW DATA

Figure 4.1.A shows the uncorrected Wide Angle X-Ray diffraction (WAXD) intensity profiles from a GLC sample heat-treated at 1800°C (GLC1800). It was found that the uncorrected pattern of GLC1800-0(i.e., 0 hours) was indistinguishable from those taken at 4, 6, from those taken at 4, 6, 9, 15, 24, 48, 72, 96 and 100 hours, that is, no change in structure discernible at this HTT for all times. Hence Fig. 4.1.A is representative for the HTT of 1800°C for all times up to 100 hours. As is the case for the 1800 sample, the patterns for each of the temperatures 1600, 1400, 1200 and 1000°C were indistinguishable as a function of HTt up to 156 hrs, but each HTT was distinguishable from the others. These non-kinetic changes have been reported by the author [42] at the 16th Biennial Carbon conference, and as far as this author knows, such behaviour below 1800 has not been reported previously.

When the HTT is increased, there is a narrowing of the 002 profiles and a shift in the peak position towards higher angles (fig. 4.1.B). This is consistent with simultaneous "crystallite" growth and strain relief. There is even more profile narrowing for changes in HTT starting at 2000°C as is easily seen from comparing the width at the half maximum positions of the two profiles. Comparison of fig. 4.1.C (i)

and (ii) for 2200°C shows that there is a kinetic factor at this HTT. Table 4.1.A, column 3, shows an increase in the 2θ position and correspondingly, a decrease in d_{002}, (see column 4), for the 002 peak between 1200 and 1800°C for the raw data. However, this change is only apparent and is evident when we look at the corrected 2θ positions in column 5. There are some 2θ changes from 2000°C and up for both HTT and HTt but these changes are small, and do not in fact attain the expected turbostratic value of 3.44 A for d_{002}.

All the samples exhibit similar strong SAXS (seen in fig. 4.1.A) in the low angle region (that is below about 10°2θ). Figure 4.1.B shows that it decreases with increasing HTT and fig. 4.1C shows that it decreases with increasing HTt. A decrease in the SAXS contribution to the 002 peak is reflected in the change with both HTT and HTt in the Porod Slope (Col. 7, Table 4.1.A) from n = - 2.7 at 1200° to -3.6 at 2600°C.

The incoherent background scattering from the material (associated with carbon in the x-ray case) is seen to increase with scattering angle. This is shown here for 1200°C and 2600°C heat-treated samples (fig. 4.1.D). Results showing that measurements of incoherent scattering made directly on the GLC sample are essentially the same as the values obtained indirectly after measurements using pyrolytic graphite, are shown in figures 3.2.A and 3.2.B. Details of the experimental procedure and analysis are to be found in [71,137] and a summary in Appendix D1.

4.1.2 CORRECTED PROFILES

The x-ray patterns were corrected for only the 002 reflections and figs. 4.1.E,F and G show the results of these corrections from GLC samples at HTTs 1200, 1800 and 2600°C. These figures illustrate that the line width decreases with increasing HTT, and the tabulated data (Table 4.1.B) show that there is also a decrease with HTt. The 002 profiles were corrected up to and including the Lorentz Polarization factor L_p and for the atomic scattering factor, f. Figure 4.1.H, which shows the totally corrected profile for GLC 2600°C, was actually corrected for the polarization, and for the atomic scattering factor, f, but not for the Lorentz factor. This is because this latter factor is quite different for 001 and hk peaks [53,54,57] and each peak must be separated from the total profile before the appropriate Lorentz correction can be applied, [46].

4.1.2.1 INTERLAYER SPACINGS, d_{002}

Interlayer spacings for d_{002} obtained for the HTT range 1200° to 2600°C are summarized in Table 4.1.A. For the lower temperature range (between 1200 and 1800°C) there is no change with temperature or time (within experimental error) as is illustrated in fig. 4.1.I. This is similar to results obtained by Saxena [47], and the preliminary work done by Henry and Bragg [40]. These spacings (0.347 ± 0.003nm) appear to be larger than the 0.340nm generally considered characteristic of turbostratic carbons at the onset of graphitization. At an above 2200°C however, we see a decrease in the interlayer d-spacing not only with temperature but also with time. It is to be noted however that

the interlayer d-spacings for the thick samples such as GLC2000-6, GLC2000-72, GLC2200-0 and GLC2300-48 do not fit exactly on the plot, exhibiting larger average values than expected. However, these results were determined using the 002 reflections and not from the higher angle reflections for which the accuracy is much higher. Thus it is considered that below 2000°C, the interlayer spacing in GLC is that of turbostratic carbon.

4.1.2.2 INTERLAYER STACKING SIZE, L_c

Line width (peak broadening) measurements and (interlayer) basal plane stacking, L_c (002 peak) are summarized in Table 4.1.B. The increase in L_c from 11.2Å at 1200° to 24.6Å at 2600°C can be indicative of both crystal growth and strain decrease. The percentage difference between the raw data and corrected data decreases from 21 percent at 1400°C to 8 percent at 2600°C. The raw 002 peak for the 1200°C sample was not sufficiently resolved (NSR) for a half maximum or even a three-quarter maximum of the peak to be determined. The figure 4.1.J shows that there are three regions of growth or strain relief: The first is a non-linear increase occurring between 1000 and about 1500°C; the second is the plateau-like region between 1500 and about 2000°C, and the third is the almost linear increase above 2000°C. Similar to the behaviour shown for the d-spacings, the interlayer stacking sizes for 2000-6, 2200-0, 2200-72 and 2300-48 are smaller than expected and do not fit exactly on the plot of L_c vs HTT. These samples are about twice the thickness of the other samples. It was further found that at and about 1800°C, L_c did not change with HTt, but above 2000°C, there were changes with both HTT and HTt.

4.2 NEUTRON DIFFRACTION PROFILES

4.2.1 RAW DATA

The uncorrected wide angle neutron diffraction (WAND) profiles for six GLC samples heat-treated at 1000°C for 24 hours (1000 -24), 1000-64, 1200-150, 1800-100, 2200-36, and 2600-4 are shown in figs. 4.1.K and 4.1.L. The features are the same as those found for x-rays except in two important aspects: (i) the neutron diffraction profiles provide more data in that the (10), (11), (20), and (21) bands are observed (compared to only the (10) and (11) for x-rays) using the CuK_α radiation, (ii) the backgrounds for the neutron profiles are much higher than those from x-ray profiles of the same sample. There is also considerable decrease in background with increasing temperature (fig. 4.1.L) and time (fig. 4.1.K). The superimposable nature of profiles from samples heat-treated at the same temperature up to 1800°C is illustrated for GLC1000 (fig. 4.1.K (i) and (ii). The difference in the background is seen at large $Q(= 4\pi/\sin\theta/\lambda)$. The narrowing of the profiles and the increase in resolvable peaks (004 and 20) with increasing HTT is also seen (fig. 4.1.L). These low temperature non-kinetic changes in the neutron data were also reported by the author [42] at the 16th Biennial Carbon Conference. Table 4.2.A shows the expected increase in 2θ and decrease in d_{002} with increasing HTT. Here also, the expected graphitic value of 0.335nm for d_{002} is not attained even for the highest HTT (2600°C). It is to be noticed however that the interlayer spacing value obtained from d_{004}

is lower. The narrowing of the profiles is reflected in the increase in all the "crystallite" size parameters (Table 4.2.b) with increasing HTT from 8.1A to 20.9A for L_{002}, from 19.5A to 22.2A for L_{004}, from 21.1A to 38.3A for L_{10} and 17.3A to 28.0A for L_{11}.

The same small angle scattering features are also exhibited here, and the incoherent background (associated with hydrogen in the neutron neutron case) was expected and assumed to be constant with increasing angle since the scattering is isotropic.

4.2.2 CORRECTED DATA

The entire profile corrected only for SANS and background, for reasons explained earlier (Section 2.1.3) are shown in fig. 4.1.M to 4.1.P for HTTs of 1200, 1800, 2200 and 2600°C. The sharpening of the profiles is evidenced in the decrease of the width at half maximum with increasing HTT, and also in the increase in separation of the overlapping (004) from the (10) peak. This is also true also for the (11) and (20) peaks. The large decrease in background with increasing HTT is shown for the 1000 and 2500°C samples (fig. 4.1.Q), and with HTt is shown for the 1000°C sample (fig. 4.1.K). These profiles were corrected only for the small angle scattering.

4.2.3 "PEEL OFF" ANALYSIS

Four samples 1200, 1800, 2200 were corrected as described in Section 2.1.3 then each peak "peeled off" from the full profile (described in Section 2.1.4). The results of the "peel off" analysis

for the 1200 and 2600 samples are seen in fig. 4.1.R and 4.1.S. The 002 and 004 peaks exhibit the expected symmetrical shape, and the increase in profile sharpness with increase in HTT is no surprise, neither is the sharp fall off to zero intensity on the lower angle side of the 10, 11 and 20 minimum positions. The fact that the tails of these latter bands extend out to very large scattering vectors has been discussed and is expected. What is new here is the success of the "Peel Off" analysis as it applies to the GLC disordered structure. Such analysis has not been reported previously.

Interlayer spacings and line widths obtained from the above analysis are summarized in Tables 4.2A and 4.2B respectively. The expected decrease in the d-spacings is observed and it is seen that the expected turbostratic value of 3.44A for $\bar{d}_{002}$ is attained even for our lowest HTT of 1200°C. The fact that $\bar{d}_{004}$ produces values which are lower than $\bar{d}_{002}$ for the interlayer spacing cannot be over-emphasized, and similar results have been obtained by Karamura and Bragg [141] in their studies on Pyro Carbon and Pitch Coke [155]. What is also observed (Table 4.2.B) is that the L_A values of 28.2 to 50.0A (layer diameter sizes) are not much larger than the L_C values (layer stacking size) of 15.5A to 22.0A. However the graphitic d-parameters are not obtained even at the HTT of 2600°C. In fact, not even the turbostratic parameter of 3.40A is attained. What is attained however are the large changes in the parameters after the "peel off" analysis. The positive slopes of the size-strain graph (fig. 4.1.T) where $B_{1/2}\cos\theta$ is plotted vs $(h^2 + hk + k^2)$ is an indication of the amount of strain present in

the L parameters for the hk bands. The "peeled" off data for (004) and (20) could not be compared with the corrected data because the profiles were not sufficiently resolved (NSR) to be analysed. For the same reason the (20) peaks could not be used in the analysis for strain (slope) decrease with increasing HTT (fig. 4.1.S). The results (Table 4.2.B) show that 44 to 53 percent of the size parameter L_A is present as strain in the (11) peak, and 22 to 28 percent for the (10) peak. These results from GLC, and similar ones obtained on Pyro Carbon are the subject of two abstracts by Henry and Bragg, [154] and Karamura and Bragg [155] submitted to the 37th Pacific Coast Regional Meeting of the American Ceramic Society (1984).

4.3 RATIO OF HYDROGEN ATOMS TO CARBON ATOMS, n_h/n_c

The cross section per unit per mass σ/m for the various samples decreased with increasing HTT, but increased with increasing background. These results are tabulated (Table 4.3). The trend is to be expected since the total cross section is used to determine the species content; in our case hydrogen. The HOPG, sample is taken as the standard, (STD) i.e., $n_c = 0$, from which n_h/n_c for the other samples were obtained. Similar heat-treated (Ht'd) samples were sent to NBS, but the times were different. The above HOPG standard and σ/ms values were used to calculate n_h/n_c for these samples. The differences for the different times at any temperature were at least three orders of magnitude less than the difference between temperatures. These results indicate that the amount of hydrogen present in the GLC samples decreases with increasing HTT and HTt. These results also follow the same trend as the residual hydrogen found in carbons and graphites by Meyer et al. [132] over the temperature range 800 to 3000°C, by Mehrotra et al. [132] over the range 1000-2600°C, Redmond et al. [135] over the range 200-2000°C and Anderson et al. [136].

4.4 SMALL ANGLE X-RAY SCATTERING

4.4.1 POROD PLOTS

Figure 4.4A is a demonstration of the symmetry of SAXS from GLC. The data represents a computer printout of the 2-dimensional SAXS data using position sensitive detectors. The connected curves are iso-intensity contours which are circular and show that the scattering is approximately isotropic, i.e. of circular cross-section on the average. Similar results were found for PG specimens cut parallel to the disposition surface by Bose et al. [48,68,125,138,139]. Their data showed that for PG the scattering (perpendicular to the layer planes) is approximately isotropic (fig. 17, p. 63 of Bose's Ph.D. Thesis [48].

Figure 4.4.B shows the Porod scattering curves of lnI vs. ln h for GLC samples heat-treated between 1000°C and 1800°C. At each temperature the curves represent HTt of 0, 4, 8, 16, 25, 36, 72, 96 and 128 hours, that is, the curves for all times at any one temperature were all superimposable. This indicates that there were no changes with HTt at each HTT. At 2000°C and above however there are changes with both HTT and HTt. The changes in HTt are shown for GLC 2200 (fig. 4.4.C). The Porod slopes were found to lie between -3.0 and -4.0. The greater than -4.0 obtained, although a point collimated system was used, is shown to be due to the density fluctuation within the matrix of the carbon system. This will be dealt with in more detail in Sections 4.4.4 to 4.4.6.

4.4.2 GUINIER RADIUS OF GYRATION (R_g) PLOTS

Guinier Plots (ln I vs. h^2), are shown in fig. 4.4.D for the HTT of 2200°C and times of 0, 6, 15 and 48 hours respectively. These plots are as expected. The slopes increase non-linearly with increasing HTt above 2000°C i.e. the pores in the material are coarsening. The results of the average radius of gyration, $\bar{R}_g$, calculated from the slopes of these plots can be found in Tables 4.4.A to 4.4.O. They show that at 2000°C and above, $\bar{R}_g$ increases linearly with both HTT and HTt but below 2000°C, there are no changes (fig. 4.4.E). This suggests that below 2000°C there is non-kinetic growth, and at 2000°C and above, both non-kinetic and kinetic (but mainly kinetic) growth occurs. Very little attention has been paid to the non-kinetic growth region previous to this study, but the results are in agreement with non-kinetic changes in $\bar{d}_{002}$, the dimensional length, L_c (reported in other section of this thesis) and preliminary investigations of the surface per volume.

The linear relationship between the cube of the average radius of gyration $(\bar{R}_g)^3$ and HTt at each HTT is shown in fig. 4.4.F. Here again the same behaviour is seen: No change with HTt below 2000°C, but starting at 2000°C and above, there are large increases with HTt. Below 2000°C, the average radius of gyration at each HTT becomes the value at zero time ($\bar{R}_g$), [see Table 4.4.P], and the values range from 9.00A to 14.56A at 1800°C. The value at 1000°C is used as the standard and the initial value, $\bar{R}_{go}$. Above 2000°C each slope was extrapolated to the zero time value. The values ranged from 14.68A at 2000°C to 23.67Å at

2800°C. The change in $\bar{R}_g$ from 1000 to 1800°C (800°C difference) is 5.56Å, but the change from 2000° to 2800°C (also a 800°C difference) is 8.9Å. This shows a larger growth for the higher heat treatment temperatures.

4.4.3 ARRHENIUS PLOT

The following procedure for data reduction is necessary to arrive at the activation energy associated with the pore coarsening. The slopes, K(D) (Table 4.4.Q) of the linear relationships between the cube of the average radius of gyration, $(\bar{R}_g)^3$ and the HTt at each HTT (fig. 4.4.F) are multiplied by the corresponding Kelvin temperature. The log (base e) of the modified parameter $[T\ (\bar{R}_g)^3 - T\ (\bar{R}_g)^3]$ is then plotted against reciprocal Kelvin temperature [fig. 4.4.G]. An activation energy of $\Delta H = 76 \pm 4$ kcal/mole was obtained from the plot. This agrees, within experimental error, with the theoretical value of 71.4 kcal/mole obtained by Diennes [104] and lies well within the experimental range of 58 to 90 kcal/mole obtained by many investigators [112-119]. The present value however is higher than that [64 ± 10 kcal/mole] obtained by Bose et al. [48,91] from specific surface area data from similar glass-like carbons.

4.4.4 POROD ASYMPTOTIC PLOTS

Raw and corrected plots [$h^4 I(h)$ vs. h^2] for GLC 1800-100 and GLC 2200-60 samples are shown in fig. 4.4.H. All of the uncorrected data up to 2500°C show positive slopes at large scattering vectors, h instead of zero slopes. The zero slope is representative of the well

known Porod Asymptotic Law at high scattering vectors h, and the possitive deviations are a result of density fluctuations within the material. Figure 4.4.H shows the decrease in positive slope value as the HTT is increased, and illustrates that the zero slope is obtained at large h when the corrections are applied. When corrected (fig. 4.4.H) the plots are used to determine the Porod Asymptote, i.e. $K_p = [\lim h^4 I(h)]$, and hence the surface area per volume of the pore-matrix interface. The results show that K_p increased from 0.585 (cps/A^4) at 1200°C to 0.725 at 2600°C. The fact that the plots do not show any distinct peak maximum in the low scattering vector region is region is indirect proof that the pores in the material are not spherical. This is illustrated in fig. 4.4.I for the whole temperature of 1200 to 2600°C.

4.4.5 POROD INVARIANT CURVES

The surface area is obtained from a combination of the integrated intensity plot (of $h^2 I(h)$ versus h) called the Porod Invariant, Q_p, and the Porod Asymptote, K_p. The latter was discussed in the previous Section 4.4.4. The Porod Invariant is shown to increase with increasing heat-treatment temperature (HTT), with the profile becoming sharper, and the maximum shifting towards lower scattering vectors. Examples of the Porod Invariant are shown in fig. 4.4.J for GLC 1800 and 2200°C samples where Q_p = 2.44 and 6.68 (cps/A^3) respectively. Details of the analysis for the specific surface i.e. the surface per volume which ranged from 1104 m^2/cm^3 for 1200 to 513 m^2/cm^3 for 2600°C were discussed in Section 2.2.5.

4.4.6 PORE SHAPE CURVES

Figure 4.4.K shows how the intensity $h^4R_g^4I(hR_g)$ for oblate ellipsoids [$\nu(=b/a) \leq 1.0$] changes with the dimensionless scattering vector hR_g for $\nu = 0.35$ to $\nu = 0.10$. It is to be noted that there is no peak or maximum in the curve; such a peak would have indicated that the material contained strictly spherical and smooth particles (Tchoubar and Méring, [164]). Superimposed on these plots are the experimental data curves for GLC-1200, 2200 and 2600°C. These curves for GLC all lie between the curves for $\nu = 0.25$ and 0.30 indicating or suggesting that there is not much change, if any, in shape between 1200 and 2600°C. This is consistent with the results obtained by Bose et al. [48] for particles with sharp edges and corners.

4.5 $\bar{R}_g$, $\bar{R}_{go}$, $\bar{R}_{gi}$ AND L_o RELATIONSHIPS WITH BULK DIMENSIONAL CHANGES

The non-kinetic changes in the average radius of gyration, $\bar{R}_{go}$ ($=\bar{R}_{go} - \bar{R}_{goi}$) as a function of HTT shows a non-linear behaviour up to 2000°C (fig. 4.5.A), but becomes linear above 2000°C and up to 2900°C. Here $\bar{R}_{go}$ is the average value at HTt = 0 hours for any temperature above the processing temperature and $\bar{R}_{goi}$ is the average value for the processing temperature (1000°C in this case). The relative $\bar{R}_g$ changes ($\Delta\bar{R}_{go}/\bar{R}_{gi}$) as a function of HTT (fig. 4.5.B) are also non-linear below 2000°C and follows the same behaviour as that of the relative dimensional changes ($\Delta l_o/l_{oi}$) as shown in the same fig. 4.5.B. The data for the dimensional changes were taken from Mehrotra's Ph.D. Thesis [183], and plotted in this way so as to compare the results with the pore size data.

When the relative dimensional changes are plotted against the relative pore size changes, we see three distinct regions (fig. 4.5.R): A sharp initial non-linear increase, a plateau-like region, and a final linear increase above 2000°C. This same three-region behaviour is seen in the graphs which show the changes in pore size and dimension with HTT. What is even more striking is the plot (fig. 4.5.S) of the ratio of the relative changes in R_g to the relative dimensional changes, 1. The ratio is seen to decrease non-linearly with increasing HTT up to about 2000°C, then becomes flat (no change) out to 2600°C. Overall the plots exhibit the same three-regions behaviour indicating that more than one mechanism is responsible for the structural evolution of the pores between 1000 and 2600°C.

5. DISCUSSION OF RESULTS

5.1 NEUTRON BACKGROUND AND H/C

As noted in Table 4.3 we have shown that the amount of hydrogen in glass-like carbons (GLCs) decreases with increasing heat treatment temperature (HTT) and time (HTt). These results are similar to those found for other carbons and graphites (but using different methods) by previous investigators [132-136]. In the same way, it is shown that the strong background from the Wide Range Neutron Diffraction (WRND) data decreased with increasing HTT and HTt (Table 4.3). Analysis of the neutron cross-section data indicated that this strong background can only be coming from hydrogen, and must therefore be regarded as incoherent scattering. To this end we must recall that the neutron cross-section for hydrogen is about 170 times that of carbon. These results can be related to density and weight loss results of Mehrotra et al., [134]. This weight loss increase has been suggested to be due to the release of hydrogen and they showed that most of the weight loss occurred below 2000°C. These authors also studied the kinetics of the weight loss and found it to be consistent with the diffusion of hydrogen. Similar results have been reported by Causey et al. [140], for measurements from pyrolytic carbon. The latter authors suggested that because the activation energy for the diffusion is so high (100 kcal/mole) then the diffusion must be controlled by chemical bonding between the hydrogen and the carbon atoms. The negative heat of solution obtained from solubility results is clear indication that

dissolving the hydrogen in PYC is an exothermic process and therefore implies chemical bonding. It is not difficult then to conclude that the increased weight loss with increasing HTT directly reflects the loss of hydrogen and therefore a decrease in the incoherent background scattering with increasing HTT.

5.2 LATTICE AND INTERLAYER d-SPACINGS

The analysis of the crystalline (001) reflections shows that the interlayer spacings ($\overline{d}_{002}$ and $\overline{d}_{004}$) do not change in the temperature range 1000 to 1800°C even after extremely long times (156 hours). These non-kinetic changes have been associated with the presence of hydrogen by Noda and Kato [153] and others [134]. At 2000°C and above however, there is a sudden decrease in these d-spacings not only with HTT but also with HTt. It has been further suggested that the sudden decrease in hydrogen loss at this temperature is responsible for the beginning of graphitization in turbostratic carbons (Meyer et al. [132]). The analysis done for this investigation also shows larger d(002) values than is expected for turbostratic carbons, and confirms the earlier work done by this author (Henry and Bragg, [40,41]) on two GLC samples heat-treated at 1000 and 2700°C for 1 and 2 hours respectively. However, the "corrected" d(004) values are not only much smaller but agree with results which show that the graphitization has begun. The fact that higher order reflections should produce better lattice parameters is to be expected and have been demonstrated by Karamura and Bragg [41] in their experiments using Pyrocarbon (PYC) which had been heat treated in the range 1000 to 2600°C and up to 32 hours. It is to be noted also

that the interlayer d-spacings for the thick samples such as GLC2000-6, GLC2000-72, GLC2200-0 and GLC2300-48 did not fit exactly on the plot (fig. 4.1.I), exhibiting larger average values than expected. This same behaviour was found in the pore size, "crystallite" size, and density measurements. For the latter, both thin and thick samples were heat-treated for the same time, then the densities measured. Firstly, the average densities of the thick samples were much larger than those of the thin samples, and much larger than the experimental error. Secondly, some of the thick were then cut in two and others were thinned. The densities of the cut pieces were different from that of the original and different from the thin and thinned samples, and all differences were much larger than experimental error. This same behaviour has been reported by Fischbach et al [147] and Nadeau [148,149] in their density studies of several GLC materials. They showed specifically that the density of the surface layer was larger than the interior. It is suggested that the temperature difference (gradient) between the inside and the outside of the sample prevented uniform structural rearrangement across the thickness of the sample.

5.3 "PARTICLE SIZE" FROM PEAK BREADTH AT HALF MAXIMUM

The decrease in 002 line width (corresponding to increase in layer size) with increasing HTT for the temperature range 1000 to 2000°C (Table 4.1.B) is expected. The fact that there is no change with HTt in this range has been reported previously (Henry and Bragg, [42]). These changes then are non-kinetic. For the X-ray data, the higher order 004 peak was not sufficiently resolved even after correction (for

the 2600°C) for a calculation of the peak breadth to be useful without a "peel off" analysis. For the neutron data however, analysis after "peel off" showed that the line width for both the 00l and hk reflections decreased with increasing HTT. The corrected (extrapolated) layer diameter, L_a, which had values ranging from 47.1Å to 64.1Å, in the temperature range 1200-2600°C are larger (as expected) than the layer height, L_c with range 15.5Å to 22.0Å. This shows that layer diameter growth is greater (17.0Å increase) than the increase of 6.5Å in layer stacking. It must be noted here that although the L_{20} peak data did not fit on same straight line (fig. 4.1.T) as the data from the L_{10} and L_{11} peaks, the growth is about the same, that is, 1.44nm. It must be noted further that the latter parameters are associated with defect free distances in the material. This is because the concept of particle size has very doubtful meaning for this GLC material whose structure is polymeric. Because the material is made by carbonizing a thermosetting resin, there are no grain boundaries as we would find in a polycrystalline material.

5.4 STRAIN AND STRESS RELIEF

Analysis after "peel off" (Table 4.2.b) showed that 43 to 53 percent of the broadening in the size parameter, L_a is present as strain in the (11) peak and 22 to 25 in the (10) peak, that is, the strain decreased with decreasing reflection order. The percentage difference in strain decreased with increasing HTT (Table 4.2.b) from 28 to 22 for the (10), and 53 to 44 for the (11) and is smaller than the percentage decrease (100 percent in both cases) from (10) to (11), that

is, with increasing order of reflection. It is seen then that calculations using broadening for "crystallite" size analysis with the non-availability of a few orders of reflection can be quite incorrect.

Similar results have been obtained by Kawamura and Bragg [141] in their studies of the 001 changes in the less disordered carbons (soft) in the temperature range of 2300 to 2600°C. Their data included time-dependent temperature changes. Their time dependent analysis showed that only the 2600°C samples showed an immediate decrease of strain (slope of the plot of $\beta_c \cos\theta_c$ versus 1^2) from 0 to 10 hours. For the temperatures 2500, 2400 and 2300°C however, they reported an initial increase in the slope (strain) from 0 up to 32 hours for the 2300°C, 0 to 8 hours for the 2400°C and 0 to 2 hours for the 2500°C samples. Thereafter, the slope (strain) decreased. The indication here is that for temperatures below 2600°C there is an initial increase in strain for a small time, then at some later time, the strain is relieved.

Their data also shows that the 2300 and 2400°C samples all had the same extrapolated $B_c \cos\theta$ value for all times (i.e. $B_c \cos\theta = 0.0125$), hence L_c [$=k\lambda/B_c \cos\theta_c$] is approximately 110 Å (= 11nm). This indicates no change with time for these two temperatures for the interlayer stacking height. The particle sizes increased with time starting at 3 hours for the 2500°C sample. These extensive results mirror the results obtained by this author for the GLC samples where the L_c values from the x-ray data showed a plateau-like region in the temperature range 1800 - 2200°C (Table 4.1.B) and an increase at higher temperatures. However, no such region is seen for the L_a changes. It is seen then that the layer diameter grows at a much faster rate than the interlayer

stacking. It can be concluded that extensive time analysis should be done at each temperature before any definite conclusions can be drawn about the growth of the layers.

The fact that the broadening from the (20) band does not lie on the straight line plot for temperatures up to 2600°C can be partially explained. The background contribution to the peak in this region is extremely high. In addition, the 001 and hk peaks appear so close that there is considerable overlapping. Thus the 20 band line profile is likely to suffer from over removal of background.

5.5 SPECIFIC SURFACE AREA (S/V) ANALYSIS

The decrease in the specific surface area, S_p (= S/V, the surface per volume) for four GLC samples heat treated at 1200, 1800, 2200, and 2600°C, from 1066 to 513m^2/cm^3 is expected. This fundamental quantity is relatively independent of any size distribution and of the shape of the pores (Bose and Bragg [50]. This decrease in S_p ties in well with the increase in $\overline{R}_g$ (9 to 23Å) over the same temperature range, and shows that the smaller particles are the largest contributors to the specific pore surface value in the material. Alhough the decrease in S_p is nothing new, the values obtained are much larger than values from adsorption methods where the latter shows very little decrease in the specific surface with HTT. This confirms that the pores in GLC are closed to gas penetration. What is new here however is the fact that the intensity data has to be corrected for the density fluctuations [29-32] within the matrix before any analysis can be made. This is certainly true for the S_p calculation because the latter depends on the use of the data at larger angles where as the density fluctuations

contribution is almost 100 percent at the very small angles (Guinier region); however, this contribution is so small as to be totally negligible. This is illustrated in the Asymptotic and Invariant Plots (figs. 4.4.H and J) shown for the 1200 1800, 2200 and 2600°C samples.

5.6 PORE SHAPE ANALYSIS

When the theoretical curves for ellipsoids of revolution were fitted to the experimental results from the GLC samples, it was found that the pores in the samples can be approximated using the oblate ellipsoidal shape where the aspect ratio is less than one. Further evidence of the pore shape in GLC can be inferred from results from other carbons and GLCs reported by many investigators [2,34-38,47,142-145] using Transmission Electron Microscopy (TEM). The narrow range found for the aspect ratio (0.25 to 0.31) for the HTT range 1200 to 2600° is evidence that although the pore size ($\bar{R}_g$) increased 155 percent (9Å to 23Å) and the specific surface area, S_p or surface area per unit volume, decreased 60 percent (1104 to 513m^2/cm^3), there is little or no change in the shape of the ellipsoidal pores. This is to be expected because in the first place, the pores are assumed to be bounded by the layer planes. These planes have been shown to grow faster in the a-direction than in the c-direction. This is similar to the results found by Bragg et al. [49] for pyrolytic graphite. Preliminary experiments have also shown that all rotations of the specimens give results identical to those of the curves in fig. 4.4.A. This indicates that the inhomogeneity regions or pores causing the small angle scattering (SAS) are randomly oriented.

5.7 PORE SIZE ANALYSIS

The non-kinetic change in the pore size (as represented by the radius of gyration parameter, $\bar{R}_g$) has not been reported previously so far as the author knows. There is change however with increasing HTT. This constancy in size with time at each HTT in the temperature range 1000 to 1800°C can be related to the gas pressure mechanism observed by Mehrotra and Bragg [134]. The latter investigators reported that the mechanism is responsible for the volume expansion up to 1800°C. They further argued that above 1800°C the thermal stress mechanism is predominant. Hence we see pore size increases with both HTT and HTt, with the change being very abrupt at about 2000°C. This is reflected in the change in $\bar{\Delta} R_g$ (difference between the initial value (t = 0 hrs.) at each HTT and the initial value for the processing temperature which is approximately 1000°C in most cases) with increasing HTT (fig. 4.5.A). These changes are seen to be non-linear below 2000°C, and linear above 2000°C. Bulk dimensional changes show the same behaviour, and since it has been shown [143] that the dimensional changes are isotropic on a macroscopic basis, these can be related to the pore size. Since very little or no more hydrogen is released at each of these low temperatures no matter how long the time, this is further evidence for the gas pressure mechanism. In this region, increase in temperature increases the gas pressure, hence size increases due to the volume expansion only.

5.8 PORE COARSENING ANALYSIS

The coarsening of the pores with HTt and HTT of 1800° (fig. 4.4.F) can be associated not only with the gas pressure mechanism, but also to the added irreversible thermal expansion factor [134]. Although the analysis did not include time data, it is easy to see (fig. 5.8.A) that there are four distinct regions in their heating curves: (i) up to 1000°C, (ii) from 1000 to about 1400°C, (iii) from 1400°C to about 1800°C, and (iv) above 1800°C. Their results are similar to the results obtained by Sutton et al. [151] and Collins et al. [146] in their study on dimensional changes and expansion in carbons and graphite. These authors explained that the first region was the region of reversible expansion where the crystallite structure of carbon changes continuously and reverts to its original structure on cooling. At and above the second stage, the heating causes irreversible changes in the expansion. They even reported shrinkage between 1300 and 1600°C, and this coincides with the plateau-like region obtained for the changes in R_g between 1400 and 1800°C (fig. 4.5.A). The underlying difference in this temperature range is that the added strains created during heating are not all relieved on cooling of the material and these frozen-in strains remain until the material is heated up again to a higher temperature. In the third and fourth regions, there are sharp increases in slope and this indicates that there is an added factor above this temperature of about 1600°C. Since the weight loss [134] remains constant from 1800°C and up, and the gas pressure decreases with HTT, then the added factor must be due to the stress on strain in the material (Mrosowski (152]. The decrease in

strain on cooling after each (mentioned earlier in Sec. 5.4) for these GLCs provides added energy for the vacancy movement (migration) along the basal planes. The second source is the reduction in surface energy which allows carbons to migrate from the larger pores to the smaller pores. This is the same as vacancy migration from the small pores to the large pores, thus making the larger pores larger (pore growth).

5.9 ACTIVATION ENERGY FROM VACANCY MIGRATION

The activation energy of $\Delta H = 76 \pm 4$ kcal/mole obtained for the pore size changes in GLC with time at each HTT compares with the theoretical value for migration energy (71.4 kcal/mole) in graphite Diennes [104]. These are self diffusing vacancies migrating parallel to the layers (basal planes). Since the vacancy formation energy of 168 kcal/mole (Kanter, [106] and Thrower, [112] is much higher, then the value obtained during this work must be associated totally with the vacancy migration mechanism. This further confirms that the pore growth must have occurred by the migration of vacancies such that the larger pores grow at the expense of the smaller pores in the system. In this case the high concentration of structural defects acts as an excellent sink for the migrating vacancies. Based on the theory (Bragg et al., [49] that the pores occur at the "crystallite" boundaries in graphite, and therefore must occur in association with the "crystallites", it can be assumed that the same occurs for these GLCs. In the latter case however, the pores are bounded by highly strained tangled laths which release most of the energy (upon heat-treatment) required for the vacancies to move. This vacancy movement is made

easier because of the following concurrent process which Noda and Kato [153] observed when they heat-treated several carbon materials under very high pressure. These authors argued that during the dehydrogenation process, the carbon atoms which had been chemically bonded to the already released hydrogen, become relatively unstable, and are therefore easily displaced by an external force. This of course is the well known creep process or mechanism. In the studies being reported for this dissertation, the releases of stress with HTT becomes the "external" force, the creep rate increases with increasing HTT, and the pore coarsening will result because of the vacancy migration.

5.10 IMPLICATIONS OF THE NON-KINETIC CHANGES IN $\overline{R}_g$ AND $\overline{d}$

The non-kinetic changes in the pore size, $\Delta \overline{R}_{go}$ ($= \overline{R}_{go}-\overline{R}_{gi}$) exhibits the same behaviour (fig. 4.5.A) as macroscopic dimensional length, ΔL_o ($= L_o-L_i$) and the interlayer stacking height, L_c. The figure shows three regions: the linear high temp. (>2000°C) region, the plateau-like between 1600 and 2000°C, and the initial non-linear increase from 1000 to 1600°C. Below 1500°C where the gas pressure mechanism operates (Collins, [146] Mehrotra and Bragg, [134] and Fischbach [147]), the small change in pore size and expansion (length) is to be expected. It is suggested now that the plateau-like region represents a slowing down of the process or an actual contraction [146], and a need to overcome an energy barrier. The sudden increase in pore size above 2000°C implies overcoming this energy barrier. This same behaviour is seen not only for the non-kinetic length changes (fig. 4.5.A), but also for

the interlayer stacking height, L_c. All this can be related to the sudden decrease in d(002) also at this temperature (see Sec. 5.2). All this readily conforms to Meyer et al's. [132] suggestion that the expulsion of the last vestiges of hydrogen at about 2000°C is probably responsible for the beginning of graphitization in turbostratic carbons.

The non-kinetic rate of increase of the pore size is also seen to be less than that of the macroscopic length (fig. 4.5.A), and this implies that the gas pressure and the anisotropic thermal stresses affect the macroscopic dimensional changes less so than they do the microscopic changes. These changes can be related to the very little extra weight loss after 2000°C for these GLCs [134] and coincides with the conclusion that the gas pressure makes very little contribution at these higher temperatures (>2000°C). Since the $\bar{d}_{002}$ spacing decreases in this temperature range, then the strain relief must be responsible for the increase in the pore size, and the increase in macroscopic length. Hence the heating of GLC causes the relaxation of internal stresses in the lattice through plastic deformation which is accomodated in the pores. This has been observed in fine-grained tantulum tungstates by Holcombe [150] and in vitreous carbons and graphite by Sutton and Howard [151].

Below 2000°C however, there are two regions: The initial non-linear steep increase up to about 1500°C and the plateau-like area up to 2000°C. In situ thermal expansion results [134] (reproduced here for easy reference (fig. 5.8.A) also show four regions of heating, but only one for cooling; the latter resulting in a 3 percent permanent

expansion after cooling from 2700°C. The second region which corresponds to the first region of the pore size plot (fig. 4.5.A) can be attributed to the result of the large release of hydrogen gas which is responsible for the stress generated in the pores. This is in accordance with the conclusion [134] that below about 1500°C the density decrease and the strain relief can be explained by the gas pressure mechanism which is solely responsible for the volume expansion. Here the pore size increases are much larger than the dimensional increases, but there are no changes in the $\overline{d}_{002}$ spacing.

The plateau-like regions (1500 to 2000°C) of Mehrotra and Bragg's [134] thermal expansion curve must obviously represent a combination of the end of the gas pressure mechanism and the beginning of the anisotropic thermal expansion contribution. A closer look at their linear expansion curve suggests that the region between 1500 and 2000°C is different from that above 2000°C. The same plateau-like region is observed for the d_{002} data, the interlayer stacking size, and the relative dimensional data. The decreasing effects of the gas pressure induced volume expansion and the very little strain from the anisotropic thermal expansion at this temperature range are probably not enough to produce more than a slight increase in the pore size in this region. This is probably because most of the thermal expansion is recovered in this temperature region when the material is cooled for measurement. It can be concluded then that in this region there is not much overall strain relief and the change in parameters remains almost constant.

6. SUMMARY AND CONCLUSIONS

The structural evolution of the pores in glass-like carbons has been studied and shown to be a strong function of both heat-treatment temperature and time. Small angle x-ray data was used to provide information about the size, growth, and shape of the pores. Thermally activated processes associated with the pore coarsening, only becomes effective above 2000°C. The experimental activation value of 76 ± 4 kcal/mole was determined from the Arrhenius plot of the changes in the radius of gyration, $\bar{R}_g$ as a function of heat-treatment temperature, and based on the fact that the rate of coarsening is dependent on the cube root of the heat-treatment time (rate $t^{1/3}$).

To confirm and correlate the structural evolution of the disordered structure, wide angle diffraction data was used to provide information about such parameters as interlayer and lattice spacings, $\bar{d}$ defect free distances (both perpendicular (L_c) and parallel (L_a) to the layer planes), and strain broadening, . Results of this study show that (i) prolonged heat-treatments at high temperatures is insufficient to graphitize the glass-like carbons, that is, the d_{002} reduction was only from 0.344nm to 0.340nm compared to 0.335nm for graphite; (ii) heating below about 2000°C causes a narrowing of the diffraction profiles, but the interlayer spacing $\bar{d}_{002}$ remains constant at 0.344nm even after 156 hours. This same behaviour of no change with time, but changes with temperature is found for the pore sizes.

Wide Angle Neutron diffraction (WAND) data showed that more than 80 percent of the broadening was due to strain. The neutron cross-section studies were used to obtain the relative number of hydrogen atoms to carbon atoms. This data correlated well with the results of the background extrapolation from the WAND data and the hydrogen analysis done by Mehrotra and Bragg [134], which showed that the hydrogen content decreases with increasing HTT.

CONCLUSIONS drawn from the above analyses are the following:

1. At temperatures below about 2000°C, there is no apparent time dependent structural change, that is, the changes are non-kinetic, and are most likely associated with the gas pressure mechanism.
2. At temperatures at and above 2000°C, the activation energy for pore coarsening is 76 ± 4 kcal/mole. This agrees well with the theoretical vacancy migration energy of (71 kcal/mole) value.
3. This activation energy is associated with vacancy migration parallel to the layer planes. The overall mechanism being that larger pores grow at the expense of smaller pores, and the structural changes are associated with the release of strain.
4. The high background obtained from the neutron data is a consequence of the hydrogen present (though in small amounts) in the carbon material.
5. There are three regions of structural change and this can be obtained from measurements made after heat-treatment in the temperature range 1000 - 2600°C.

(i) The first region represents a dramatic increase with temperature in the geometric structural parameters. Here, 90 percent of the hydrogen remaining after pyrolysis is removed.

(ii) The second region, represented by the plateau, indicates that the structural rearrangement process is slowing down as the last vestiges of the gases are being removed. The gas pressure mechanism becomes negligible in this region. Here the temperature range is about 1500 to 2000°C, and the interlayer parameters, L_c and $\overline{d}_{002}$, the pore parameter, $\overline{R}_{go}/\overline{R}_{gi}$, and the dimensional parameter, $1_o/1_1$ do <u>not</u> change.

(iii) In the third region, between 2000 and 2600°C, the slopes (of the geometric parameter changes) versus heat-treatment temperature become positive again, and the turbostratic carbon material become less disordered. Here the layers rearrange, the vacancies anneal, strain is relieved with enough energy to drive the process further. The graphitic structure is never achieved however, neither is all the strain relieved.

GLOSSARY

SYMBOLS	DEFINITION
Å	ANGSTROMS
ANL	ARGONNE NATIONAL LABORATORIES (IN TENNESSEE)
CKAPPA	IS THE CONSTANT IN THE EQUATION FOR CALCULATING THE COMPTON BACKGROUND SCATTERING
GLC	GLASS-LIKE CARBON
HOPG	HIGHLY ORIENTED PYROLYTIC GRAPHITE
HTT	HEAT-TREATMENT TEMPERATURE
HTt	HEAT-TREATMENT TIME
LSEM	LIFTSHITZ, SLYSOV MODIFIED ENCOUNTER THEORY
LSW	LIFTSHITZ, SLYSON AND WAGNER THEORY
MLSW	MODIFIED LIFTSHITZ, SLYSOV AND WAGNER
NBS	NATIONAL BUREAU OF STANDARD (IN WASHINGTON, D.C.)
NCS	NEUTRON CROSS SECTION
NGC	NON-GRAPHITIZABLE CARBON
NIS	NEUTRON INELASTIC SCATTERING
nm	NANOMETERS
PG	PYROLYTIC GRAPHITE
ppts	PRECIPITATES
PYC	PYROLYTIC CARBON
R_g	RADIUS OF GYRATION
S/V	SURFACE PER VOLUME
SAS	SMALL ANGLE SCATTERING
SAXS	SMALL ANGLE X-RAY SCATTERING

WAND	WIDE ANGLE NEUTRON DIFFRACTION
WAXD	WIDE ANGLE X-RAY SCATTERING
WRND	WIDE RANGE NEUTRON DIFFRACTION
WRXD	WIDE RANGE X-RAY DIFFRACTION

ACKNOWLEDGEMENTS

The author would like to acknowledge the support of Professor R. H. Bragg who directed this research. Special thanks also to him for providing the majority of my financial support during the length of my stay at the University. Deep appreciation is extended to Professors Ron Gronsky and Hans-Rudolph Wenk for helpful and meaningful discussions as well as serving with Professor R. H. Bragg on my thesis committee. Special thanks to Professors Gronsky and Alan Searcy for having a deep concern about all aspects of my course study and stay at the University.

It is with pleasure that I acknowledge the assistance provided by the technical staff of the Materials and Molecular Research Division of the Lawrence Berkeley Laboratory, with special thanks to Gloria Pelatowsky who drafted the line drawings. In particular, I would like to recognize the help and extreme patience provided by Jean Wolslegel and staff of the Technical Information Department. I wish now to extend thanks to my colleagues who helped make my stay at Berkeley a memorable one. In particular I would like to mention the graduates in our research group: Bhola N. Mehrotra, Tony Pearson, Jeff Hoyt and Dennis F. Baker. My gratitude to Professor Marshal F. Merriam for his guidance during Professor Bragg's leave of absence, and to Professor Segun Adewoye, who came on two visits from the University of Ife, Nigeria.

Special thanks to Felix Norris, John Walsh, John Frease, Jerry Myers and Allan Lyle, (all members of the MSME Workshop) not only for their technical assistance, but also for providing friendship during my stay in the department. Special thanks also to the department's secretaries, Judy Roberts, Madelein Penton and Mary Hammond, for their patience, understanding and help.

I wish also to acknowledge the partial financial support from the Kaiser Foundation.

Finally, I will forever remain grateful to my spouse, Bernadette, and my daughters Malene and Nilaja, for their understanding and patience during numerous hours I spent away from home.

This work was supported by the Director, Office of Energy Research, Office of Basic Sciences, Materials Sciences Division of the U. S. Department of Energy under Contract Number DE-AC03-76SF00098.

APPENDIX A

THE C_1 CONSTANT IN THE X-RAY PROFILE EQUATION

The equation for the observed x-ray intensity diffracted at any angle has been written in Section 2.1.1.1.

The constant C_1 in the equation can be written as:

$$C_1 = I_o * e^4/(m^2C^4R^2) * A_o/2\mu_c * N_A/At.Wt. \quad (31)$$

where

I_o is the incident unpolarized beam intensity.

A_o is the cross-sectional area of the incident beam.

Mu is the linear absorption coefficient of the sample.

N_A is the Avagadro number (= 6.023×10^{23} $mole^{-1}$).

At.Wt. is the atomic weight of the carbon material.

R is the sample -to-detector or sample to X-ray tube distance (= 14.55 cm).

e is the electronic charge (= 4.802×10^{-10} esu).

m is the electronic mass (= 9.109×10^{-28} gms).

c is the velocity of light (= 2.997×10^{10} cm sec^{-1}).

APPENDIX B

THE C_2 CONSTANT IN THE NEUTRON PROFILE EQUATION

The equation for the observed neutron diffracted intensity at any angle has been written in Section 2.1.1.2.

The constant C_2 in the equation can be written as:

$$C_2 = (\phi\lambda^3 * h_s * t * \rho^1)/(8\pi * R * \rho) \qquad (32)$$

where:

ϕ = neutron flux or the number of neutrons per min. in the incident monochromatic beam (neutrons $m^{-2}s^{-1}$).

λ is the wavelength of the incident beam.

h_s is the height of the counter slit.

R = distance from specimen to counter.

t = thickness of specimen.

ρ^1 = measured density of specimen.

ρ = theoretical density.

APPENDIX C

TABULATED VALUES USED IN "PEEL-OFF" ANALYSIS

The Warren function [54], F(A) is given by:

$$F(A) = \int_0^\infty \exp[-(x^2-A)^2]dx \qquad (33)$$

where $A = [(\pi)^{1/2} * L_a * (r - \lambda H)]/\lambda$

$\lambda H = 2\sin\theta_o$

$r = 2\sin\theta$

$x = [(\pi)^{1/2} * L_a * r/2\ \lambda]^{1/2}$

λ is the wavelength

A	F(A)	A	F(A)
-1.2	0.12	0.1	0.96
-1.0	0.21	+0.2	1.01
-0.8	0.32	+0.3	1.04
-0.6	0.46	+0.4	1.06
-0.5	0.53	+0.5	1.07
-0.4	0.61	+0.6	1.06
-0.3	0.69	+0.8	1.04
-0.2	0.77	+1.0	0.99
-0.1	0.84	+2.0	0.67
0.0	0.91	+3.0	0.52

Appendix C (cont.)

In the analysis done here, L_a, lambda, λ, θ and θ_o are obtained from the diffraction data. The 2 theta position of zero intensity can now be obtained from the plot of F(A) versus A.

APPENDIX D1

THE INCOHERENT (BACKGROUND) SCATTERING ANALYSIS

The total scattering at large $k(= 4\pi\sin\theta/\lambda)$ from any atom with z electrons can be written as the sum of the coherent and incoherent (background) scattering [59], that is

$$I_{TOT}(2\theta) = I_{COH}(2\theta) + I_{INC}(2\theta). \tag{34}$$

For GLC, the low atomic number carbon material, with thickness t_s, bulk density ρ_s, coherent and incoherent linear absorption coefficients, μ_c and μ_i, respectively, the background scattering can be written as [71]:

$$I_{TOT}(2\theta) = I_{inc}(2\theta) = K_s \left(\frac{\rho_s}{\mu_c+\mu_i}\right) \times Pol(2\theta) \times \mathcal{I}_{inc}(2\theta)\left[1-\exp\left\langle-\frac{(\mu_c+\mu_c)t_s}{\sin\theta}\right\rangle\right]$$

$$\times \exp\left\langle-(\mu_A t_A + \mu_w t_w)B^3\right\rangle \tag{35}$$

where $K_s = C_1 \quad 2\mu_c$ is sample dependent.

C_1 is defined in Appendix A

and Pol $(150^\circ 2\theta) = 0.8750$

$\mathcal{I}_{inc}(2\theta) = \left(\frac{\mathcal{I}_{eu}}{R_B}\right) \times R_B$ is the incoherent scattering for for elemental carbon, and

$\left(\frac{\mathcal{I}_{eu}}{R_B}\right)$ is the incoherent scattering for elemental carbon in electron units [91].

B is the Breit-Dirac recoil factor [159,160]

$\mu_c + \mu_i = \mu_c [1 + B^3]$

Appendix D1 (cont.)

$$\text{where } B^3 = \frac{1}{R_B}$$

$\mu_w t_w = 0.0473$ for the Beryllium window in the detector.

$\mu_a t_a = 0.2137$ for the air in the sample chamber.

The above equation (35) is based on the assumption that at large angles the background scattering is essentially all incoherent scattering except near an interference maximum [70]. The equation shows that from a measurement of the incoherent intensity $I_{inc}(2\theta)$ at large $\sin\theta/\lambda$, and a knowledge of the other parameters, the constant K_s for each sample can be obtained, and hence $I_{inc}(2\theta)$ over the whole range can be generated.

APPENDIX D2
X-RAY DATA USED IN THE ANALYSIS

SAMPLE T°C	Thickness, t (cms)	Time (hrs)	Length (cms)	Density (gm/cm^2)	$\mu*t$	μ_c (cm^{-1})	$2\mu_c*R^{\dagger}$
1200	0.172	9 to 156	5.068	1.510	1.055	6.132	178
1400	0.172	9 to 72	5.110	1.502	1.083	6.295	183
1600	0.174	9 to 48	5.140	1.485	1.064	6.115	178
1800	0.168	9 to 100	5.156	1.471	1.044	6.123	178
2000	0.285	6	5.146	1.456	1.718	6.023	176
2000	0.283	72	5.158	1.434	1.657	5.955	173
2200	0.283	0	5.090	1.434	1.657	5.955	173
2300	0.240	48	5.216	1.402	1.237	5.511	160
2400	0.170	0	5.208	1.426	0.951	5.457	159
2400	0.168	30	5.234	1.400	0.947	5.565	162
2500	0.120	4	5.276		0.678	5.590	163
2500	0.120	30	5.274		0.662	5.539	161
2600	0.286	0	5.052	1.387	1.661	5.808	169
2600	0.180	4	5.056	1.378	0.891	5.607	164

$^{\dagger}R = 14.55$ cm

APPENDIX D3
X-RAY DATA USED IN THE ANALYSIS

SAMPLE T°C	Thickness, t (cms)	Time (hrs)	$(\mu_c+\mu_I)$	$(\mu_c+\mu_I)t$	(1-exp) inc	CKAPPA*	SAXS SLOPE
1200	0.172	9 to 156	12.72	2.197	0.897	14.25	-2.8
1400	0.172	9 to 72	13.11	2.255	0.903	14.00	-2.9
1600	0.174	9 to 48	12.74	2.216	0.899	15.56	-3.1
1800	0.168	9 to 100	12.75	2.143	0.895	19.91	-3.1
2000	0.285	6	12.63	3.587	0.975	14.97	-3.2
2000	0.283	72	12.52	3.544	0.9745	14.39	-3.0
2200	0.283	0	12.40	3.515	0.974	15.08	-3.3
2200	0.162	60	12.84	2.079	0.884	48.37	-3.5
2300	0.224	48	11.48	2.576	0.931	15.16	-3.0
2400	0.170	0	11.37	1.932	0.865	14.52	-3.1
2400	0.168	30	11.59	1.947	0.870	15.07	-3.2
2500	0.120	4	11.64	1.390	0.763	15.11	-3.3
2500	0.120	30	11.42	1.370	0.762	15.85	-3.2
2600	0.286	0	12.10	3.460	0.967	14.66	-3.4
2600	0.1880	4	11.68	1.864	0.843	10.43	-3.6

*CKAPPA defined in glossary p. .

REFERENCES

1. G. M. Jenkins, and K. Kawamura, "Polymeric Carbons-carbon Fibres, Glass and Char," Cambridge University Press, Cambridge (1976).

2. G. M. Jenkins, K. Kawamura, and L. L. Bann, "Formation and Structure of Polymeric Carbons, "Proc. Roy. Soc. (London) A 327, 501 (1972).

3. E. Fitzer, W. Schaefer and S. Yamada, "The Formation of Glasslike Carbon by Pyrolysis of Polyfurfuryl Alcohol and Phenolic Resin" Carbon 7,643 (1969).

4. T. Nodar, M. Inagaki, and S. Yamada, J. Non-Crystalline Solids, 1, 285 (1969).

5. E. E. Hucke, "Glassy Carbons" Semi-Annual and Final Reports; The University of Michigan, Ann. Arbor Mich., ARPA Order No. 1824 Contract No. DAHC 15-71-C-0283, (1971-1975).

6. I. S. Nadeau, "Hertzian Fracture of Vitreous Carbon", J. Amer. Cer. Soc. 56; 467 (1973).

7. W. P. Minnear, T. M. Hollenbeck, R. C. Bradt, and P. L. Walker, Jr., "Subcritical Crack Growth of Glass Carbon in Water," Non-cryst. Solids. 21, 107-115 (1976).

8. J. S. Nadeau, "Subcritical Crack Growth in Vitereous Carbon at Room Temperature", J. Amer. Cer. Soc., 57, 303-306 (1974).

9. H. M. Hawthorne, "The Microindentation Hardness Behaviour of Carbon Filaments, Glassy Carbons and Pyrolytic Graphites", Carbon 13, 215 (1975).

10. G. M. Jenkins, "Deformation Mechanisms in Carbons", Chem. and Physics of Carbon, P. L. Walker, Jr., and P. A. Thrower, editors Marcel Dekker, N. Y., Vol. 11, p. 169 (1975).

11. W. V. Kottlensky, and H. E. Martens, Tensile Properties of Glassy Carbon to 2900°C", Nature, 206, 1246 (1965).

12. J. J. Melcholsky, R. W. Rice, and S. W. Freeman," Prediction of Fracture Energy and Flaw Size in Glasses from Measurements of Mirror Size," J. Amer. Cer. Soc. 57, 440 (1974).

13. S. Yamada, and H. Sato, "Some Physical Properties of Glassy Carbon" Nature (London) 193, 261 (1962).

14. F. C. Cowlard, and J. C. Lewis, "Vitreous Carbon-A New Form of Carbon," Jour. Mat. Sci. 2, 507-512 (1967).

15. E. Fitzer, W. Schaefer, and S. Yamada, "The Formation of Glass-Like Carbon by Pyrolysis of Polyfurfuryl Alcohol and Phenolic Resin," Carbon 7, 643-648 (1969).

16. F. Rodriguez-Reinso, and P. L. Walker, Jr., "Reaction of Glassy Carbon with Oxygen," Carbon 13, 7-10 (1975).

17. T. C. Peng, "Oxidation Effects on the Tensile Strength of ATPS Graphite and Vitreous Carbon," Carbon 17, 157-174 (1979).

18. G. L. Tingey, "Chemical Activity of Glass-Like Carbons," Extended Abstracts 12th Biennial Carbon Conference, Pittsburgh, Pennsylvania, July 28 - August 1, (1975) p. 181.

19. A. Kellomaki, "Electrolytic Durability of Glass Carbon," Jour. Mat. Sci., 15, 1316 (1980).

20. Tylan Corporation, 19220 S. Normandie Ave., Torrance, California, 90502.

21. S. Hosoki, S. Yamamoto, M. Futomoto, and S. Fukuhara," Field Emission Characteristics of Carbon Tips," Surface Science, 86, 723 (1979).

22. R. W. Hendricks et al. "Final report of the International Project for the calibration of Absolute Intensities in Small-angle X-ray Scattering," Commission on Crystallographic Apparatus, Int'l Union of Crystallography, J. Appl. Cryst., 11, 196 (1978).

23. R. Perret, and W. Ruland, "Glassy Carbon as Standard for the Normalization of Small-Angle Scattering Intensities," J. Appl., Cryst., 5 116 (1972).

24. D. F. Baker, "An Overview of Carbons and Glassy Carbons" LBL Report No. LBID - 680 March 1983, Materials and Molecular Research Division, Lawrence Berkeley Lab. University of California, Berkeley, CA 94720.

25. R H. Bragg, and M. L. Hammond, "X-Ray Study of Graphites and Glassy Carbon," 7th Biennial Carbon Conference, Cleveland, Ohio, June 21 - 25, 1965 paper No. 57 also Carbon 3, 340 (1965).

26. G. Porod, and G. Kolloid-Z 124, 83 (1951).

27. P. Debye, N. R. Anderson, and H. Brumberger, J. Appl Physics, 28, No. 6, 689 (1957).

28.(a) R. A. Van Nostrand, and K. M. Hach, Paper presented at the Amer. Chem. Soc. meeting, Chicago, Sept. 1953.

28.(b) R. A. Van Nostrand, and K. M. Hach, and M. F. L. Johnson Paper presented at the Amer. Chem. Soc. meeting in N. Y. September 1954.

29. R. Perret and W. Ruland, "X-Ray Small Angle Scattering of Non-graphitizable Carbons", J. Appl. Cryst. 1, 308 (1968).

30. R. Perret and W. Ruland, "X-Ray Small Angle Scattering of "Glassy Carbon" 10th Biennial Carbon Conference, Lehigh University, Bethlehem, Penn. (1971), paper No. SS91, p. 146.

31. R. Perret and W. Ruland, "X-Ray Small Angle Scattering of Glassy Carbon", J. Appl. Cryst. 5, 183 (1972).

32. R. G. Jenkins and P. L. Walker, Jr., "Small Angle X-Ray Scattering Studies on Carbons Derived from Polyfurfuryl Alcohol (PFA) and Polyfurfuryl Alcohol (PFA) Ferrocene Copolymers," Carbon 14, 7 (1976).

33. L. G. Henry and R. H. Bragg, "Simple Conversion of Commercial Diffractometer for Small Angle X-Ray Scattering (SAXS) Measurements", LBL Report No. 15773, December 1983, Lawrence Berkeley Laboratory, University of California, Berkeley, CA.

34. S. Bose, U. Dahmen, R. H. Bragg and G. Thomas, "Lattice Image of LMSC Glassy Carbon", J. Amer. Cer. Soc. 61, 174 (1978).

35. J. L. Kaae, "Microstructural Observations on a Commercial Glassy Carbon", Carbon 13, 246 (1975).

36. V. A. Phillips, "Lattice Structure in 1800°C Processed Vitreous Carbon", Metallography 6, 361 (1973).

37. L. L. Ban, D. Crawford, and H. Marsh, "Lattice Resolution Electron Microscopy in Structural Studies of Non-graphitizing Carbons from Polyvinylidene Chloride (PVDC)", J. Appl. Cryst. 8, 415 (1975).

38. R. Gronsky and R. H. Bragg, "Lattice Images in Glassy Carbon", 33rd Pacific Coast Regional Meeting, Amer. Cer. Soc. San Francisco, CA, October, (1980).

39. S. Bose and R. H. Bragg, "Procedure for Correcting the X-Ray Line Profile of Glassy Carbons", University of California, Lawrence Berkeley Laboratory Report No. 6649 (1978a).

40. L. G. Henry and R. H. Bragg, "Anomalous Large Layer Spacings in Glassy Carbon", 14th Biennial Conference on Carbon, Pennsylvania State University University Park, PA, June 25 - 29, 1979; also LBL Report No. 13544, U. C. Berkeley, CA, December 1978.

41. L. G. Henry, R. H. Bragg and S. Bose, "Procedures for Analyzing the X-Ray Line Profiles of Disordered Carbons", 34th Pacific Coast Regional Meeting of the Amer. Cer. Soc., Newport Beach, CA., October 25 - 28, 1981; and LBL Report No. 13698, U. C. Berkeley, CA, December 1981.

42. L. G. Henry, R. H. Bragg, J. Rush and J. Rhyne, "Comparative Profile Analysis of Glass-Like Carbons Using X-Ray and Neutron Diffraction", 16th Biennial Carbon Conference, San Diego, CA., July 18-22, 1983; also LBL Report No. 15882, U. C. Berkeley, CA, March 1983.

43. S. Ergun, Carbon 14, 139 (1976); Phys. Rev. 1, No. 8, 337 (1970); with R. R. Schehl, Carbon 11, 27 (1973).

44. W. Ruland, Acta Cryst. 14, 1186 (1961).

45. R. Perret and W. Ruland, J. Appl. Cryst. 1, 257, (1968).

46. M. A. Short and P. L. Walker, Jr., "Measurement of Interlayer Spacings and Crystal Sizes in Turbostratic Carbons", Carbon 1, 3 (1963).

47. R. R. Saxena and R. H. Bragg, "Kinetics of Graphitization in Glassy Carbon Carbon 16, 373 (1978), and Ph. D. Thesis (Saxena's) UCLBL Report No. LBL-5129, (1976).

48. S. Bose, "Pore Structure and Growth Kinetics in Carbon Materials". Ph.D. thesis, University of California, Berkeley April 1978, LBL-7638.

49. R. H. Bragg, M. L. Hammond, J. C. Robinson and P. L. Anderson, "Nature (London) 200 No. 4906, p. 555 (1963).

50. S. Bose and R. H. Bragg, "Kinetics of Pore Coarsening in Glassy Carbon" Carbon 19, No. 4, p. 289, (1981).

51. J. J. Hoyt and R. H. Bragg, "Pore Shape and Growth Kinetics in Glassy Carbon Using SAXS", 34th and 35th Pacific Coast Regional Meeting, Amer. Ceram. Soc. Newport Beach, CA., October 25-28, 1981, and October 26-28, 1982; also M. S. Thesis (J. J. Hoyt) July 1982 LBL-14580, and LBL Report No. 13784, U. C. Berkeley CA, October 1981.

52. J. Biscoe and B. E. Warren, "An X-Ray Study of Carbon Black", J. Appl. Phys., 13, 364 (1942).

53. C. R. Houska and B. E. Warren, "X-Ray Study of the Graphitization of Carbon Black", J. Appl. Phys. 25, No. 12, p. 1503 (1954).

54. B. E. Warren, "X-Ray Diffraction in Random Layer Lattices", The Physical Review, 59, No. 9, 693 (1941).

55. B. E. Warren, "X-Ray Diffraction Study of Carbon Black", Jour. of Chem. Physics 2, No. 9, 551 (1934).

56. Rosalind E. Franklin, "The Interpretation of Diffuse X-Ray Diagrams of Carbon", Acta. Cryst. 3, 107 (1950).

57. B. D. Cullity, "Elements of X-Ray Diffraction", 2nd Edition, Addison Wesley Publ. Co., (1978).

58. H. P. Klug and L. E. Alexander, "X-Ray Diffraction Procedures for Polycrystalline and Amorphous Materials", John Wiley, N. Y., 2nd Edition (1974).

59. M. A. Short, Acta. Cryst. 14, 486 (1961).

60. B. E. Warren and R. L. Mozzi, J. Appl. Cryst. 3, 59 (1970).

61. S. Ergun in Chem. and Physics of Carbon, Vol. 3 (P. L. Walker Jr., editor) Marcel Dekker Publ. Co., N. Y. p. 225 (1968).

62. T. Willis (editor) "Thermal Neutron Diffraction", Oxford University Press (1970) Chapters 1-4.

63. G. E. Bacon, "Neutron Diffraction", Clarendon Press, Oxford, 1975, 3rd edition.

64. L. H. Schwartz and J. B. Cohen, "Diffraction from Materials", Academic Press, San Francisco, CA. (1977).

65. W. S. Rosenthal, J. Appl. Phys., 39 No. 3, 1840 (1968).

66. M. M. Biswall, P. O. Bihuniak and R. H. Bragg, Abstracts, 10th Biennial Carbon Conference, June 27 - July 2, Lehigh University, Bethlehem, Pa. p. 145 (1971).

67. R. G. Jenkins and P. L. Walker Jr., Abstracts, 11th Biennial Carbon Conference, June 4 - 8, Gatlinberg, Tenn. p. 182 (1973).

68. S. Bose and R. H. Bragg, The 2nd Int'l Conf. on Carbon (Carbon '76) Deutsche Keramische Gesselschaft (German Ceramic Soc.), Baden - Baden. Fed. Republic of Germany, p. 205 (1976).

69. D. T. Keating and B. E. Warren, Rev. Sci. Instr., 23, 519 (1952).

70. R. H. Bragg and C. M. Packer, Rev. Sci. Instr., 34, 1202 (1963).

71. L. G. Henry and R. H. Bragg, "Comparative Determination of the Incoherent Scattering in Amorphous Materials", LBL Report No. 15611, U. C. Berkeley, CA, December 1982.

72. B. E. Bacon, "Neutron Physics", (1969), Wykeman Publ. Ltd. (London).

73. P. Scherrer, (1918) 2, 98 Nach., Gres. Wissench. Gottingen, 2, 98, cited by M. A. Short and P. L. Walker Jr., Carbon 1, 3 (1963)

74. J. T. Randall, H. P. Rossky and B. S. Cooper, Z Kristallog 75, 196 (1930).

75. A. Guinier, G. Fournet, C. B. Walker, and K. Yudowitch, "Small Angle Scattering of X-Rays", John Wiley and Sons, N. Y. (1955).

76. P. Krisnamurti, "Studies in X-Ray Diffraction - Part 1, The Structure of Amorphous Carbon", Aus. J. Phys. 5, 473 (1930).

77. Lord Rayleigh, Proc. Royal Soc. (London) A-84, 25 (1911) and A-90 (1914).

78. G. Porod, "Determination of General Parameters by SAXS". Chapter 1 of SAXS, editor H. Brumberger, Gordon and Breach, N. Y. (1967). Proc. of the Conf. on SAXS held at Syracruse University, June 1965.

79. G. Porod, "General Theory" Chapter 2 of SAXS, editors O. Glatter and O. Kratky, Academic Press, San Francisco, CA. (1982).

80. R. Perret and W. Ruland, J. Appl. Cryst. 2, 209 (1969).

81. R. Perret and W. Ruland, J. Appl. Cryst. 3, 525 (1970).

82. C. Schiller and J. Méring, C. R. Acad. Sci. Paris, t 264, Serie B, 247 (1967).

83. W. Ruland, "Small Angle Scattering of Two Phase Systems: Determination and Significance of Systematic Deviations from Porod's Law", J. Appl. Crys. 4, p. 70 (1971).

84. V. Luzzati, J. Wetz and A. Nicolaieff, J. Mol. Biology 3, 367 (1961).

85. J. H. Wendorff and W. Ruland, Kolloid Z u Zeit Polymere, 251, 876 (1973) "Thermal Density Fluctuations in Amorphous Polymers as Revealed by X-Ray Diffraction".

86. R. Perret and W. Ruland, Kolloids Z u Zeit Polymere, 247, 835 (1971).

87. C. G. Vonk, "Investigation of Non - Ideal Two-Phase Plymer STructures by SAXS", J. Appl. Cryst. 6, 81 (1973).

88. J. Rathje and W. Ruland, Colloid and Polymer Sci. 254, 358 (1976). "Density Fluctuations in Amorphous and Semicrystalline Polymers".

89. W. Weigan and W. Ruland, "Density Fluctuations as a State of Order of Amorphous Polymers", Colloid and Polymer Science 66, 355 (1979).

90. W. Ruland, Colloid and Polymer Science, 255, 417 (1977).

91. International Tables for X-ray Crystallography, Vol. III, p. 247, Kynock Press, Birmingham (1968).

92. M. M. Biswall and R. H. Bragg, "Void Growth in Glassy Carbon", 12th Biennial Carbon Conf., Pittsburg, Penn. July 1975, p. 51.

93. I. M. Lifshitz and V. V. Slyzov, "The Kinetics of Precipitation from Supersaturated Solutions", J. Phys. Chem. Solids 19, No. 1/2, 35 (1961).

94. C. Wagner, Z. Electrochem. 65, 581 (1961).

95. A. J. Ardell and R. B. Nicholson, Acta. Metallurgica 14, 1295 (1966).

96. A. J. Ardell and R. B. Nicholson, "The Coarsening of γ' in Ni-Al Alloys", J. Phys. Chem. Solids 27, 1793 (1966).

97. K. V. Vedula and R. W. Heckel, "Spheroidization of Binary Fe-C Alloys Over a Range of Temperatures", Metall. Trans. 1, 9 (1970).

98. A. J. Ardell, "The Growth of Gamma Prime Precipitates in Aged Ni-Ti Alloys", Metall. Trans. 1, 525 (1970).

99. A. J. Ardell, "The Effect of Volume Fraction in Particle Coarsening: Theoretical Considerations", Acta. Metall. 20, 61 (1972).

100. D. J. Chellman and A. J. Ardell, "The Coarsening of γ' Precipitates at Large Volume Fractions", Acta. Metall. 22, 577 (1974).

101. A. D. Brailsford and P. Wynblatt, "The Dependence of Ostwald Ripening Kinetics in Particle Volume Fraction", Acta. Metall. 27, 489 (1979).

102. K. Tsumuraya and Y. Miyata, "Coarsening Models Incorporating Both Diffusion Geometry and Volume Fraction of Particles", Acta. Metall. 31, No. 3,437 (1983).

103. C. K. L. Davies, P. Nash and R. N. Stevens, "The Effect of Volume Fraction of Precipitate on Ostwald Ripening", Acta. Metall. 28, 179 (1980).

104. G. J. Diennes, "Mechanism for Self-Diffusion in Graphite", J. Applied Physics, 23, No. 11, 1194 (1952).

105. L. Pauling, "The Nature of the Chemical Bond and the Structure of Molecules and Crystals; An Introduction to Modern Structural Chemistry", Cornell University Press, p. 53 (1944).

106. M. A. Kanter, "Diffusion of Carbon Atoms in Natural Graphite Crystals" Physical Review, 107, No. 3, 655 (1957).

107. C. A. Coulson, "Valence", Clarendon Press, 1953.

108. C. A. Coulson, M. A. Herraez, M. Leal, E. Santos and S. Senent, "Formation Energy of Vacancies in Graphite Crystals", Proc. Roy. Soc. (London) A274, 461, (London), 1963.

109. H. T. Knight and J. P. Rink, "Heat of Sublimation of Carbon and the Dissociation Energy of CO by X-ray Densitometry of Shock Waves", J. Chem. Phys. 29, 149 (1958).

110. C. A. Coulson and M. D. Poole, "Calculations of the Formation Energy of Vacancies in Graphite Crystals, Carbon 2, 275 (1964).

111. A. Kelly cited by P. A. Thrower, Phil. Mag. 18, 697 (1968).

112. P. A. Thrower, "The Influence of Crystal Perfection on Defect Nucleation in Graphite Irradiated at High Temperatures", Carbon 6, 687 (1968).

113. A. P. Nicholson and D. J. Bacon, "A Defect Molecule Calculation for the Vacancy in Graphite", Carbon 13, 275 (1975).

114. R. Smoluchowski, "Theory of Grain Boundary Diffusion", Phys. Review 87, 482 (1952).

115. C. Baker and A. Kelly, "Energy to Form and to Move Vacant Lattice Sites in Graphite", Nature (London), 193, No. 4812, p. 235 (1962).

116. G. R. Hennig, "Vacancies and Dislocation Loops in Graphite", Appl. Phys. Lett. 1, 55 (1962).

117. G. Hennig, "Vacancies and Dislocation Loops in Quenched Crystals of Graphite", J. Appl. Phys. 36, No. 4, 1482 (1965).

118. M. Herrschap and P. Delavignette, "Vacancy Loops in Irradiated and Annealed Graphite", J. of Nucl. Materials 12, No. 3, 349 (1964).

119. R. R. Henom and W. N. Reynolds, "Lattice Parameter Changes in Irradiated Graphite", Carbon 3, 277 (1965).

120. M. H. Feldman, W. V. Goeddel, G. J. Diennes and W. Gossen, "Studies of Self, Self-Diffusion Using C-14 Tracer", J. Appl. Phys. 23, No. 11, 1200. (1952).

121. G. Porod, Kolloid Z 124, 83 (1951).

122. F. M. Hamzeh and R. H. Bragg, "Small Angle Scattering from Groups of Randomly Oriented Ellipsoids of Revolution of Low Concentrations", J. Appl. Phys. 45, No. 7, 3180 (1974).

123. A. G. Malmon, "Small Angle X-Ray Scattering Functions for Ellipsoids of Revolution and Right Circular cylinders", Acta. Cryst. 10, 639 (1957).

124. L. C. Roess and C. G. Schull, "X-Ray Scattering at Small Angles by Finely Divided Solids", I and II, J. Appl. Phys. 18, 295 - 307 and p. 308-313 (1947).

125. S. Bose and R. H. Bragg, "Small Angle X-Ray Scattering from Oriented Ellipsoidal Voids in PG", J. Appl. Phys. 49, No. 4, 2916 (1978).

126. P. Schmidt, Ph. D. Thesis, University of Wisconsin (1948).

127a. G. Porod, Acta Physica Austriaca 2, 255 (1948).

127b. P. W. Schmidt, "The Small Angle X-Ray Scattering from Polydisperse Solutions of Ellipsoid Particles", Acta. Cryst. 11, 674 (1958).

128a. P. Mittelback and G. Porod, Acta. Physica Austriaca 15, 122 (1952).

128b. P. W. Schmidt and R. Hight Jr., "Calculation of the Intensity of SAXS at Relatively Large Scattering Angles, J. Appl. Phys. 30, No. 6,866 (1959).

129. O. L. Brill and P. W. Schmidt, "Small Angle X-Ray Scattering Determination of Diameter Distributions", J. Appl. Physics 39, No. 5, 2274 (1968).

130. H. Dachs, editor, Neutron Diffraction, Chapter 1, "Principles of Neutron Diffraction", Springer - Vellag, New York, (1978).

131. G. Kostorz and S. W. Lovesey, "Neutron Scattering - General Introduction" in Treatise on Materials Science and Technology - Vol. 15 of Neutron Scattering edited by G. Kostorz, Acad. Press, San Francisco (1979).

132. R. T. Meyer, A. W. Lynch, J. M. Freise, M. C. Smith and R. J. Imprescia, Carbon 11, 258 (1973).

133. B. N. Mehrotra, Ph. D. Thesis, University of California, Berkeley, (Thesis being written at time of submission December 1985).

134. B. N. Mehrotra, R. H. Bragg and A. S. Rao, "Effect of Heat-Treatment Temperature (HTT) on Density, Weight and Volume of Glass-Like Carbon", J. Mat. Sci. 18, 2671 (1983).

135. J. P. Edmond and P. L. Walker Jr., Nature 186, 72 (1960).

136. R. B. Anderson and P. H. Emmett, J. Phys. Chem. 56, 753 (1952).

137. L. G. Henry and R. H. Bragg, "Experimental Deterination of Compton Scattering from PG and GLC", Abstract, 15th Biennial Carbon Conference, June 22 - 26th , 1981, p. 478, University of Penn., Philadelphia, PA, also LBL Report No. 13546, U. C. Berkeley (1980).

138. S. Bose and R. H. Bragg, "Fourth International, Conference on Small Angle Scattering of X-Rays and Neutrons", Gatlinberg, Tennessee, p. 32 (1977).

139. S. Bose and R. H. Bragg, "Small Angle X-Ray Scattering by Diffuse Interfaces" LBL Report No. 6656, September 1977.

140. R. Causey, J. S. Ellman and V. Verghese, "Hydrogen Diffusion and Solubility in Pyrolytic Carbon", Carbon 17, 329 (1979).

141. K. Karamura and R. H. Bragg, "Strain Relief and Crystallite Growth in Heat-Treated Pyrocarbon", 37th Pacific Coast Regional Meeting of Amer. Cer. Soc., October 1984.

142. A. G. Whittaker and B. Tooper, "Single X-tal Diffraction Patterns from Vitreous Carbon", J. Amer. Ceram. Soc. 57, 443 (1974).

143. A. Fourdeaux, R. Perret and W. Ruland, Extended Abstracts of the 10th Biennial Carbon Conference, Lehigh University Bethlehem, June 27-July 2, paper FC-22, (1971).

144. A. Fourdeaux and R. Perret, C. R. Acad. Sci. Paris.

145. R. H. Heidenreich, W. M. Hess and L. L. Bann, "A Test Object and Criteria for High Resolution Electron Microscopy", J. appl. Cryst. 1 1-19 (1968).

146. F. M. Collins, "Dimensional Changes During Heat-Treatment and Thermal Expansion of Polycrystalline Carbons and Graphite". Proceedings of the 1st and 2nd Conf. on Carbon, Buffalo N. Y., November 1953 and June 1955 (Amer. Carbon Soc.), The University of Buffalo, Buffalo, N. Y., 1956, p. 177.

147. D. B. Fischbach and M. E. Rorabaugh, "Glassy Carbon Graphitization: Density Change", High Temperature - High Pressure, 1977, Vol. 9, p. 199.

148. J. Nadeau, J. Amer. Cer. Soc. 56 (9) 467 (1973).

149. J. Nadeau, J. Amer. Cer. Soc. 57(7) 303 (1974).

150. C. E. Holcombe, High Temp. Sci. 12, p. 63 (1980).

151. A. L. Sutton and V. C. Howard, "The Role of Porosity in the Accommodation of Thermal Expansion in Graphite", J. Nucl. Mater., 7(1), 1972 p. 58.

152. S. Mrozowski, "Mechanical Strength, Thermal Expansion and Structure of Cokes and Carbons", Proc. of the 1st and 2nd Sects. (see No. 146 for details).

153. T. Noda and H. Kato, "Heat Treatment of Carbon Under High Pressure", Carbon 3, 289 (1965).

154. L. G. Henry and R. H. Bragg, "Strain Relief and Crystallite Growth in Heat-Treated Glass-Like Carbons", 37th Pacific Coast regional Meeting of the American Ceramic Society, October 28-31, 1984, also LBL Report No. 18510, U. C. Berkeley, CA, October 1984.

155. K. Karamura, R. H. Braff and S. Kimura "Carbonization and Graphitization of Coal-Tar Pitch Mixed with Trinitrophenol". LBL Report No. 18783, U. C. Berkeley, CA, January 1985.

156. L. G. Henry and R. H. Bragg, "Kinetics of Void Growth in Heat-Treated Glass-Like Carbons", 37th Pacific Coast Regional Meeting of the American Ceramic Society, October 28-31, 1984, also LBL Report No. 18509, U. C. Berkeley, October 1984.

157. M. E. Tidjani, L. G. Henry and R. H. Bragg, "Characterization of Particle Size and Shape Using Small Angle x-Ray Scattering", 37th Pacific Coast Regional Meeting of the American Ceramic Society, October 28-31, 1984; also LBL Report No. , U. C. Berkeley, 1984.

158. P. A. Ross and P. Kirkpatrick, "The Constant in the Compton Equation", Phys. Rev. 45, No. 3, 223 (1934).

159. G. Breit, "A Correspondence Principle in the Compton Effect", Phys. Rev. 27, 362 (1926).

160. P. A. M. Dirac, "Relativity Quantum Mechanics with an Application to Compton Scattering", Proc. Roy. Soc. A-111, 405 (1926).

161. T. M. Sabine and P. J. Clarke, "Powder Neutron Diffraction - Refinement of the Total Pattern", J. Appl. Cryst. 10, 277 (1969).

162. T. M. Sabine, "Neutron Diffraction - The Total Powder Pattern", Aust. J. Phys. 33, 565 (1980).

163. G. Caglioti, A. Paoletti and F. P. Ricci, "Choice of Collimation for a Crystal Spectrometer for Neutron Diffraction", Nucl. Inst. Methods 3, 223 (1958).

164. D. Tchoubar and J. Mêring. "Interpretation de la Diffusion Central des Rayons X par les Systemes Poreux.I, II Examples de Application", J. Appl. Cryst. 2, 128 (1969).

165. "User Notes for the 10 Meter SAX Instrument", National Center for Small-Angle Scattering Research. Solid State Division, Oak Ridge National Laboratory, Oak Ridge, Tennessee, July 1983.

TABLE 4.1.A

X-RAY INTERLAYER SPACINGS d_{002} FOR GLC

HTT/HTT	t(cm)	20°	d_{002}	20°	d_{002}(Å)	SAXS SLOPE
1200	0.172	24.3°	3.66A	25.5°	3.49±0.03	-2.7
1400	0.172	24.9	3.58A	25.7	3.47	-2.9
1600	0.174	24.9	3.58A	25.7	3.47	-3.1
1800	0.168	25.3	3.52	25.6	3.48	-3.1
*2000-6	0.284	24.9	3.58	25.5	3.49	-3.2
*2000-72	0.284	25.2	3.53	25.7	3.47	-3.0
*2200-0	0.283	25.0	3.56	25.7	3.47	-3.3
2200-60	0.162	25.5	3.49	26.0	3.43	-3.5
*2300-48	0.224	25.5	3.49	26.0	3.43	-3.0
2400-0	0.170	25.5	3.49	25.9	3.44	-3.1
2400-30	0.168	25.4	3.51	26.0	3.43	-3.2
2500-4	0.120	25.5	3.49	26.0	3.43	-3.3
2500-30	0.120	25.7	3.47	26.10	3.41	-3.2
2600-4	0.160	25.7	3.47	26.00	3.42	-3.6

*Very thick samples

TABLE 4.1.B
BASAL PLANE STACKING SIZE L_{002} FOR GLC
X-RAY DATA

	RAW DATA		CORRECTED DATA		Percentage difference in	t(cm)
HTT	$B_{1/2}\cos\theta$	L_c(Å)	$B_{1/2}\cos\theta$	L_c(Å)	L_c's	
1200	NSR	--	0.1224	11.2±0.24Å	--	0.172
1400	0.1133	12.1Å	0.0893	15.4 "	21Å	0.172
1600	0.1099	12.5	0.8597	16.0 "	22	0.172
1800	0.1054	13.0	0.834	16.5 "	21	0.168
*2000-6	0.1116	12.2	0.894	15.4 "	20	0.284
*2000-72	0.1039	13.2	0.0825	16.6	21	0.283
*2200-0	0.1063	12.9	0.0881	15.6	17	0.283
2200-60	0.0717	19.2	0.0604	22.7	16	0.162
*2300-48	0.0707	19.4	0.0612	22.4	13	0.224
2400-0	0.741	18.5	0.6377	21.5	14	0.170
2400-30	0.0655	20.9	0.0585	23.6	11	0.168
2500-4	0.0655	20.9	0.0585	23.3	10	0.120
2500-30	0.0638	21.5	0.0568	24.2	11	0.120
2600-4	0.0609	22.5	0.0558	24.6	8	0.160

NSR = Not sufficiently resolved

$L_c = 0.89*\lambda/(B_{1/2}\cos\theta)$

* = Thick samples

TABLE 4.2.A
RAY AND CORRECTED NEUTRON DATA: d-spacings

	GLC1200°C				GLC1800°C			
	RAW		PEEL		RAW		PEEL	
hkl	2θ°	d(Å)	2θ°C	d(Å)	2θ°C	d(Å)	2θ°	d(Å)
002	25.6	3.480	25.8	3.453	25.8	3.453	26.0	3.427
004	52.8	1.734	53.2	1.722	53.2	1.722	53.6	1.709
10	43.8	1.067	43.8	2.067	43.6	2.076	43.6	2.076
11	79.8	1.202	79.8	1.202	79.4	1.207	79.4	1.207
20	95.2	1.044	95.0	1.046	94.6	1.049	94.6	1.048

	GLC2200°C				GLC2600°C			
	RAW		PEEL		RAW		PEEL	
hkl	2θ°	d(Å)	2θ°C	d(Å)	2θ°C	d(Å)	2θ°	d(Å)
002	25.8	3.453	26.0	3.427	29.5	3.440	26.1	3.414
004	53.6	1.710	53.8	1.704	53.6	1.710	53.8	1.704
10	43.6	2.076	53.5	2.080	43.4	2.985	43.4	2.085
11	79.0	1.212	79.4	1.207	79.2	1.209	79.0	1.212
20	94.6	1.049	94.5	1.050	94.6	1.049	94.2	1.052

THEORETICAL VALUES FOR GRAPHITE

hkl	(002)	(004)	(100)	(110)	(200)
2θ°	26.6°	54.8°	42.2°	77.6°	92.7°
d(Å)	3.354	1.677	2.132	1.231	1.066

TABLE 4.2.B
STRAIN ANALYSIS (NEUTRON DATA)

	L_c(Å)				L_a(Å)					
	L_{002}		L_{004}		L_{10}		L_{11}		L_{20}	
TEMP°C	RAW	PEEL	RAW	PEEL	RAW	PEEL	RAW	PEEL	RAW	PEEL
1200	8.1	15.5	NSR*	19.5	21.1	34.0	17.3	22.0	NSR	26.6
1800	14.3	17.9	NSR	21.0	34.0	41.6	23.2	28.2	NSR	30.7
2200	17.6	21.2	NSR	21.5	37.0	46.5	27.8	31.3	NSR	37.2
2600	20.9	21.5	NSR	22.0	38.3	50.2	28.0	35.6	NSR	41.0

*NSR = NOT SUFFICIENTLY RESOLVED

TEMPERATURE °C		1200	1800	2200	2600
L_a(intercept)(Å)		47.1	54.8	62.0	64.1
STRAIN (diff.)	(10)	28	24	24	22
	(11)	53	49	50	44

$$L_{c_{1/2}} = (0.89 \times \lambda)/B_{1/2} \cos\theta_c$$

$$L_{a_{1/2}} = (1.77 \times \lambda)/B_{1/2} \cos\theta_a$$

TABLE 4.2.C
PEAK BREADTH ANALYSIS (NEUTRON DATA)

	L_c(Å)			L_a(Å)				DIFF.
	(002)	(004)	Extrap. for (002) and (004)	(10)	(11)	(20)	Extrap. for (10) and (11)	L_a-L_c
TEMP.	PEEL	PEEL		PEEL	PEEL	PEEL		(Extrap.)
*1200								
$\Delta 2\theta$	5.2°	4.5°	--	--	--	--	--	--
$\beta_{1/2}\cos\theta$	0.089	0.070	0.095	0.080	0.124	0.103	0.058	--
L(Å)	15.5Å	19.5Å	14.5Å	34.0Å	22.0Å	26.6Å	47.1Å	32.6Å
*1800								
$\Delta 2\theta$	4.5°	4.2°	--	--	--	--	--	--
$\beta_{1/2}\cos\theta$	0.077	0.065	0.080	0.066	0.097	0.089	0.050	--
L(Å)	17.9Å	21.0Å	17.1Å	41.6	28.2	30.7	54.8	37.7Å
2200-60								
$\Delta 2\theta$	3.8°	4.1°	--	--	--	--	--	--
$\beta_{1/2}\cos\theta$	0.065	0.064	0.065	0.058	0.087	0.074	0.044	--
L(Å)	21.2Å	21.5Å	21.1Å	45.6	31.3	37.2	62.0	40.9Å
2600-4								
$\Delta 2\theta$	3.7°	4.0°	--	--	--	--	--	--
$\beta_{1/2}\cos\theta$	0.064	0.062	0.064	0.054	0.077	0.067	0.043	--
L(Å)	21.5Å	22.0Å	21.4Å	50.2	35.6	31.0	64.1	42.4Å

*times up to 156 hours.

$\beta_{1/2} = (2\theta_2 - 2\theta_1) = \Delta 2\theta$ at half maximum.

TABLE 4.3
RATIO OF HYDROGEN TO CARBON ATOMS IN GLC

T°C		1200-9	1800-9	2200-15	2600-4	2600-4*	HOPG
ANL	$\frac{\sigma}{m}$	0.1733	0.1610	0.1587	0.1543	0.1592	0.1474
ANL	$\frac{n_h}{n_c}$	0.39	0.20	0.017	0.010	0.18	0.0
ANL	$\frac{n_{hc}}{B}$	2.93×10^{-5}	2.04×10^{-5}	1.93×10^{-5}	2.17×10^{-5}	1.20×10^{-5}	0.0

T°C		1200-156	1800-10	2200-36	2600-4	2600-4*	HOPG
NBS	$\frac{n_h}{n_c}$	0.034	0.015	0.010	0.010	--	--
NBS	$\frac{n_h}{n_c}$	0.039	0.024	0.018	--	0.018	--
NBS	B (cps)	1330	980	880	830	830	--

*Data measured repeatedly for reproducibility.

$\frac{\sigma}{m}$ = Cross-section per unit mass.

$\frac{n_h}{n_c}$ = no. of hydrogen atoms/no. of carbon atoms = n_{hc}.

B(cps) = background scattering from WAND data.

TABLE 4.4.A

HTt hrs.	GLC1000°C SAMPLE NO.	Thickness cm	TRANSMISSION	$\overline{R}_g$(Å)	$\overline{R}_g^3$ (Å^3)
0	203	0.286	0.151	0.99±0.06	726
0	203	0.286	0.151	9.12±0.06	759
0	203	0.286	0.151	9.04±0.08	739
64	A4	0.282	0.153	9.05±0.06	741
64	A4	0.282	0.153	9.05	741
128	153	0.276	0.152	9.22±0.08	783

Notes: $\overline{R}_{go} = \overline{R}_{gi} = 9.0\pm0.2$Å

$(\overline{R}_{go})^3 = (\overline{R}_{gi})^3 = 729\pm11$Å^3

TABLE 4.4.B

HTt hrs.	GLC1200°C SAMPLE NO.	Thickness cm	TRANSMISSION	$\overline{R}_g$(Å)	$\overline{R}_g^3$ (Å^3)
4	316	0.278	0.148	10.42	1130
9	82	0.176	0.321	10.80	1260
9*	142A	0.172	0.356	10.70	1225
9*	240	0.280	0.168	10.26	1081
12	317	0.273	0.179	10.47	1148
24	318	0.272	0.186	10.55	1205
48	319	0.274	0.186	10.55	1175
72	320	0.278	0.179	10.48	1152
96	321	0.264	0.164	10.45	1141

*Thin samples

$\overline{R}_{go} = 10.47\pm0.04$Å

$(\overline{R}_{go})^3 = 1148\pm21$Å^3

TABLE 4.4.C

HTt hrs.	GLC1300°C SAMPLE NO.	Thickness cm	TRANSMISSION	$\bar{R}_g$(Å)	$\bar{R}_g^3$ (Å^3)
0	332	0.273	0.349	10.57	1180

$(\bar{R}_{go}) = (\bar{R}_g) = 10.57 \pm 0.05$Å

$(\bar{R}_{go})^3 = 1180 \pm 15$Å^3

TABLE 4.4.D

HTt hrs.	GLC1400°C SAMPLE NO.	Thickness cm	TRANSMISSION	$\bar{R}_g$(Å)	$\bar{R}_g^3$ (Å^3)
0	1A	0.168		12.25	1839
72	9A	0.172		12.39	1901

$\bar{R}_{go} = 12.30 \pm 0.10$Å

$(\bar{R}_{go})^3 = 1870 \pm 45$Å^3

TABLE 4.4.E

GLC1600°C

HTt hrs.	SAMPLE NO.	Thickness cm	TRANSMISSION	$\bar{R}_g$(Å)	$\bar{R}_g^3$ (Å^3)
0	1C	0.170		13.34±0.25	2373
48	9C	0.174		13.76	2602
48	9C	0.174		13.89	2678

$\bar{R}_{go}$ = 13.66±0.29Å

$(\bar{R}_{go})^3$ = 2551±160Å^3

TABLE 4.4.F

GLC1800°C

HTt hrs.	SAMPLE NO.	Thickness cm	TRANSMISSION	$\bar{R}_g$(Å)	$\bar{R}_g^3$ (Å^3)
9	252	0.176	0.314	14.92	3324
9	251	0.171	0.301	13.99	3211
100	825	0.174	0.311	14.75	2740

$\bar{R}_{go}$ = 14.56±0.49Å

$(\bar{R}_{go})^3$ = 3088±313Å^3

TABLE 4.4.G

HTt hrs.	GLC2000°C SAMPLE NO.	Thickness cm	TRANSMISSION	$\bar{R}_g$(Å)	$\bar{R}_g^3$ (Å^3)
0	301	0.284	0.165	14.37	2966
6	302	0.284	0.168	14.74	3203
12	303A	0.286	0.160	15.10	3435
24	304	0.284	0.164	15.03	3395
36	305	0.284	0.156	15.16	3484
48	306	0.284	0.164	15.21	3519
72	307	0.280	0.161	15.39	3646
96	308	0.276	0.174	15.73	3894

$(\bar{R}_{go}) = 14.68 \pm 0.08$Å

$(\bar{R}_{go})^3 = 3164$Å^3

TABLE 4.4.H

HTt hrs.	GLC2100°C SAMPLE NO.	Thickness cm	TRANSMISSION	$\bar{R}_g$(Å)	$\bar{R}_g^3$ (Å^3)
0	331	0.284	0.161	13.89	2681
3	337	0.285	0.162	14.54	3074
6	324A	0.286	0.159	14.85	3275
12	325	0.285	0.161	14.97	3355
18	327	0.287	0.162	15.12	3460
24	328	0.285	0.155	15.10	3441
30	330	0.285	0.158	15.32	3593
36	326	0.285	0.158	15.37	3628

$(\bar{R}_{go}) = 14.35$Å

$(\bar{R}_{go})^3 = 2979$Å^3

TABLE 4.4.I

GLC2200°C

HTt hrs.	SAMPLE NO.	Thickness cm	TRANSMISSION	$\bar{R}_g$(Å)	$\bar{R}_g^3$ (Å^3)
0	215	0.283	0.167	15.27	3652
6	227	0.272	0.171	16.54	4521
15	216A	0.270	0.163	16.81	4746
24	219	0.286	0.159	17.57	5423
48	222	0.278	0.169	18.09	5921
60	223	0.168	0.351	19.12	6990

$(\bar{R}_{go}) = 15.88Å$
$(\bar{R}_{go})^3 = 4385Å^3$

TABLE 4.4.J

GLC2300°C

HTt hrs.	SAMPLE NO.	Thickness cm	TRANSMISSION	$\bar{R}_g$(Å)	$\bar{R}_g^3$ (Å^3)
0		0.259	0.198	15.45	3691
1		0.280	0.164	15.60	3724
2		0.273	0.161	15.66	3840
4		0.278	0.160	15.88	4007
6	323	0.286	0.159	15.97	4073
12	236	0.274	0.162	16.31	4339
24	284	0.261	0.198	17.27	5151
48	287	0.256	0.191	17.40	5268

$\bar{R}_{go} = 15.65Å$
$(\bar{R}_{go})^3 = 3835Å^3$

TABLE 4.4.K

GLC2400°C

HTt hrs.	SAMPLE NO.	Thickness cm	TRANSMISSION	$\bar{R}_g$(Å)	$\bar{R}_g^3$ (Å^3)
0	310	0.286	0.157	18.37	6199
6	312	0.286	0.157	19.82	7791
15	210	0.278	0.175	19.94	7925
24	212	0.171	0.335	20.82	9026
30	213	0.168	0.340	22.34	11,154

$\bar{R}_{go} = 19.21 \pm 22$Å
$(\bar{R}_{go})^3 = 7092 \pm 240$Å^3

TABLE 4.4.L

GLC2500°C

HTt hrs.	SAMPLE NO.	Thickness cm	TRANSMISSION	$\bar{R}_g$(Å)	$\bar{R}_g^3$ (Å^3)
0		0.132	0.437	18.98	6838
9		0.126	0.461	20.74	8921
15		0.124	0.463	21.17	9488
20		0.206	0.270	21.71	10,232
30		0.134	0.458	22.31	11,103

$\bar{R}_{go} = 19.37$Å
$(\bar{R}_{go})^3 = 7263$Å^3

TABLE 4.4.M

GLC2600°C

HTt hrs.	SAMPLE NO.	Thickness cm	TRANSMISSION	$\bar{R}_g$(Å)	$\bar{R}_g^3$ (Å^3)
0	228	0.286	0.161	20.39	8479
4	247	0.294	0.162	21.65	10,153
10	20-OS	0.212	0.263	23.51	13,001
10	20-OS	0.212	0.263	23.55	13,050

$\bar{R}_{go}$ = 20.39Å
$(\bar{R}_{go})^3$ = 8422Å^3

TABLE 4.4.N

GLC2700°C

HTt hrs.	SAMPLE NO.	Thickness cm	TRANSMISSION	$\bar{R}_g$(Å)	$\bar{R}_g^3$ (Å^3)
0	35-OS	0.204	0.276	22.90	12,009
2	F	0.182	0.317	23.60	13,144
2	F	0.182	0.317	23.62	13,178
4	32-OS	0.266	0.240	24.27	14,302
4	32-OS	0.238	0.231	24.27	14,291
6	33-OS	0.208	0.269	24.33	14,400
10	36-OS	0.154	0.368	25.14	15,879

$\bar{R}_{go}$ = 23.08Å
$(\bar{R}_{go})^3$ = 12,297Å^3

TABLE 4.4.0

HTt hrs.	GLC2800°C SAMPLE NO.	Thickness cm	TRANSMISSION	$\bar{R}_g$(Å)	$\bar{R}_g^3$ (Å^3)
2	23-0S	0.226	0.236	24.29	14,331
4	59-0S	0.234	0.239	24.88	15,401

$\bar{R}_{go}$ = 23.67Å
$(\bar{R}_{go})^3$ = 13,261Å^3

TABLE 4.4.P
(R_g) DEPENDENCE ON HEAT-TREATMENT TEMPERATURE (HTT)

T°C	$(\bar{R}_{g_o})^3$ (Å^3)	$(\Delta\bar{R}_{g_o})^3$	$\frac{(\Delta\bar{R}_{g_o})}{(\Delta\bar{R}_{g_i})^3}$	$(\Delta\bar{R}_{g_o})$ (Å)	$\frac{(\Delta\bar{R}_{g_o})}{(R_{g_i})}$	$\delta\left(\frac{(\Delta\bar{R}_{g_o})}{(R_{g_i})}\right)$	$(\bar{R}_{g_o})$ (Å)
1000	729 **	0.0	0.0	0.0	0.0	0.0	9.0
1200	1148	419	0.575	7.48	0.83	±0.02	10.47
1300	1180	451	0.619	7.69	0.85	±0.02	10.57
1400*	1884	1155	1.584	10.49	1.16	±0.03	13.82
1600*	2640	1911	2.621	12.41	1.37	±0.05	13.82
1800*	3092	2363	3.18	13.32	1.47	±0.08	14.56
2000	3164	2435	3.31	13.45	1.49	±0.03	14.68
2100	2979	2250	3.05	13.10	1.45	±0.03	14.39
2200	4004	3275	4.41	14.85	1.64	±0.05	15.88
2300	3701	2972	4.02	14.38	1.59	±0.04	15.65
2400	7092	6363	8.62	18.53	2.05	±0.05	19.21
2500	7263	6534	8.87	18.70	2.07	±0.04	19.37
2600	8423	7694	10.36	19.74	2.18	±0.03	20.39
2700	12,297	11,568	15.63	22.62	2.50	±0.04	23.08

*Thin samples.

**$R_{g_o}^3 = \bar{R}_{g_i}^3$ for 1000°C.

$$(\Delta\bar{R}_{g_o})^3 = \left[(\bar{R}_{g_o})^3 - (\bar{R}_{g_i})^3\right].$$

TABLE 4.4.Q
ACTIVATION ENERGY CALCULATION

T°C	T°K	1/T°K	$T\times(\bar{R}_{g_o})^3$ (intercepts)	$(\bar{R}_{g_o})^3$ $(Å)^3$	K(D) (slope)	Ln[K(D)]
2000	2273	4.4×10^{-4}	7.19×10^{-6}	3164	0.017×10^{-6}	9.76
2100	2373	4.21	7.07	2979	0.035	10.47
2200	2473	4.04	9.90	4004	0.084	11.34
2300	2573	3.89	9.87	3833	0.091	11.41
2400	2673	3.74	18.96	7092	0.385	12.21
2500	2773	3.61	20.24	7263	0.385	12.86
2600	2873	3.48	24.20	8422	1.31	14.09
2700	2973	3.36	36.56	12,297	1.11	13.01
2800	3073	3.25	40.75	13,261	1.64	14.31

INTERCEPT OF $T\times(\bar{R}_{g_o})^3 = 7.2\times0.2\times10^{-6}$.

TABLE 4.4.R
R_g RELATED TO THE DIMENSIONAL CHANGE, 1 IN GLC

HTT	$(l_F)_{T,0}$	$(\Delta l)_{T,0}$	$(\Delta \bar{R}_g)_{T,0}$	$\frac{(\Delta \bar{R}_g)}{(\Delta l)_{T,0}}$	Normalized $(\Delta l)_{T,0}$
1000	5.0930*	--	--	--	--
1200	5.1003	0.0072 (cm)	7.48(Å)	1039	0.95
1300	--	--	7.69	--	--
1400	5.1119	0.0189	10.49	555	2.50
1600	5.1307	0.0377	12.41	329	4.99
1800	5.1602	0.0672	13.38	199	8.90
2000	5.1739	0.0809	13.45	166	10.72
2100	5.1781	0.0851	13.10	154	11.27
2200	5.1816	0.0886	14.85	168	11.74
2300	5.2035	0.1105	14.38	130	14.64
2400	5.2122	0.1192	18.53	156	15.79
2500	5.2320	0.1390	18.70	135	18.42
2600	5.2422	0.1490	19.74	133	19.74

$(\Delta l)_{T,0} = (l_F)_{T,0} - (l_F)_{i,0}$
*$(l_F)_{i,0}$ is the initial length at 1000° for zero time.

TABLE 4.4.S
RELATIVE R_g CHANGES RELATED TO RELATIVE DIMENSIONAL CHANGES IN GLC

T°C	$\frac{(\Delta\bar{R}_{g_o})_{T,0}}{(R_g)_{i,0}}$	$\frac{(\Delta_{l_o})_{T,0}}{(l)_{i,0}}$	NORMLZD $\frac{(\Delta_{l_o})_{T,0}}{(l)_{i,0}}$	$\frac{(\Delta\bar{R}_{g_o}/\bar{R}_{g_i})}{(\Delta l_o/l_i)}$	$(l_f)_{T,0}$	$(\Delta)_{T,0}$
1000	--	--	--	--	5.093*	--
1200	0.83+0.02	0.0014	0.10	592.9	5.100	0.0072
1300	0.85+0.02	--	--	--	--	--
1400	1.16+0.03	0.0037	0.28	313.5	5.112	0.0189
1600	1.37+0.05	0.0074	0.55	185.1	5.131	0.0377
1800	1.47+0.08	0.0132	0.98	111.4	5.160	0.0672
2000	1.49+0.03	0.0159	1.18	93.7	5.174	0.0809
2200	1.64	0.0174	1.24	86.8	5.178	0.0809
2300	1.59	0.0217	1.61	73.2	5.182	0.0886
2400	2.05+0.05	0.0234	1.74	87.6	5.204	0.1192
2500	2.07	0.0273	2.03	75.8	5.232	0.1390
2600	2.18	0.0293	2.18	74.4	5.242	0.1490

*This is the value at the reference temperature, $(l_f)_{i,0}$.

FIGURE CAPTIONS

Fig. 1.1.A Atomic structure of perfect graphite crystal. (XBL 832-8008)

Fig. 1.1.B X-ray diffraction profile from random polycrystalline graphite. (XBL 832-8008)

Fig. 1.2.A Schematic structural model for glass-like carbon (Jenkins model). (XBL 8110-6807)

Fig. 1.2.B X-ray diffraction profile from solid glass-like carbon. (XBL 8110-680)

Fig. 1.3 Lattice images of glass-like carbon heat-treated at 2700°C. (XBB 800-12199)
a) underfocused, b) focused and c) over-focused.

Fig. 1.4 Lattice images of glass-like carbon heat-treated at 2550°C: (XBB 800-12198)
a) underfocused, b) focused and c) over-focused.

Fig. 1.5 Lattice images of glass-like carbon heat-treated at 2250°C: (XBB 800-12197)
a) underfocused, b) focused and c) over-focused.

Fig. 1.6 Lattice images of glass-like carbon heat-treated at 1800°C: (XBB 800-12196)
a) underfocused, b) focused and c) over-focused.

Fig. 3.2.A X-ray line profile of PG and the measured incoherent scattering (CuK_α radiation). (XBL 832-5241)

Fig. 3.2.B X-ray line profile of GLC 2700-2 and the measured incoherent scattering (CuK_α radiation). (XBL 832-5242)

Fig. 3.2.C Complete x-ray line profiles of GLC2700 and the generated incoherent scattering (CuK_α radiation). (XBL 8110-6813A)

NOTE: NO Fig. 3.3

Fig. 3.4 The ORNL 10-m SAXS Camera with automatic specimen changer. (XBL 851-1049)

Fig. 3.4.B The ORNL Small-Angle X-ray Scattering Laboratory. (XBB 852-1618)

Fig. 4.1.A Uncorrected Wide Angle X-ray Diffraction (WAXD) line profiles for GLC1800 - 0 and 48 hours. (XBL 8410-7435)

Fig. 4.1.B Uncorrected Wide Angle X-ray Diffraction (WAXD) 002 peak profiles for GLC1200, 1800 and 2600°C. (XBL 8410-7436)

Fig. 4.1.C Uncorrected Wide Angle X-ray Diffraction (WAXD) 002 peak profiles for GLC2200 - 0 and 60 hours. (XBL 8410-7437)

Fig. 4.1.D Incoherent (Compton) background scattering in two samples - GLC1200 and GLC2600. (XBL 8410-7438)

Fig. 4.1.E Raw and corrected 002 peak x-ray profile for GLC1200. (XBL 8410-7439)

Fig. 4.1.F Raw and corrected 002 peak x-ray profile for GLC1800. (XBL 8410-7440)

Fig. 4.1.G Raw and corrected 002 peak x-ray profile for GLC2600 - 4. (XBL 8410-7441)

Fig. 4.1.H X-ray profile of GLC2600-4 corrected for the polarization and the atomic scattering factors, but not for the Lorentz factor. (XBL 8410-7442)

Fig. 4.1.I Interlayer spacings in heat-treated glass-like carbons. (XBL 8410-7443)

Fig. 4.1.J Interlayer (stacking) sizes as a function of heat-treatment temperature in glass-like carbons. (XBL 8410-7444)

Fig. 4.1.K Neutron diffraction profiles and incoherent (background) scattering (for GLC1000) as a function of HTt. (XBL-8410-7445

Fig. 4.1.L Neutron diffraction profiles and incoherent (background) scattering (for GLC1000 - 150, GLC1800 - 100, GLC2200 - 36, and GLC2600 - 4) as a function of HTT. (XBL 8410-7446)

Fig. 4.1.M Neutron diffraction profiles (for GLC1200) corrected for small angle scattering and background. (XBL 8410-7447)

Fig. 4.1.N Neutron diffraction profiles (for GLC1800) corrected for small angle scattering and background. (XBL 8410-7448)

Fig. 4.1.O Neutron diffraction profiles (for GLC2200) corrected for small angle scattering and background. (XBL 8410-7449)

Fig. 4.1.P Neutron diffraction profiles (for GLC2600-4) corrected for small angle scattering and background. (XBL 8410-7450)

Fig. 4.1.Q Incoherent neutron scattering as a function of HTT for 1000 and 2500°C. (XBL 833-5433)

Fig. 4.1.R Effect of corrections and "Peel-Off" analysis on the neutron line profile of GLC1200°C. (XBL 8410-7451)

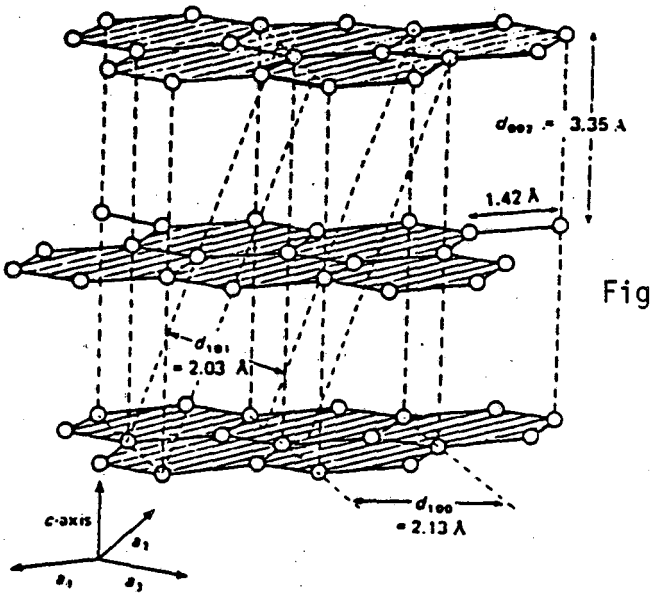

Fig. 1.1.A

. Atomic structure of a perfect graphite crystal.

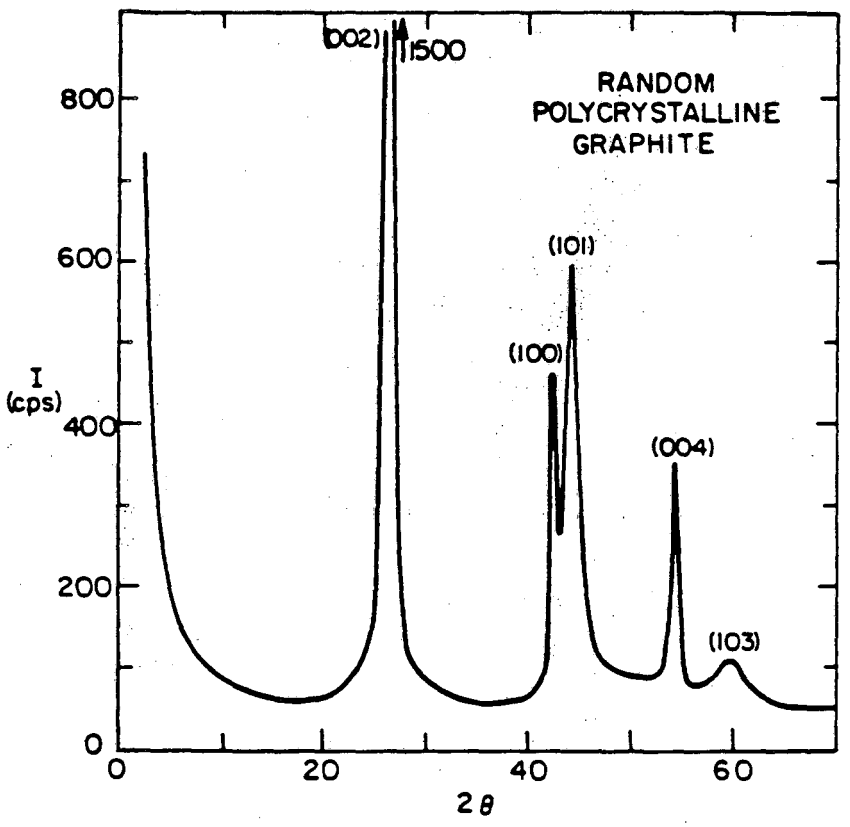

XBL 832-8008

Fig. 1.1.B

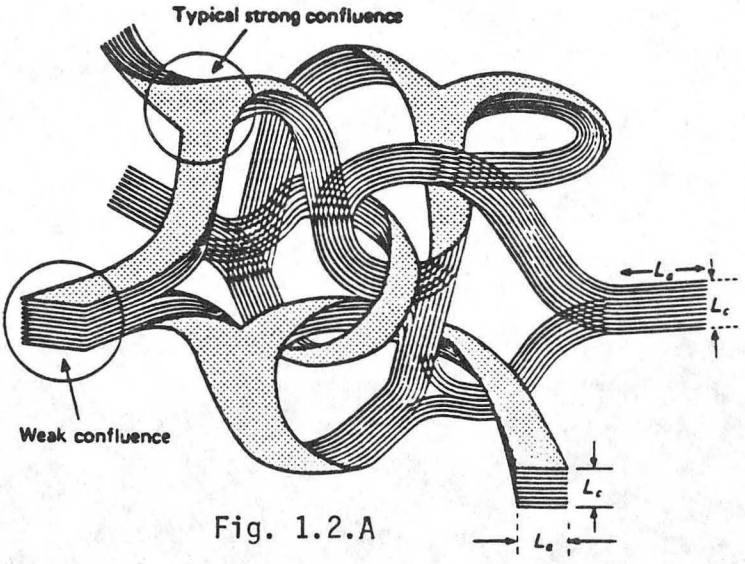

Fig. 1.2.A

Schematic structural model for a glassy carbon.

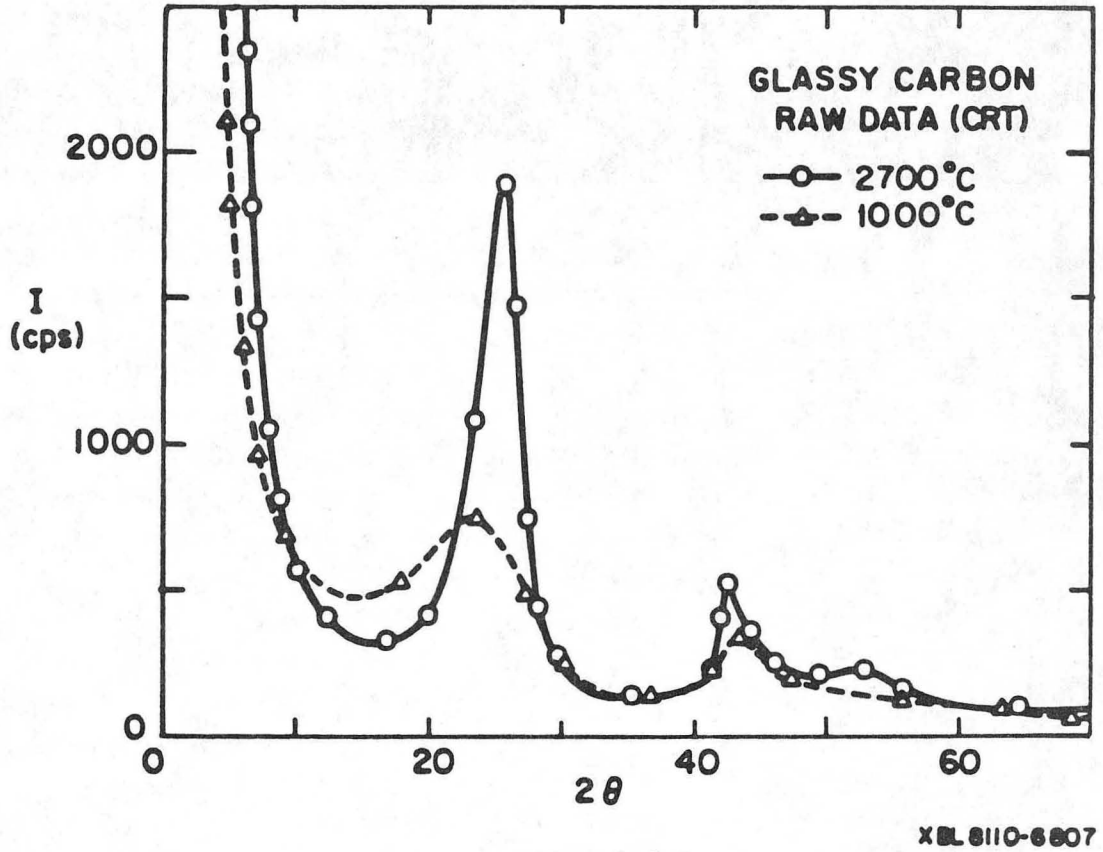

Fig. 1.2.B

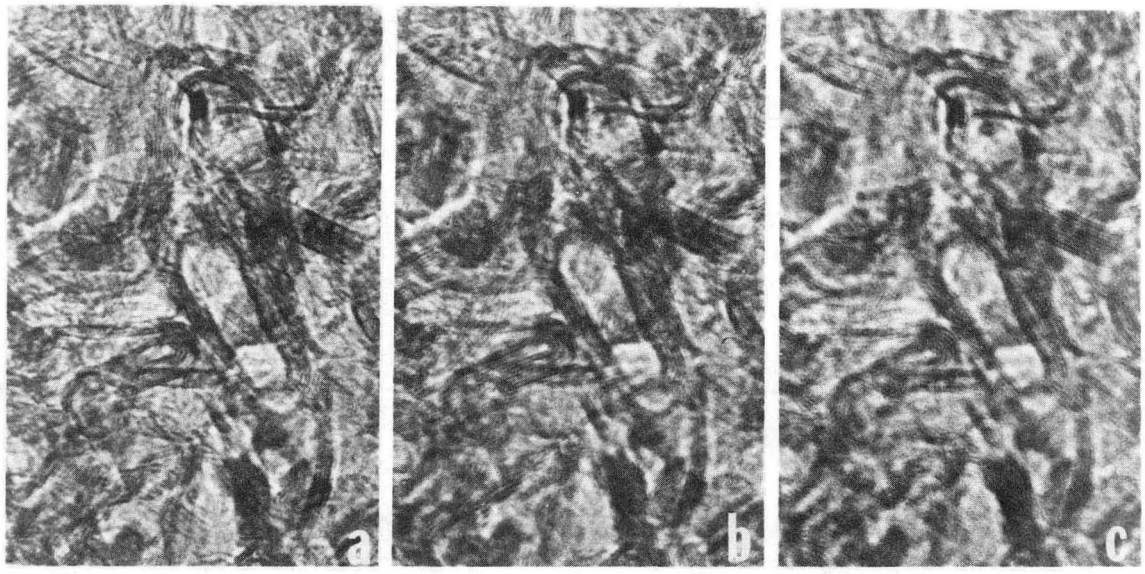

XBB 800-12199

Fig. 1.3

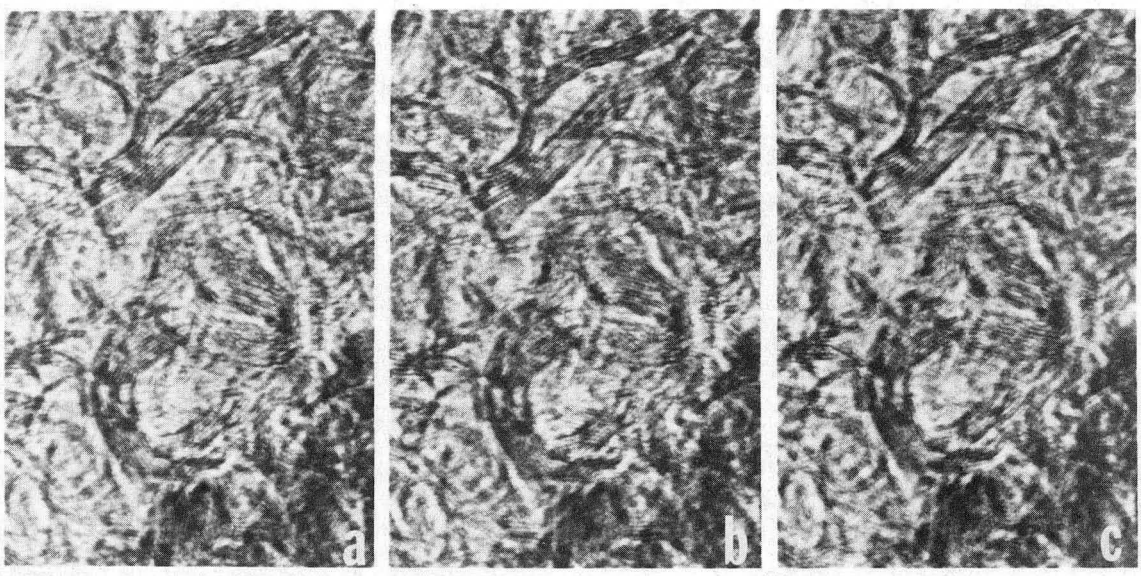

XBB 800-12198

Fig. 1.4

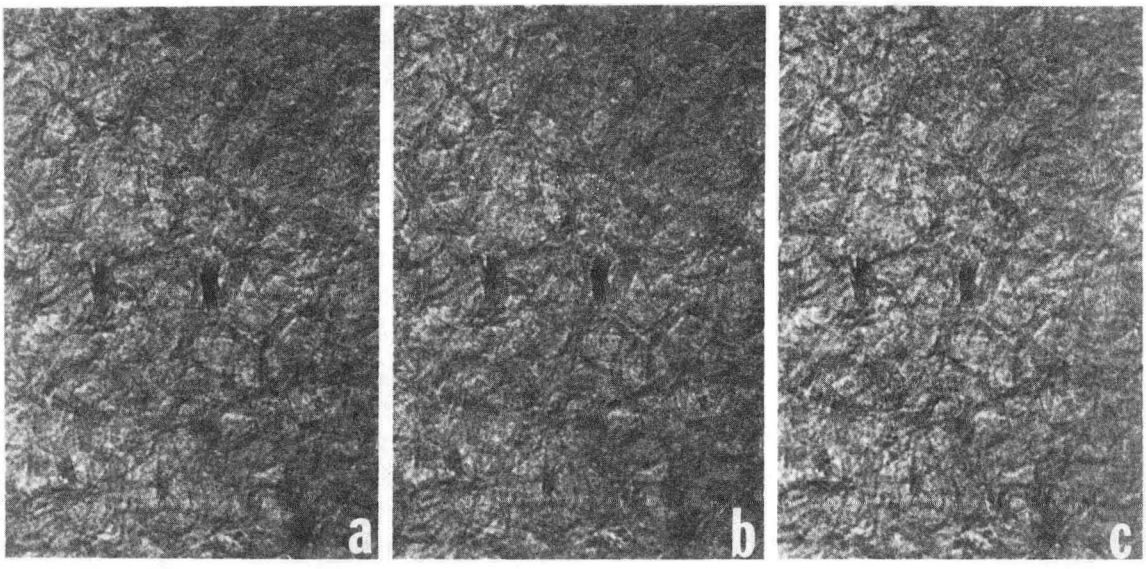

XBB 800-12197

Fig. 1.5

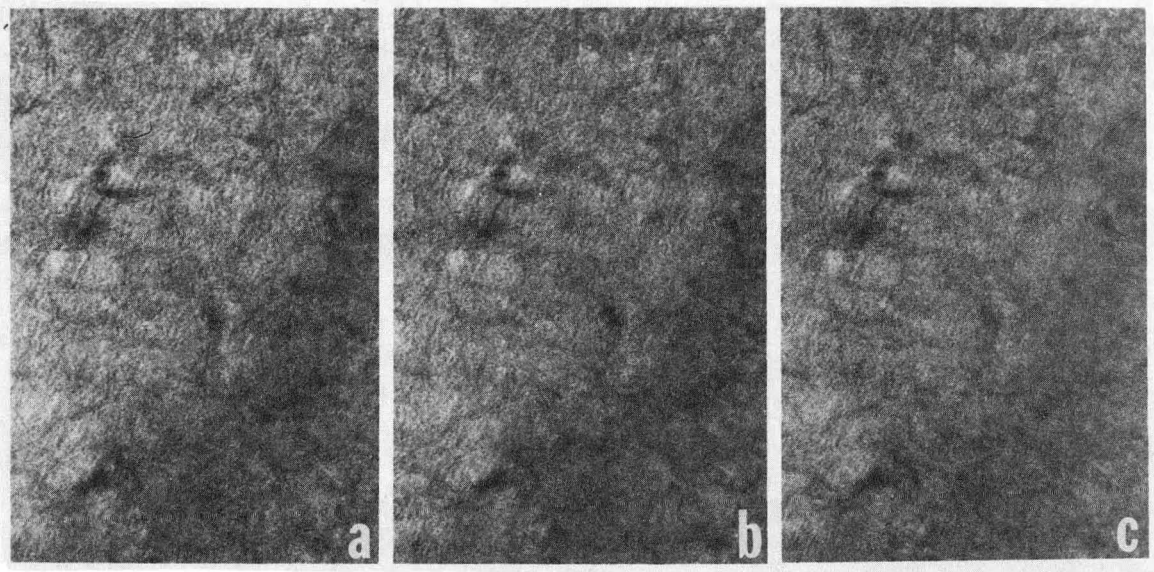

XBB 800-12196

Fig. 1.6

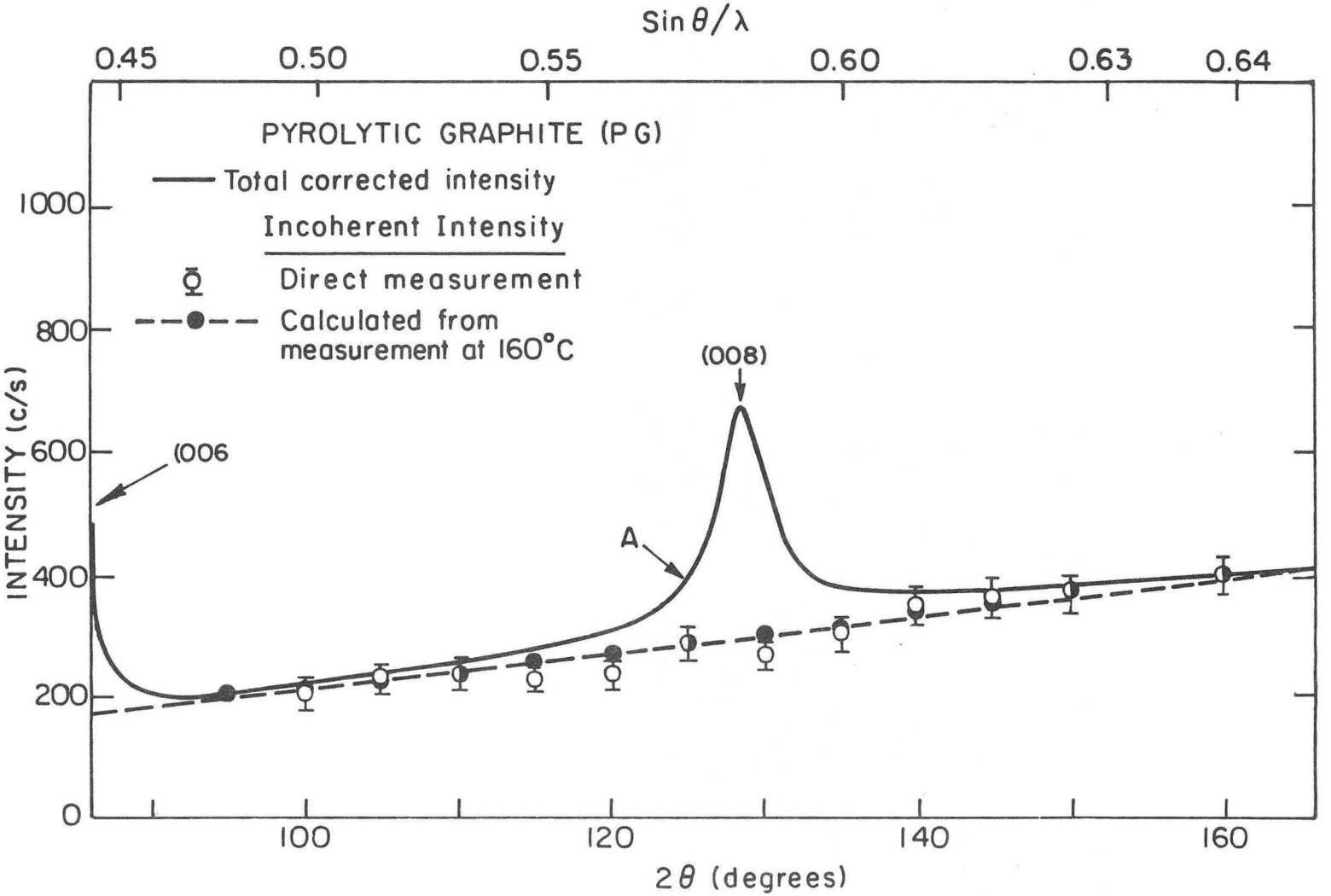
Sin θ/λ
0.45
0.50
0.55
0.60
0.63
0.64
PYROLYTIC GRAPHITE (PG)
Total corrected intensity
Incoherent Intensity
Direct measurement
Calculated from measurement at 160°C
(008)
(006
A
INTENSITY (c/s)
1000
800
600
400
200
0
100
120
140
160
2θ (degrees)
XBL 832-5241

Fig. 3.2.A

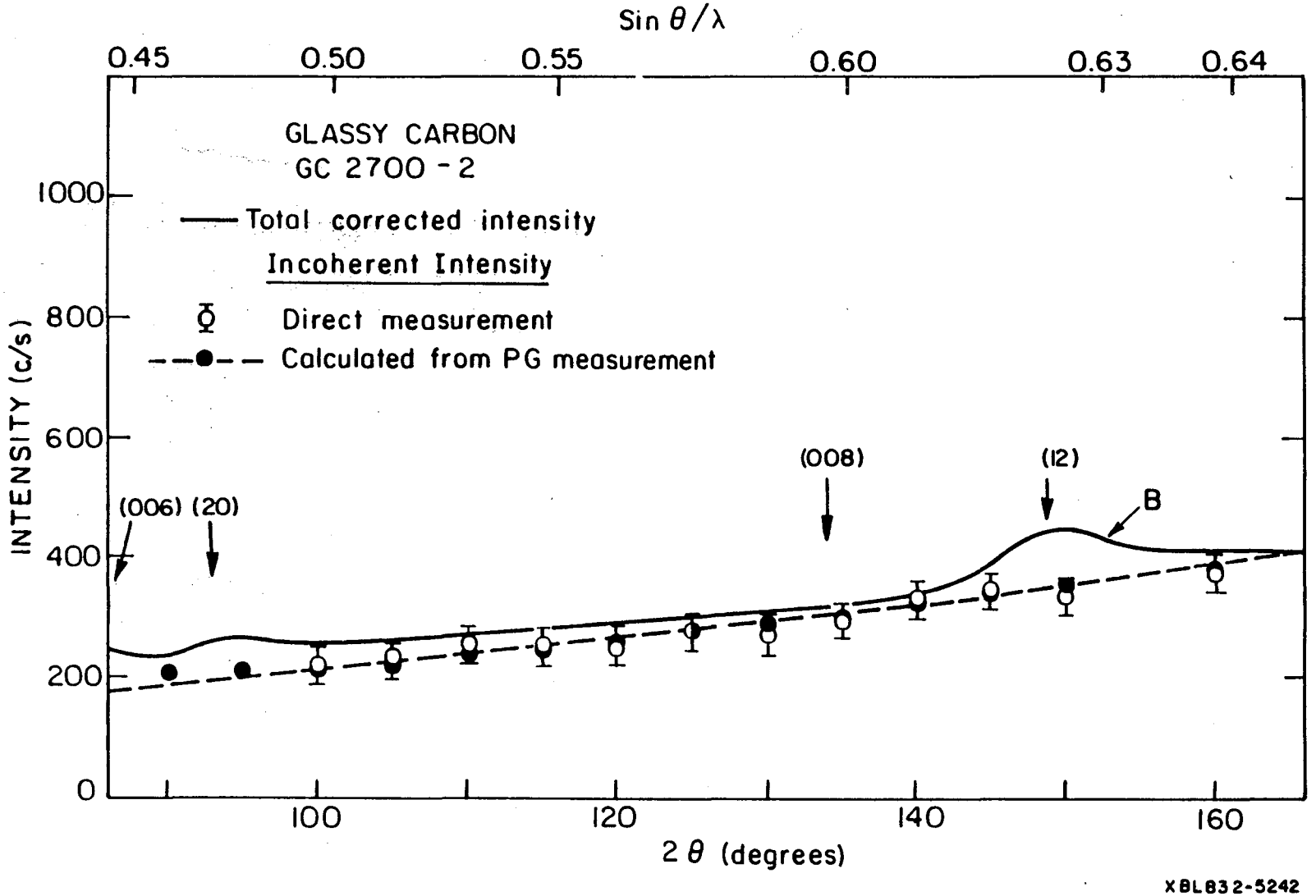
Sin θ/λ
0.45
0.50
0.55
0.60
0.63
0.64
GLASSY CARBON
GC 2700 - 2
Total corrected intensity
Incoherent Intensity
Direct measurement
Calculated from PG measurement
INTENSITY (c/s)
1000
800
600
400
200
0
(006)
(20)
(008)
(12)
B
100
120
140
160
2 θ (degrees)
XBL832-5242

Fig. 3.2.B

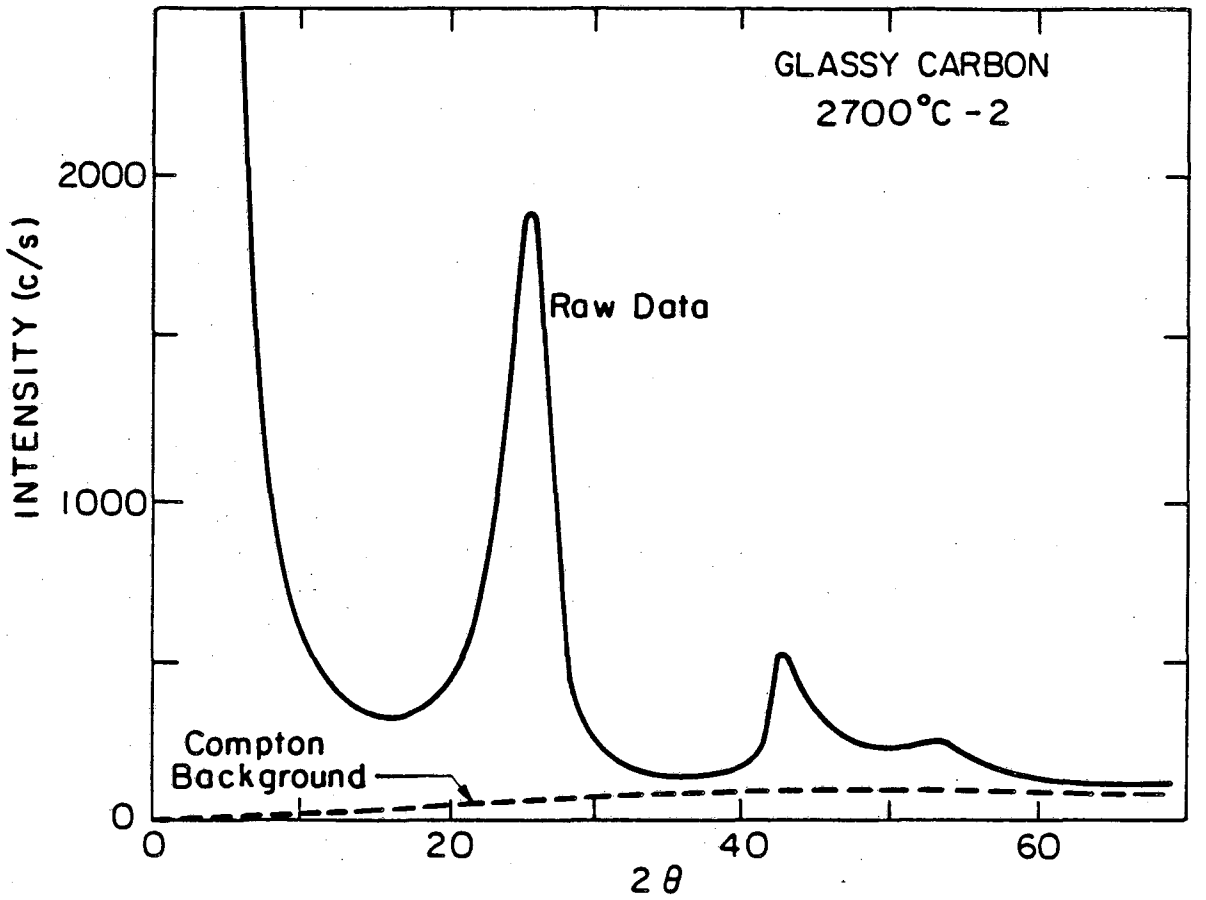
GLASSY CARBON
2700°C -2
INTENSITY (c/s)
2000
1000
0
Raw Data
Compton
Background
0
20
40
60
2θ
XBL 8110-6813A

Fig. 3.2.C

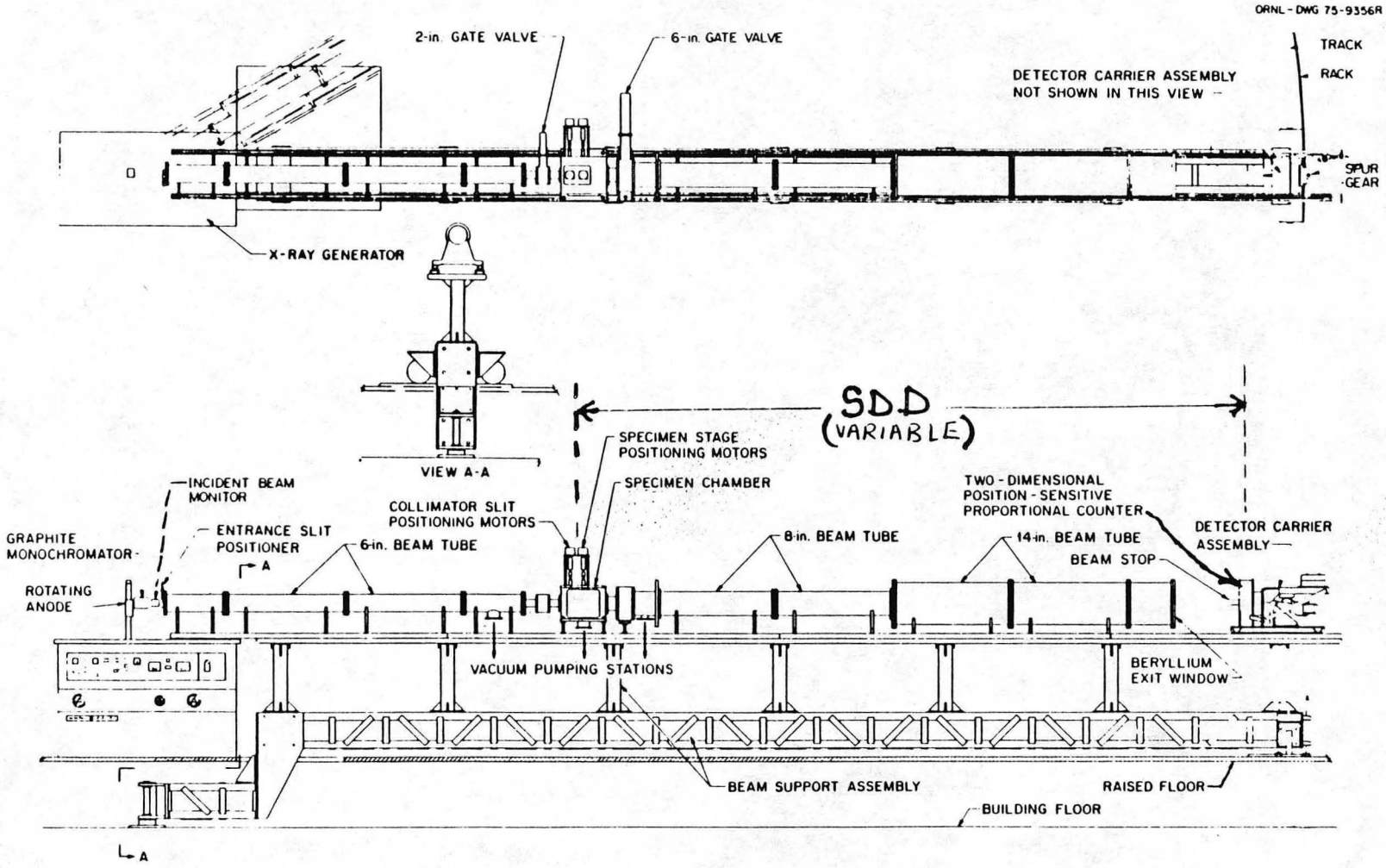

The ORNL 10-m SAXS camera.

Fig. 3.4

XBL 851-1049

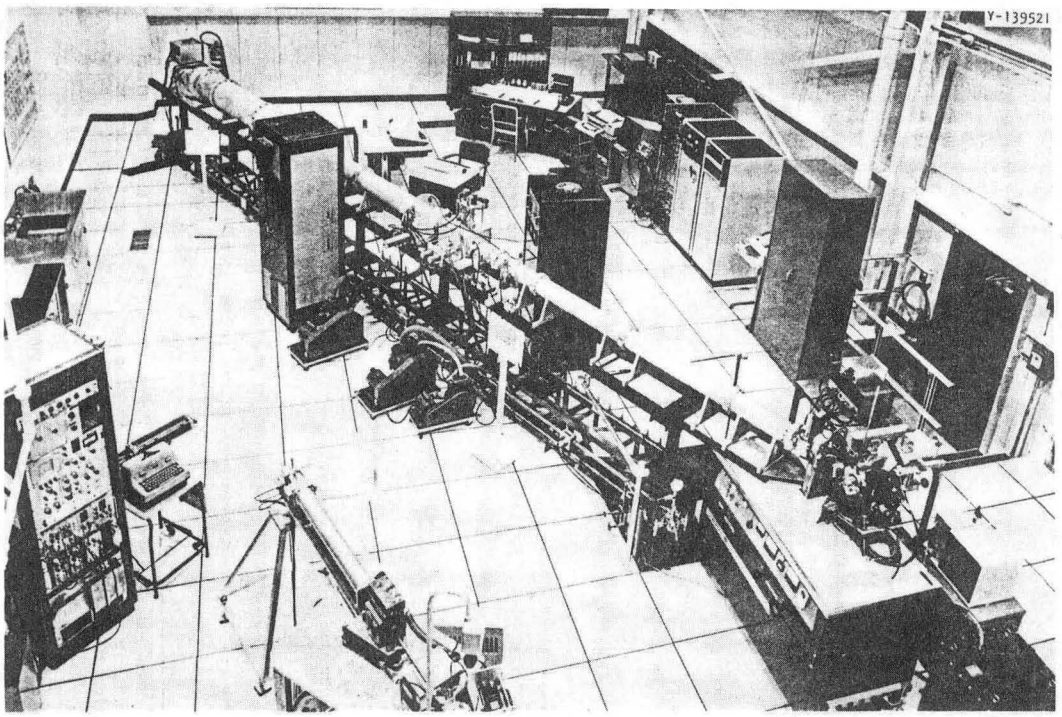

The ORNL Small-Angle X-Ray Scattering Laboratory. The main spectrometer components are identified in Fig. 2. In the upper right are the analog signal processing electronics, computer system, operator and user consoles, and the graphics terminal.

XBB 852-1618

Fig. 3.4.B

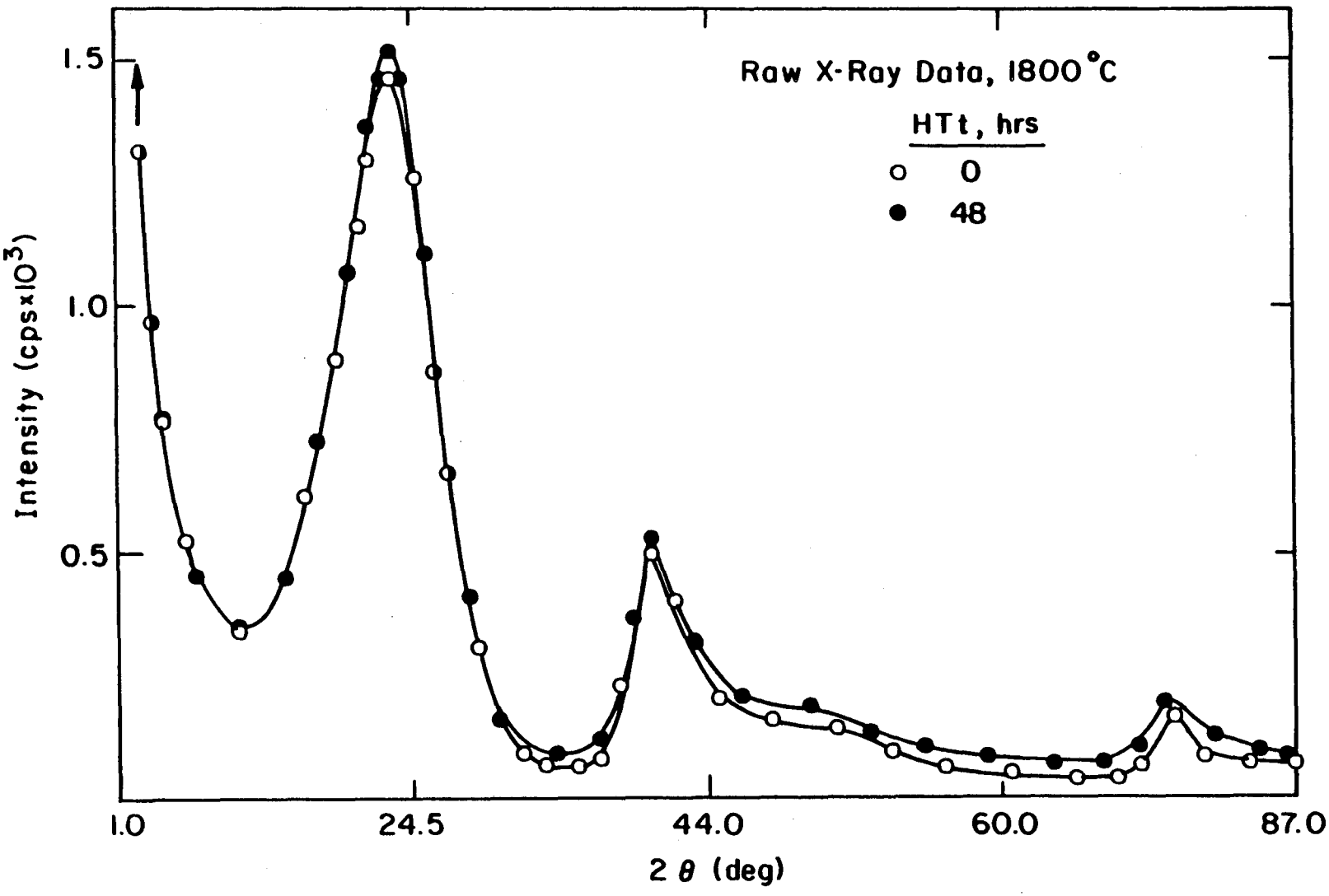

Fig. 4.1.A

XBL 8410-7435

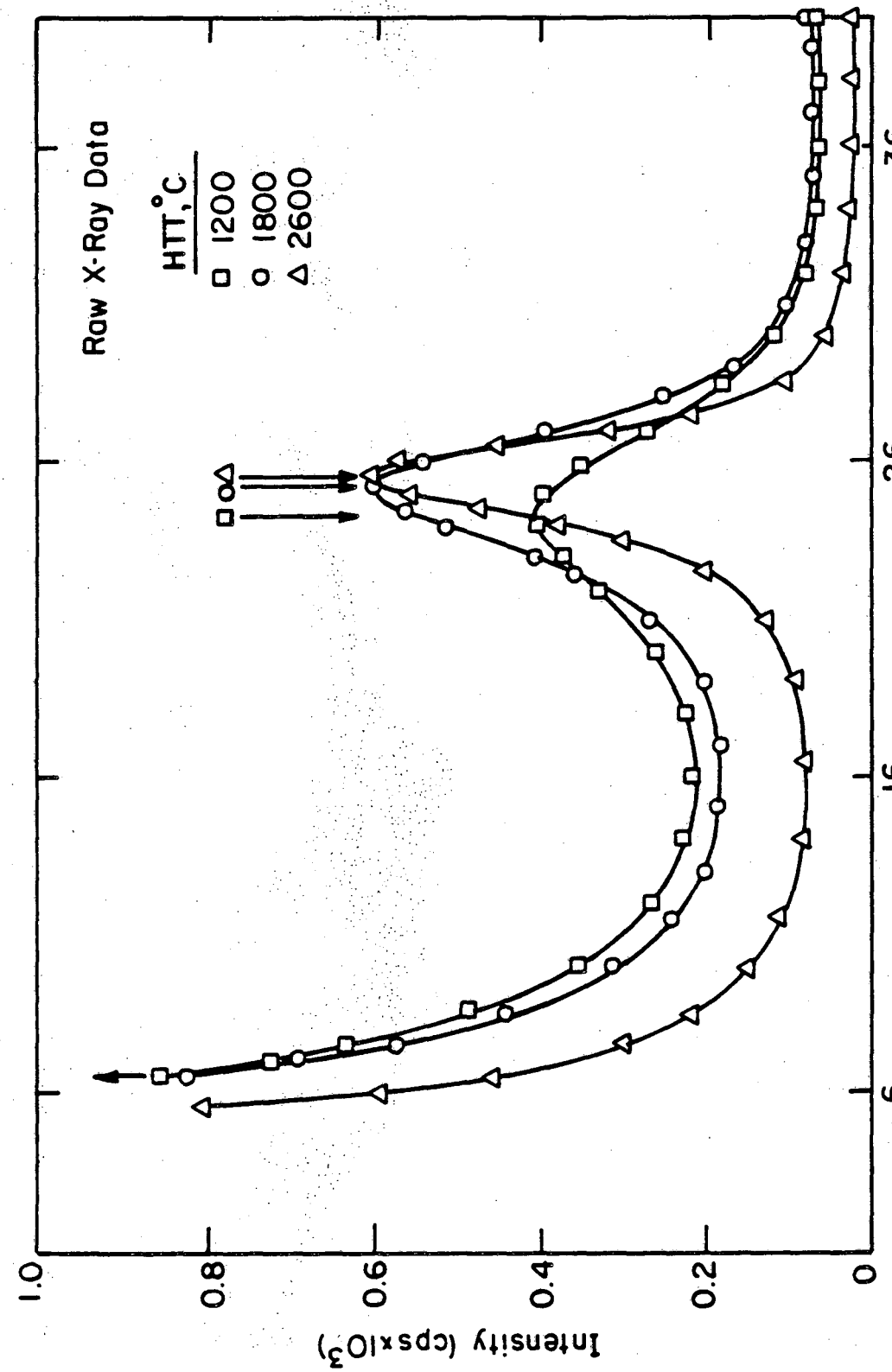
Raw X-Ray Data
HTT, °C
□ 1200
○ 1800
△ 2600
Intensity (cps x 10³)
1.0
0.8
0.6
0.4
0.2
0
6
16
26
36
2θ (deg)
XBL8410-7436

Fig. 4.1.B

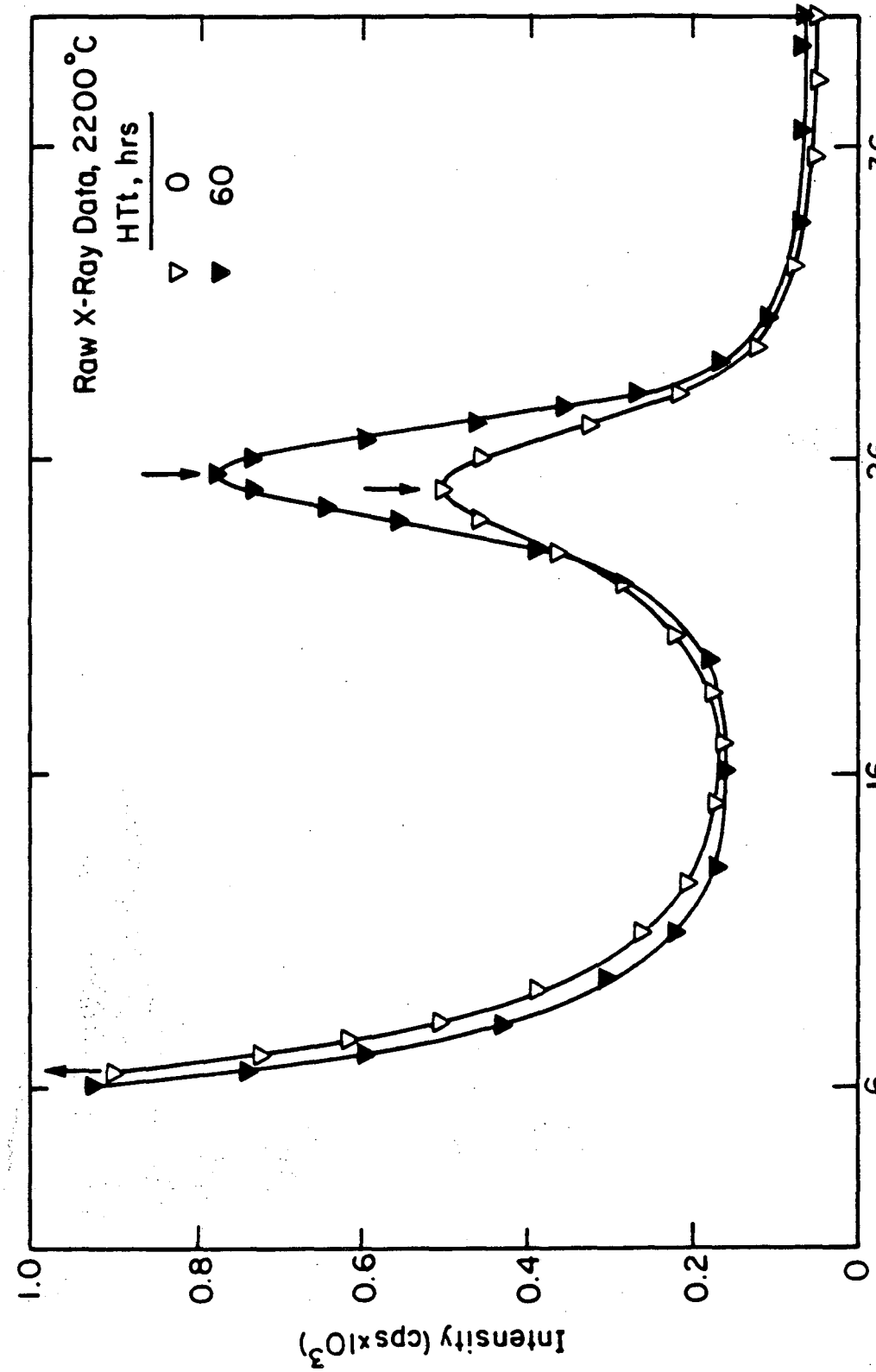

XBL8410-7437

Fig. 4.1.C

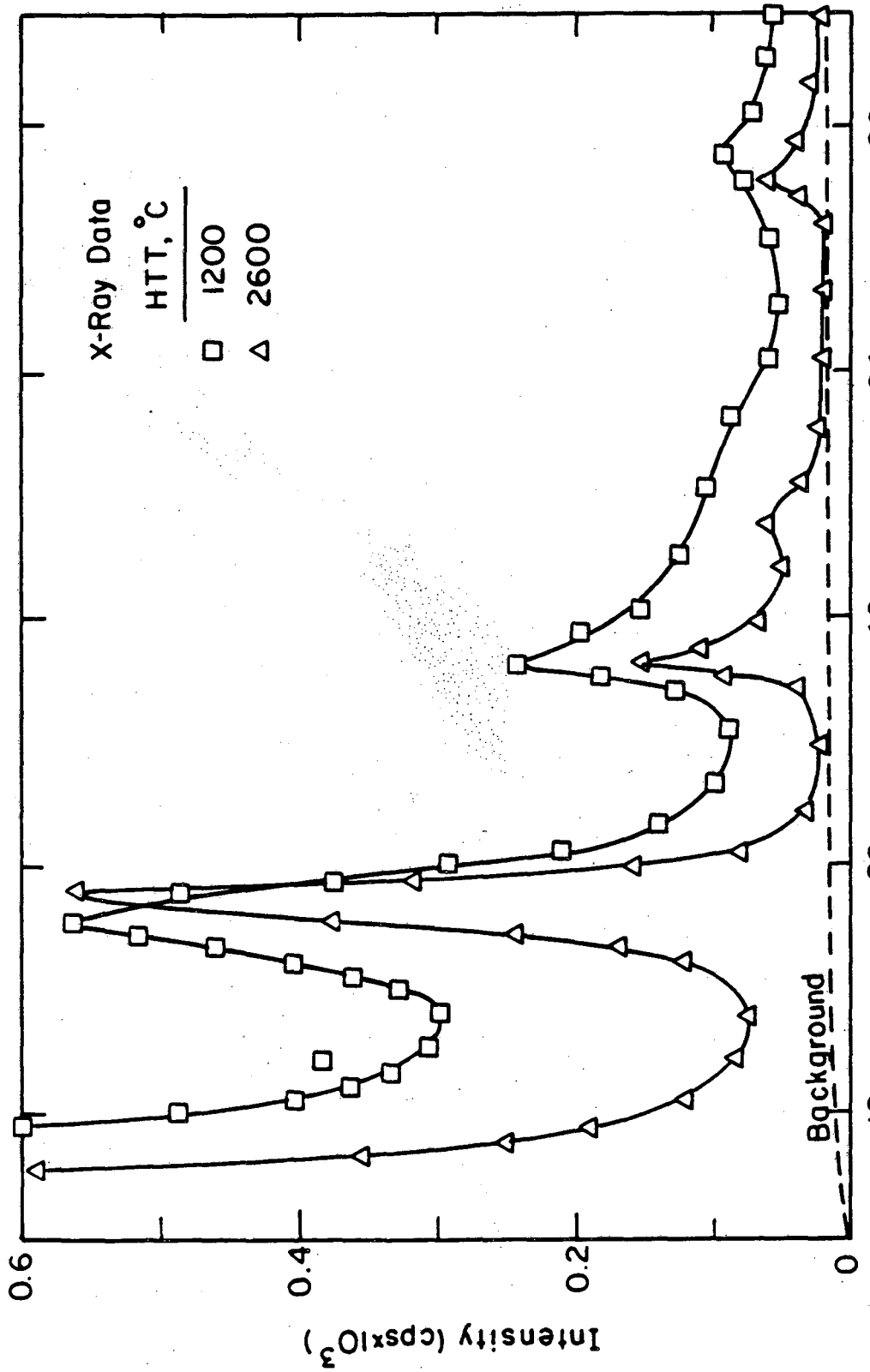
X-Ray Data
HTT, °C
1200
2600
Background
Intensity (cps x 10³)
0
0.2
0.4
0.6
10
28
46
64
82
2θ (deg)
XBL 8410-7438

Fig. 4.1.D

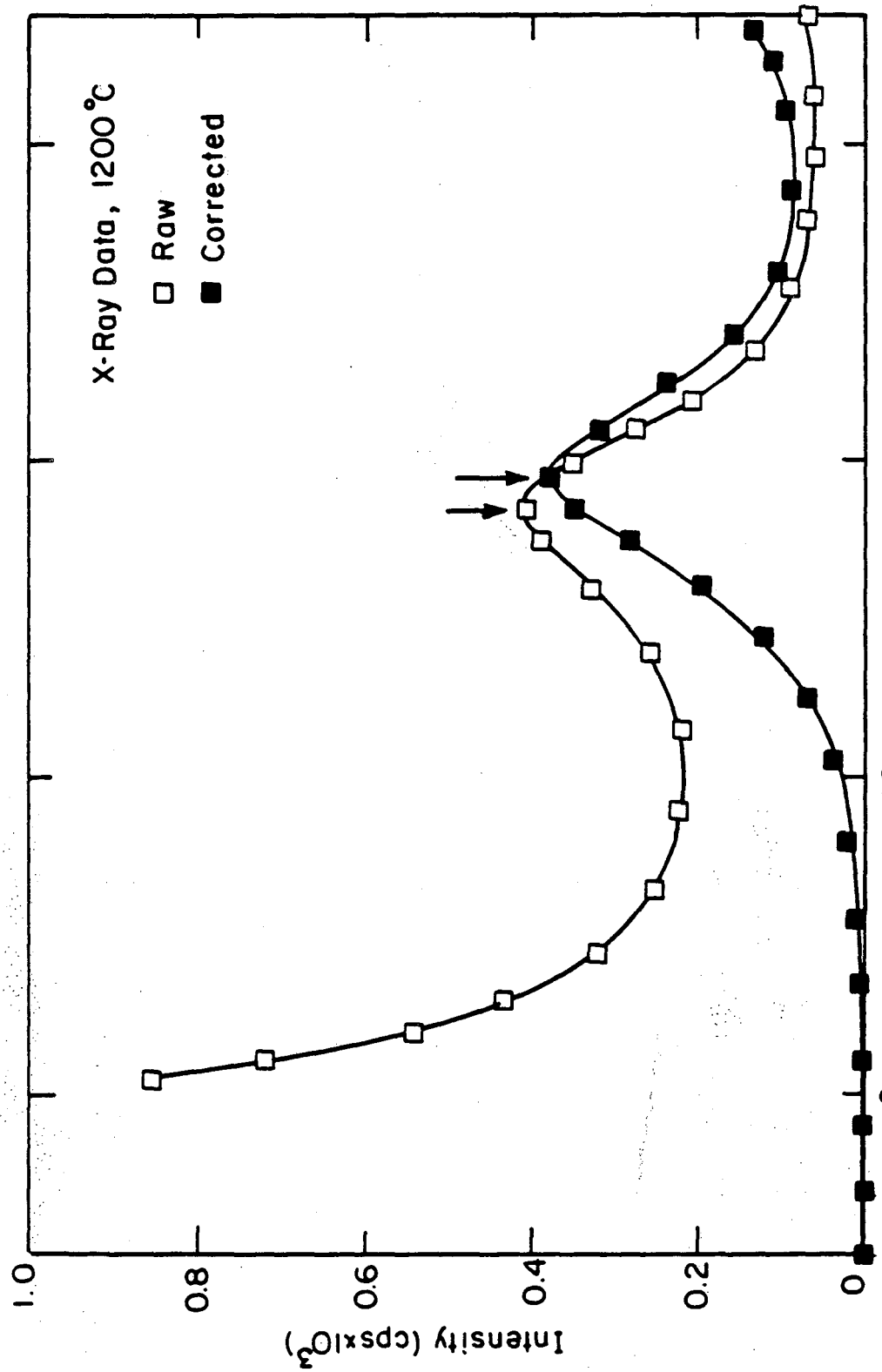

XBL 8410-7439

Fig. 4.1.E

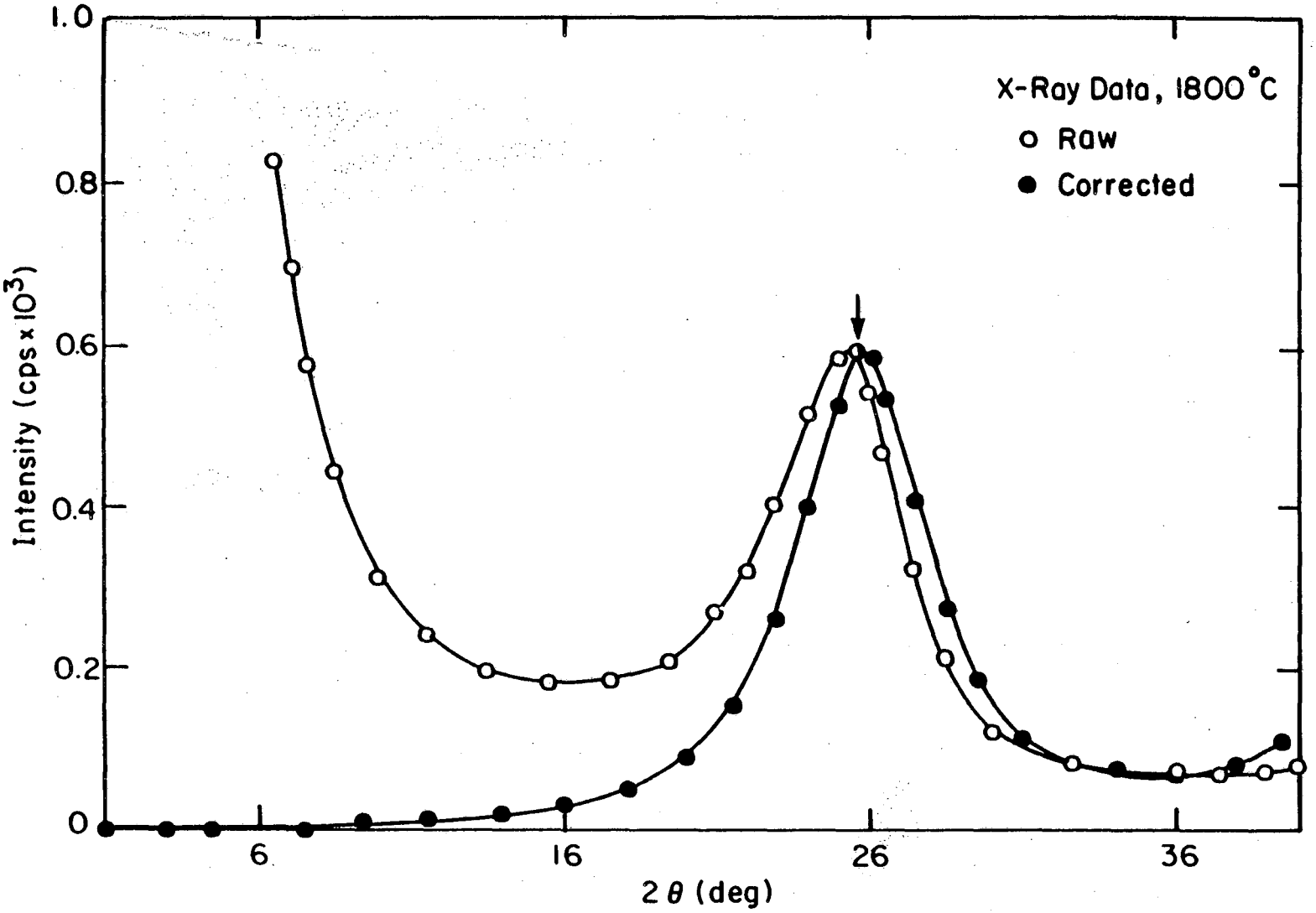

Fig. 4.1.F

XBL 8410-7440

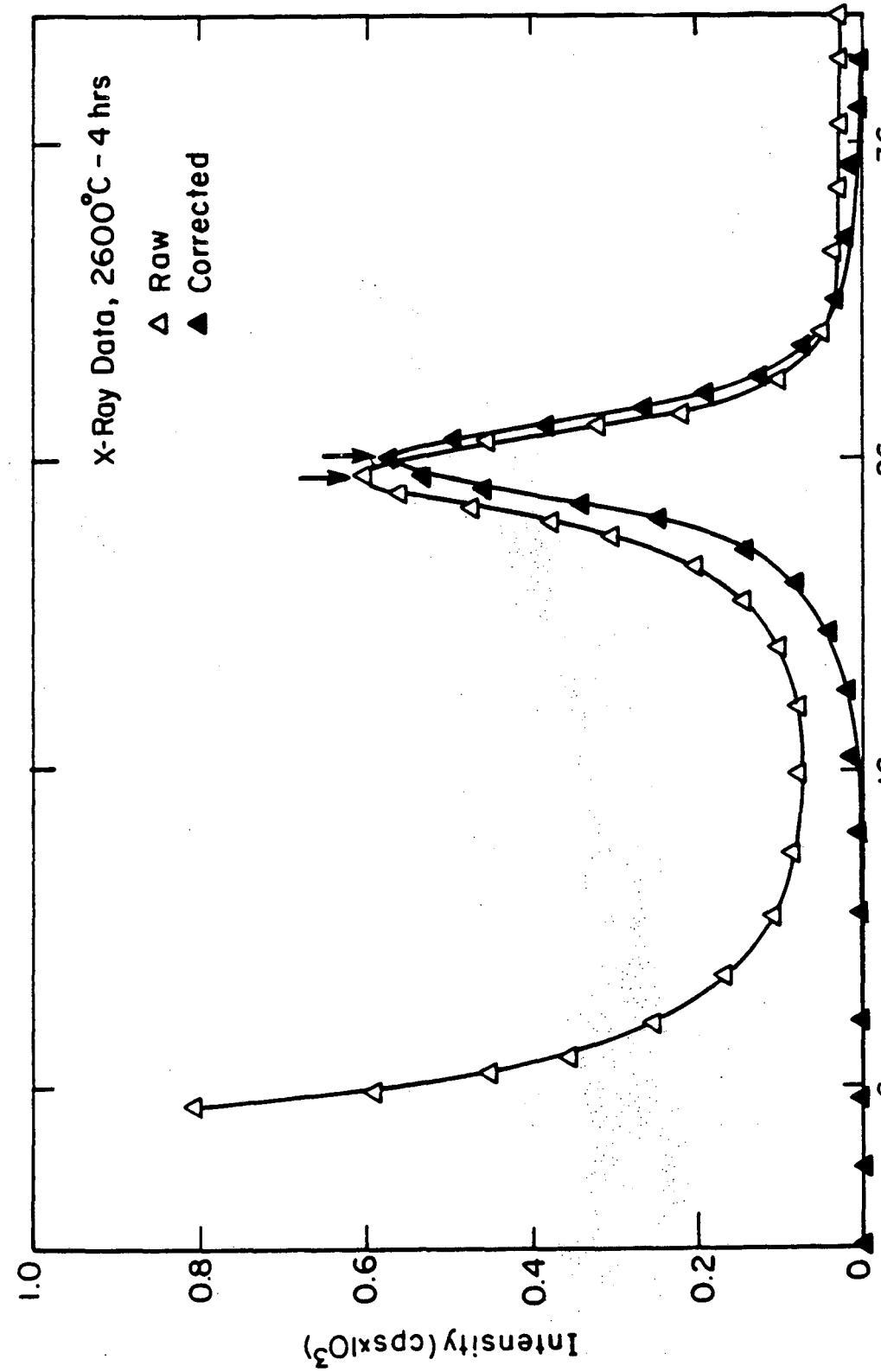
X-Ray Data, 2600°C - 4 hrs
Δ Raw
▲ Corrected
Intensity (cps x 10³)
1.0
0.8
0.6
0.4
0.2
0
6
16
26
36
2θ (deg)
XBL 8410-7441

Fig. 4.1.6

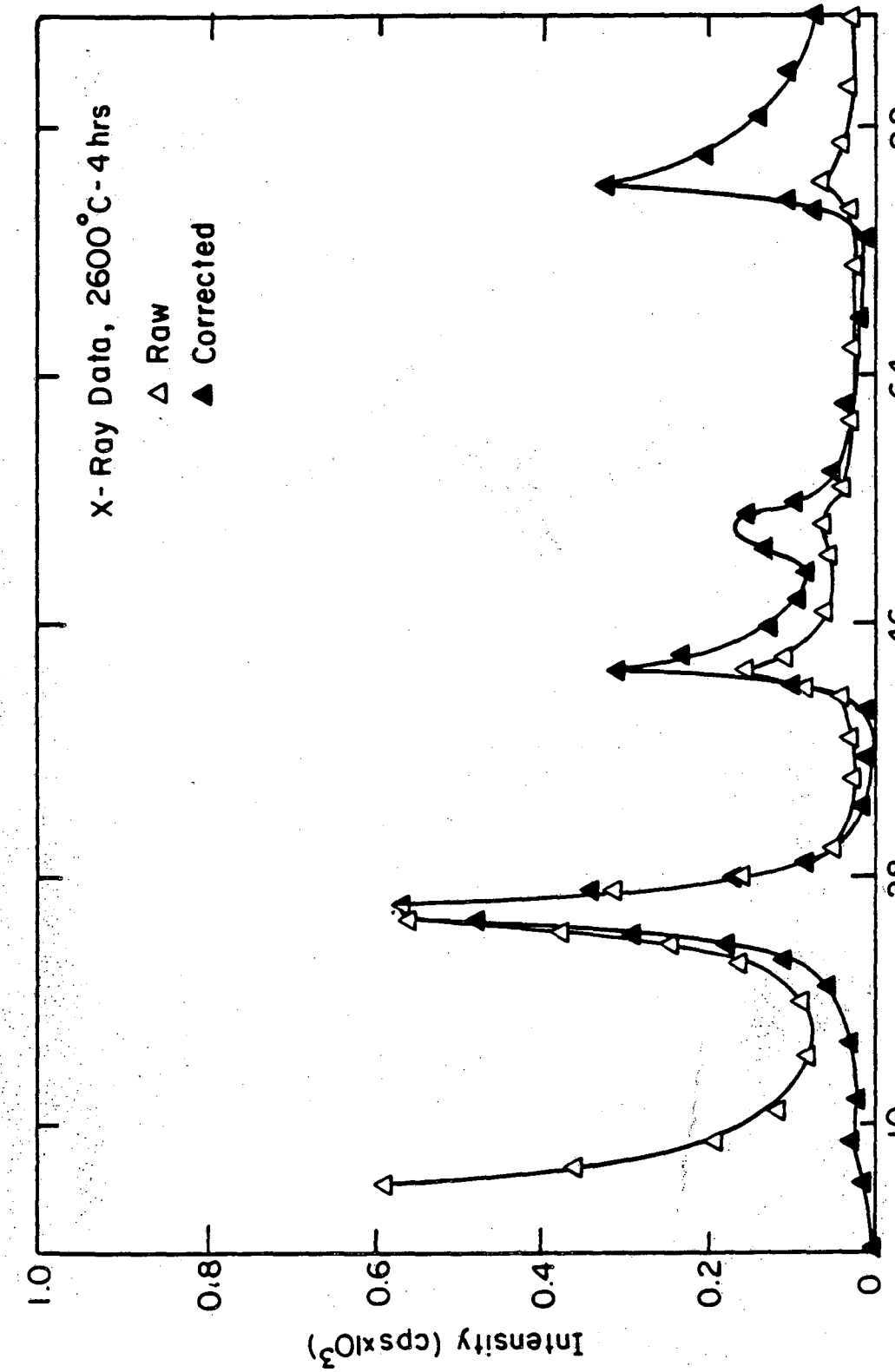
X-Ray Data, 2600°C-4 hrs
Δ Raw
▲ Corrected
Intensity (cps x10³)
0
0.2
0.4
0.6
0.8
1.0
10
28
46
64
82
2θ (deg)
XBL 8410-7442

Fig. 4.1.H

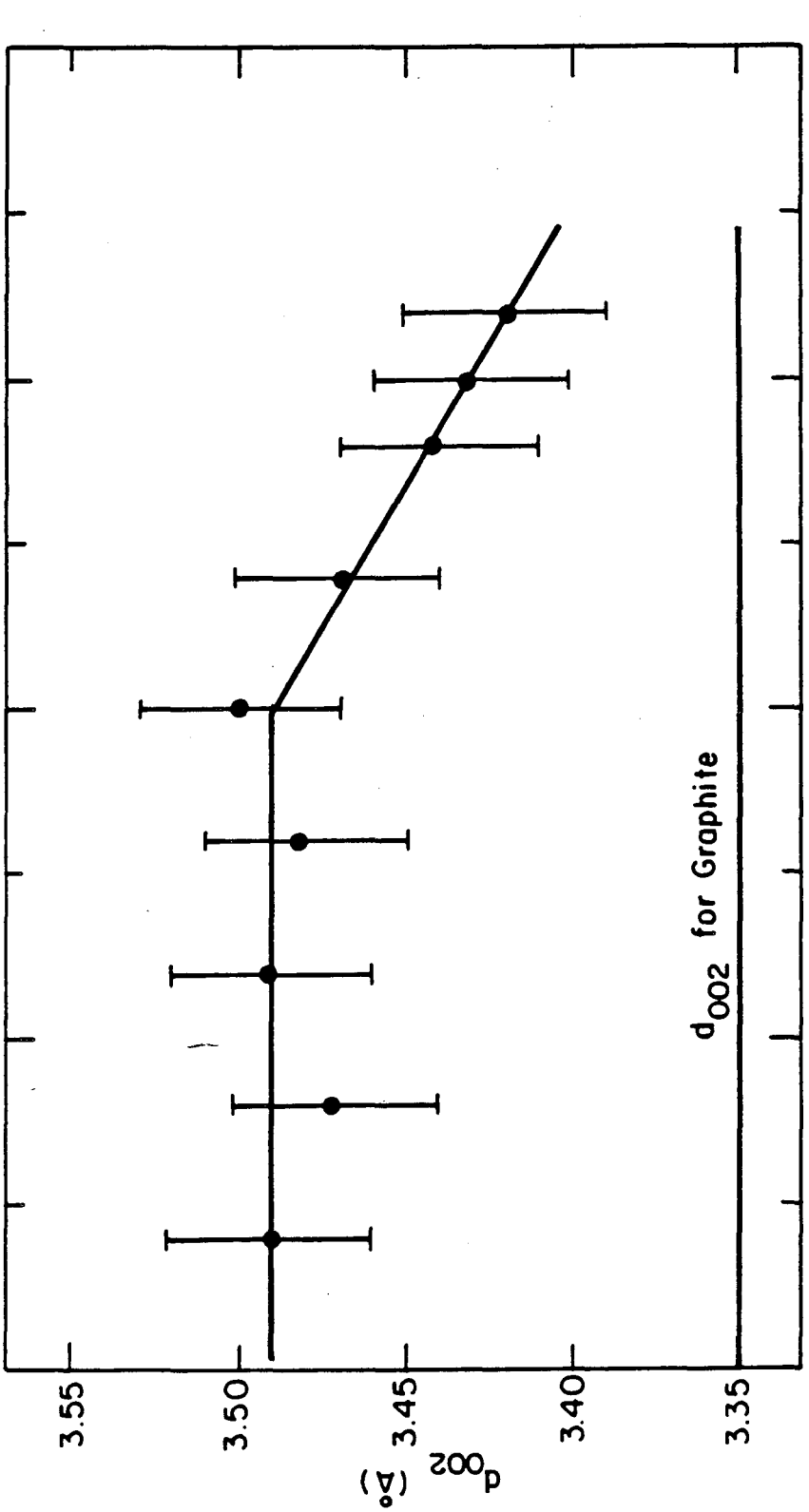

XBL8410-7443

Fig. 4.1.1

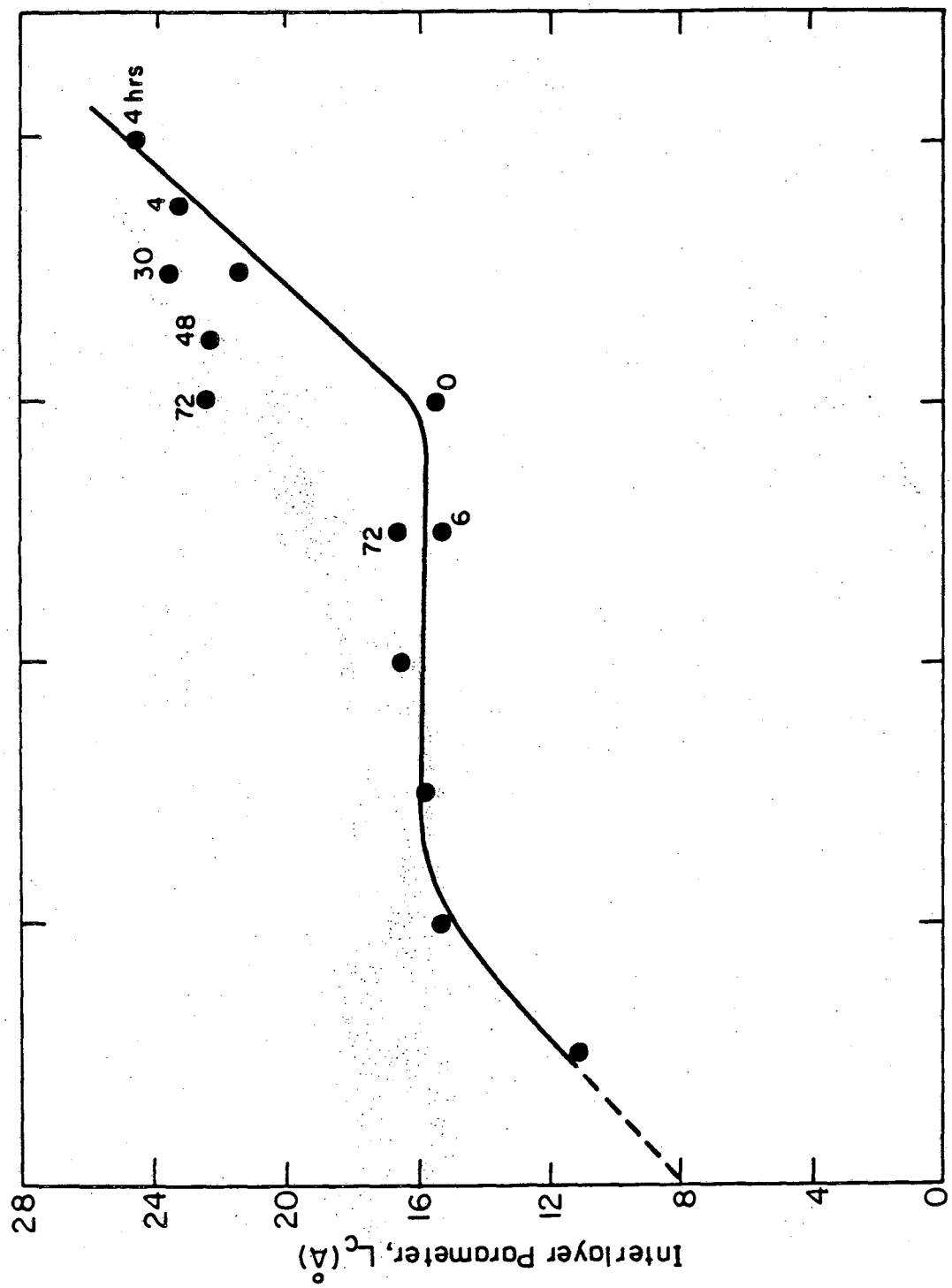
Interlayer Parameter, L_c (Å)
28
24
20
16
12
8
4
0
1000
1400
1800
2200
2600
HTT (°C)
4 hrs
4
30
48
72
0
72
6
XBL 8410-7444

Fig. 4.1.J

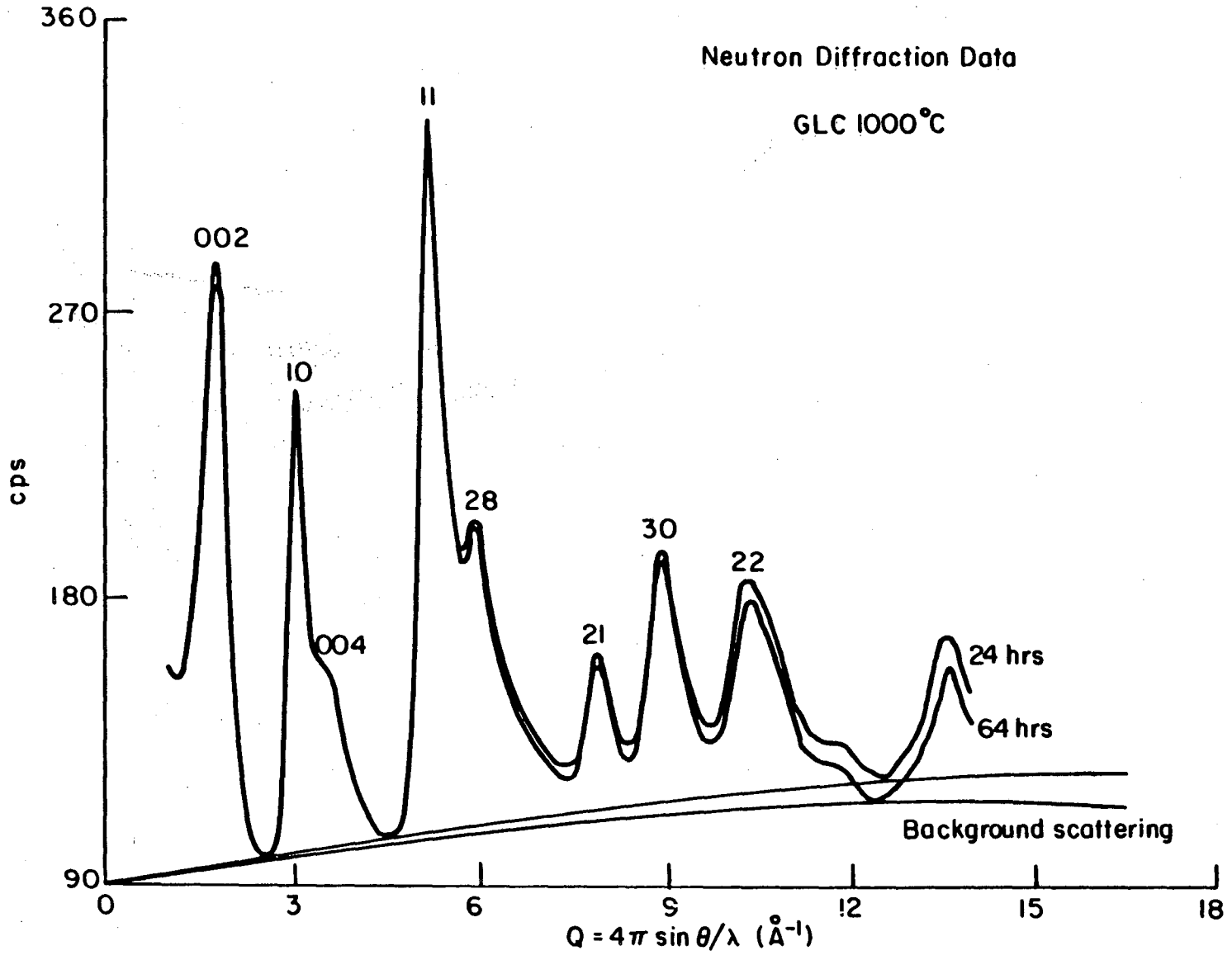

Fig. 4.1.K

XBL 8410-7445

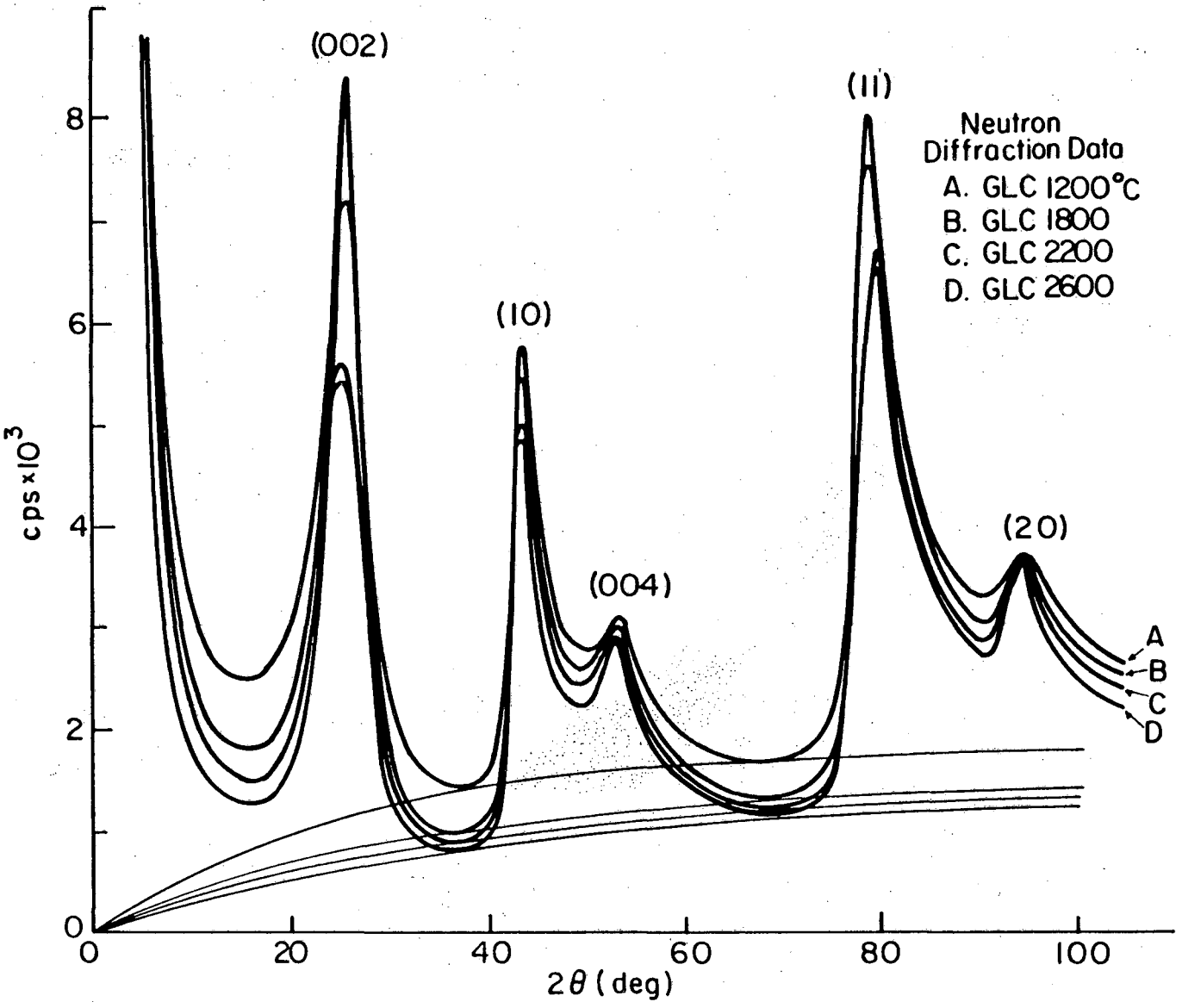
(002)
(11)
(10)
(004)
(20)
Neutron
Diffraction Data
A. GLC 1200°C
B. GLC 1800
C. GLC 2200
D. GLC 2600
A
B
C
D
cps x 10^3
0
2
4
6
8
0
20
40
60
80
100
2θ (deg)
XBL 8410-7446

Fig. 4.1.L

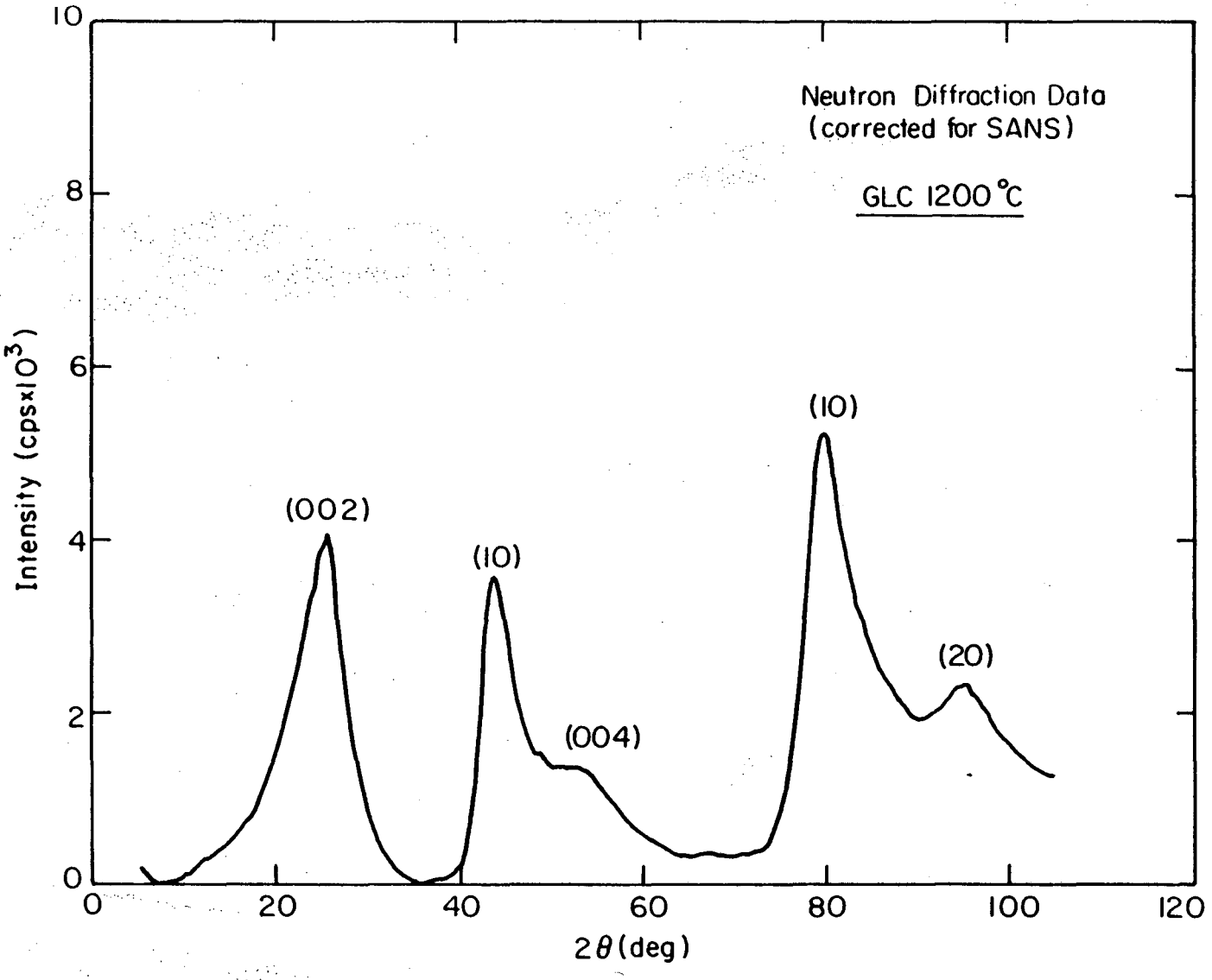

Fig. 4.1.M

XBL 8410-7447

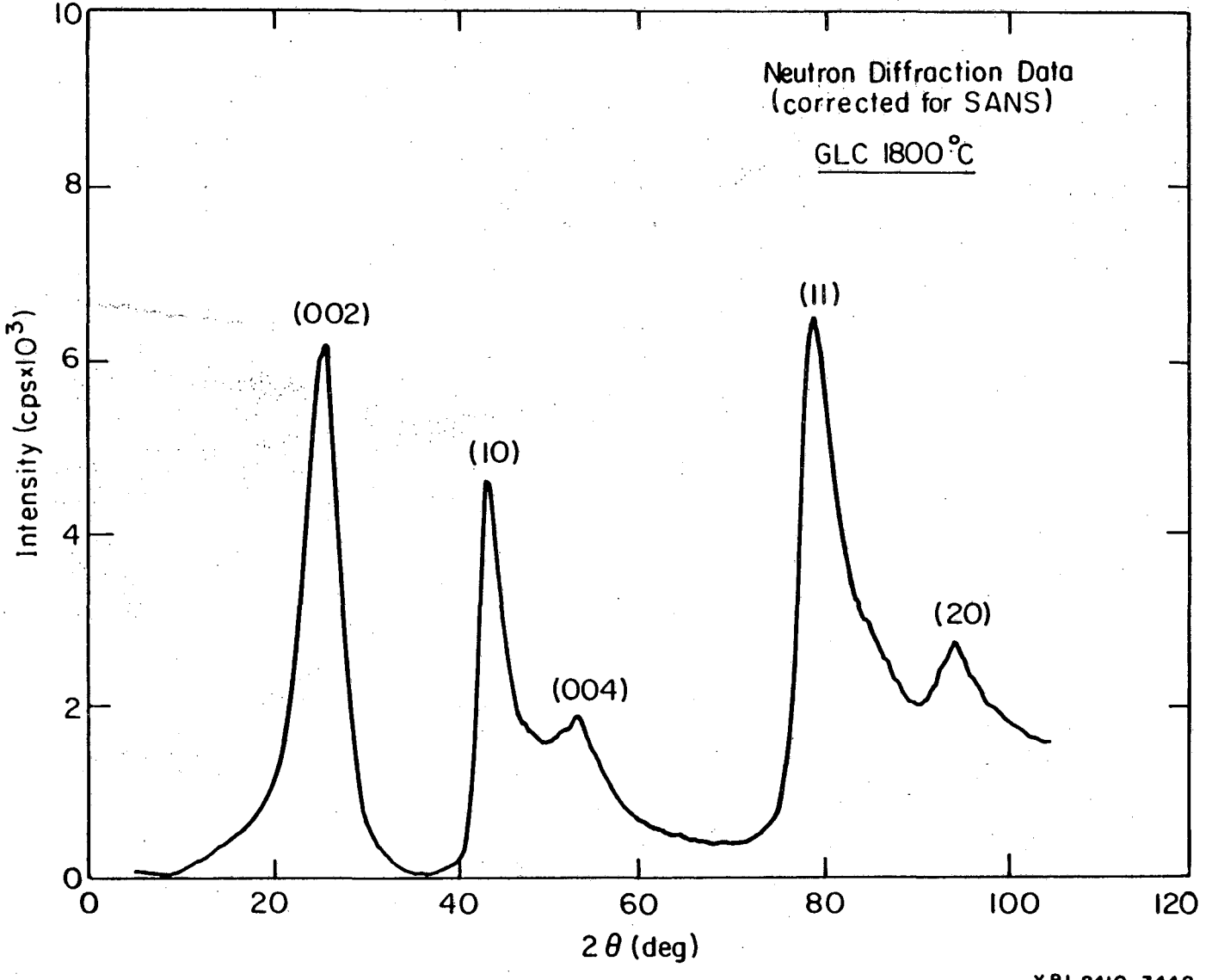

XBL8410-7448

Fig. 4.1.N

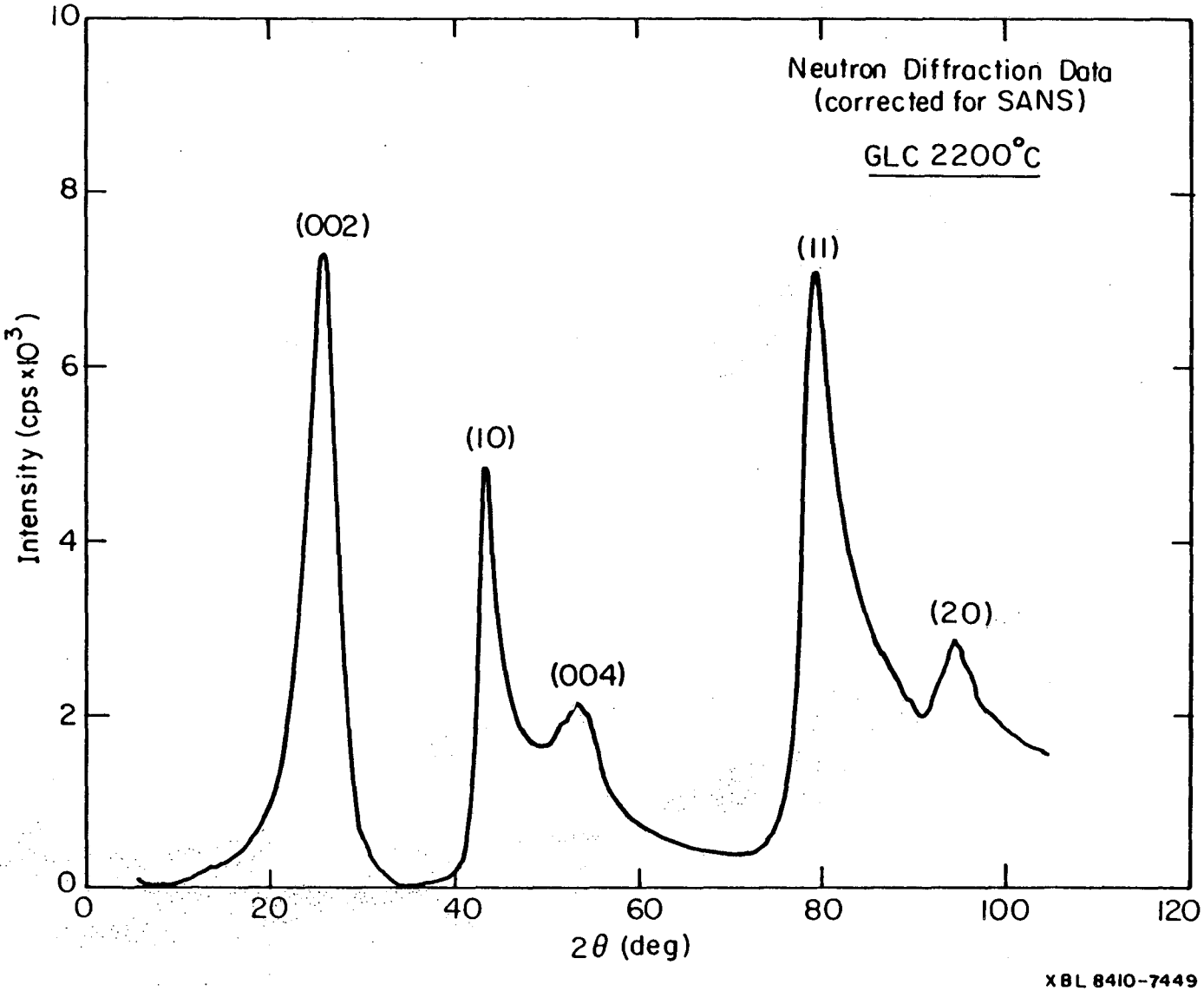
Neutron Diffraction Data
(corrected for SANS)
GLC 2200°C
(002)
(10)
(004)
(11)
(20)
Intensity (cps x10^3)
2θ (deg)
0
2
4
6
8
10
0
20
40
60
80
100
120
XBL 8410-7449

Fig. 4.1.0

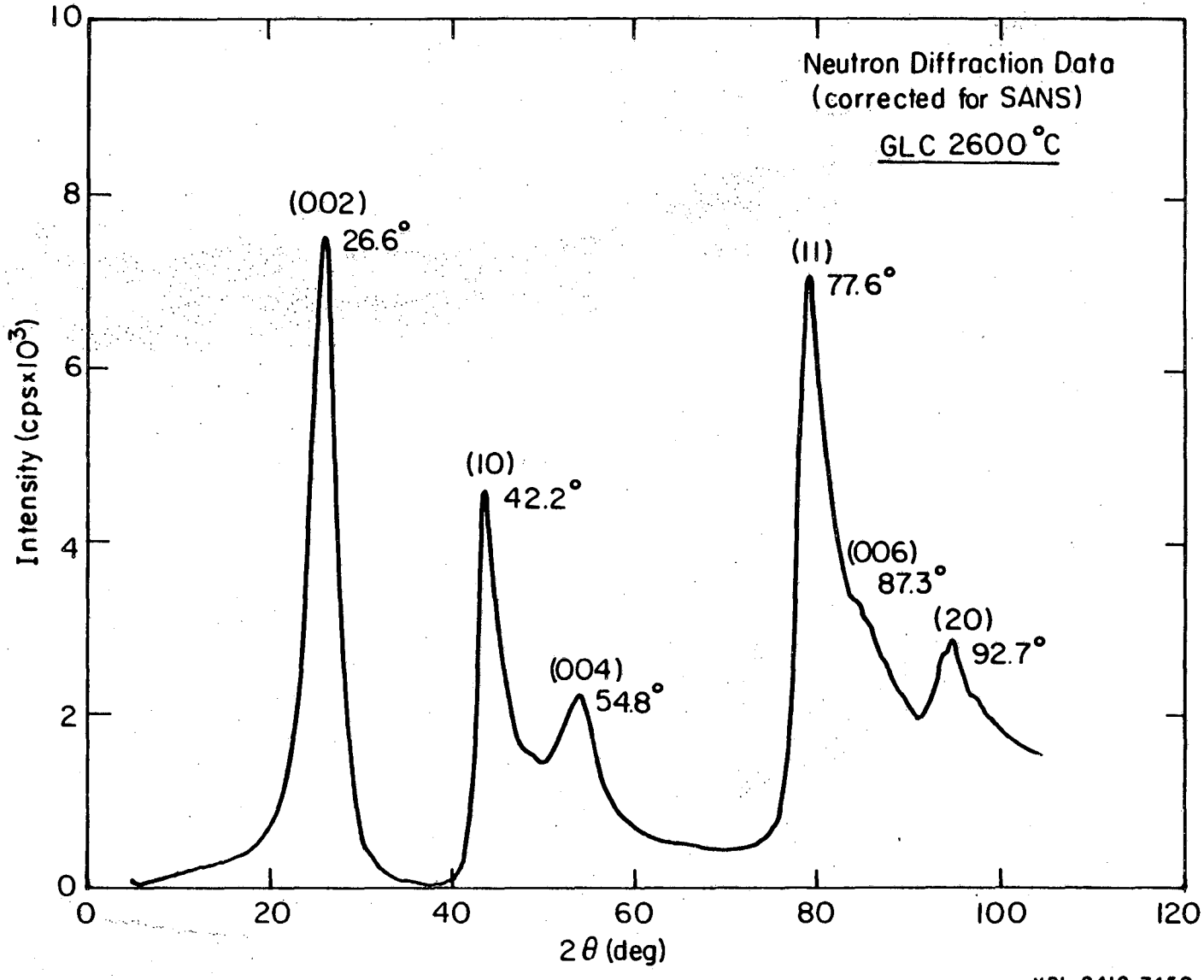

Fig. 4.1.P

XBL 8410-7450

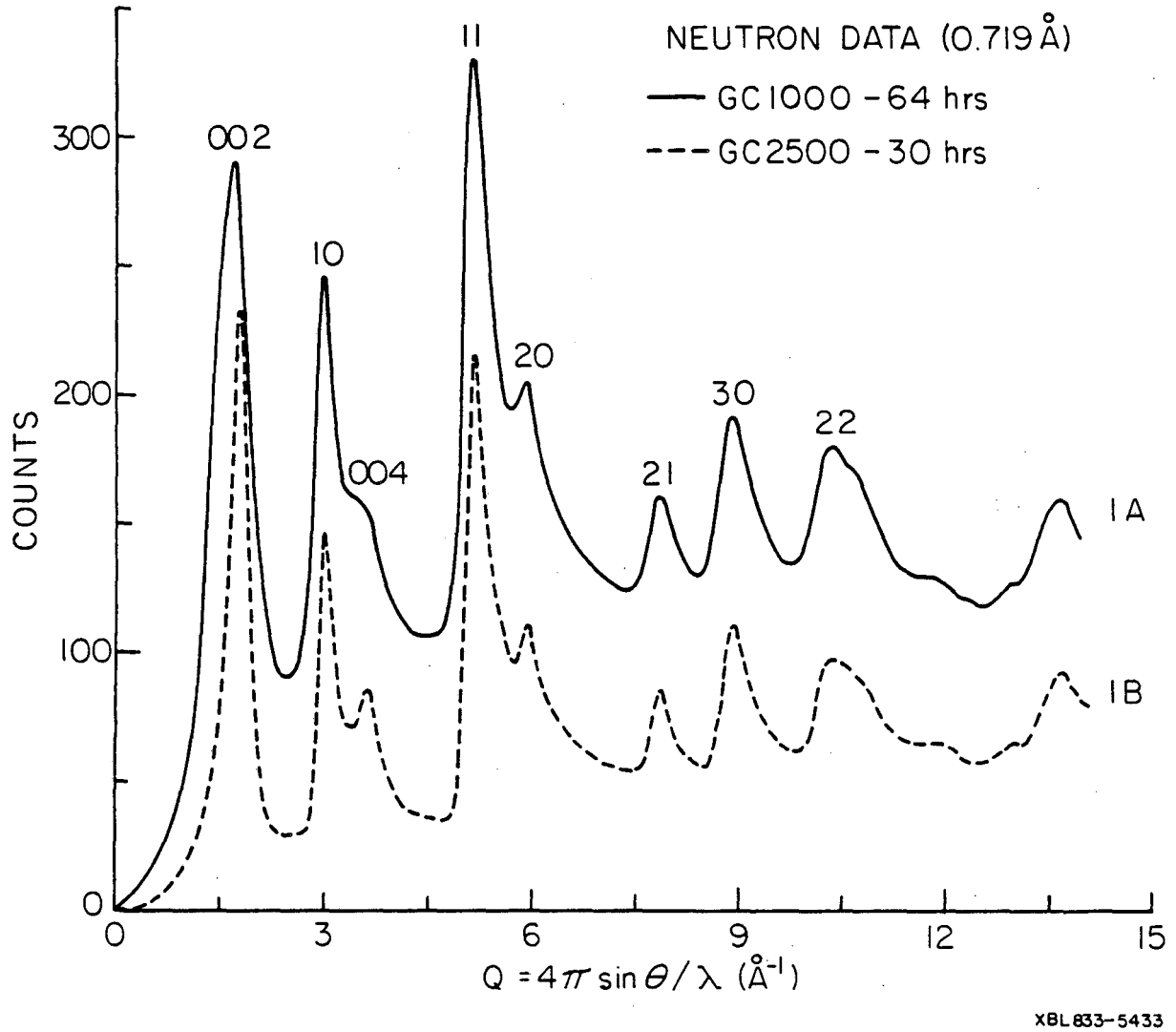
NEUTRON DATA (0.719 Å)
GC1000 - 64 hrs
GC2500 - 30 hrs
002
10
004
11
20
21
30
22
1A
1B
COUNTS
300
200
100
0
0
3
6
9
12
15
Q = 4π sin θ/λ (Å⁻¹)
XBL833-5433

Fig. 4.1.Q

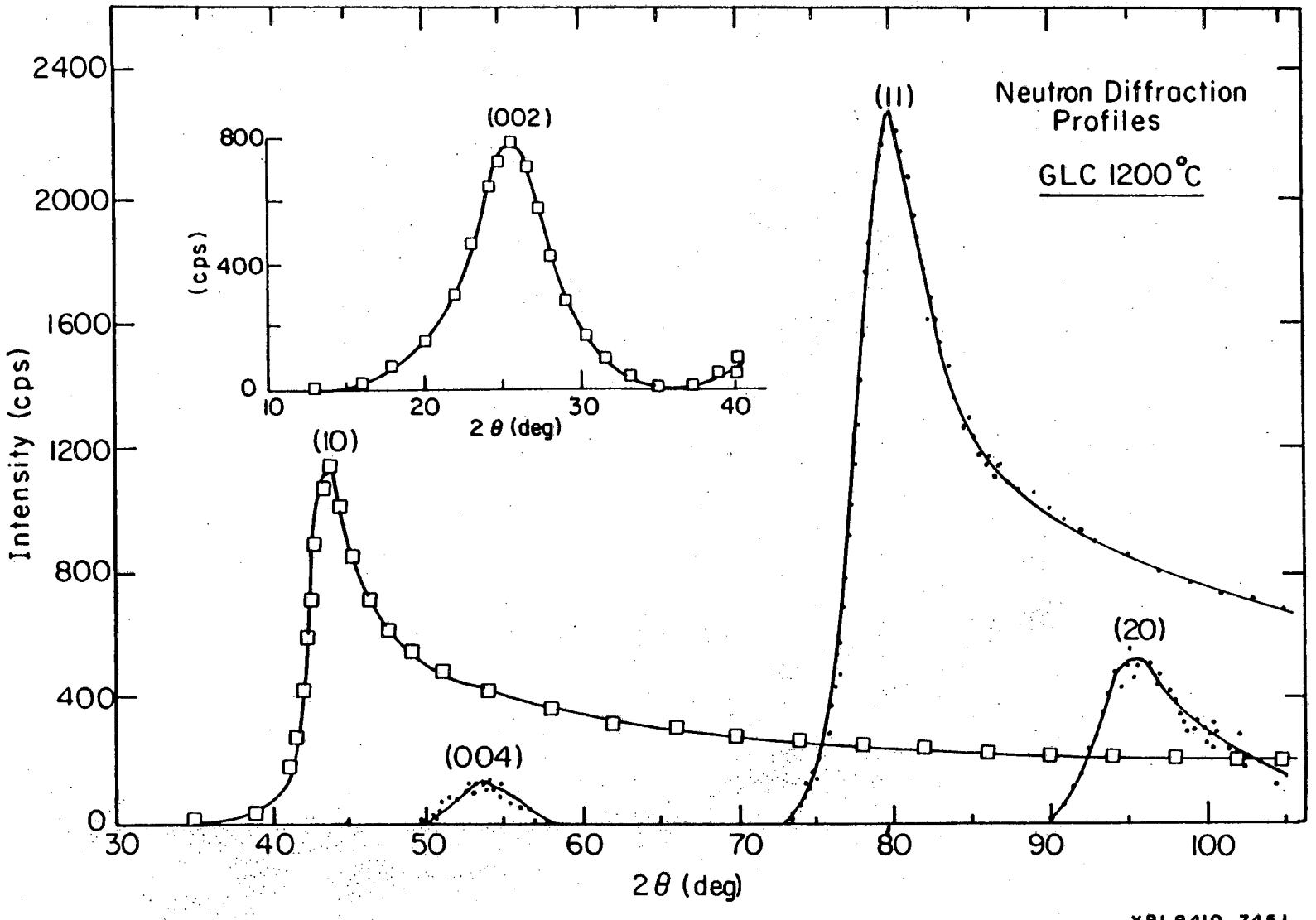
Neutron Diffraction Profiles
GLC 1200°C
(002)
(11)
(10)
(004)
(20)
Intensity (cps)
2θ (deg)
(cps)
2 θ (deg)
XBL8410-7451

Fig. 4.1.R

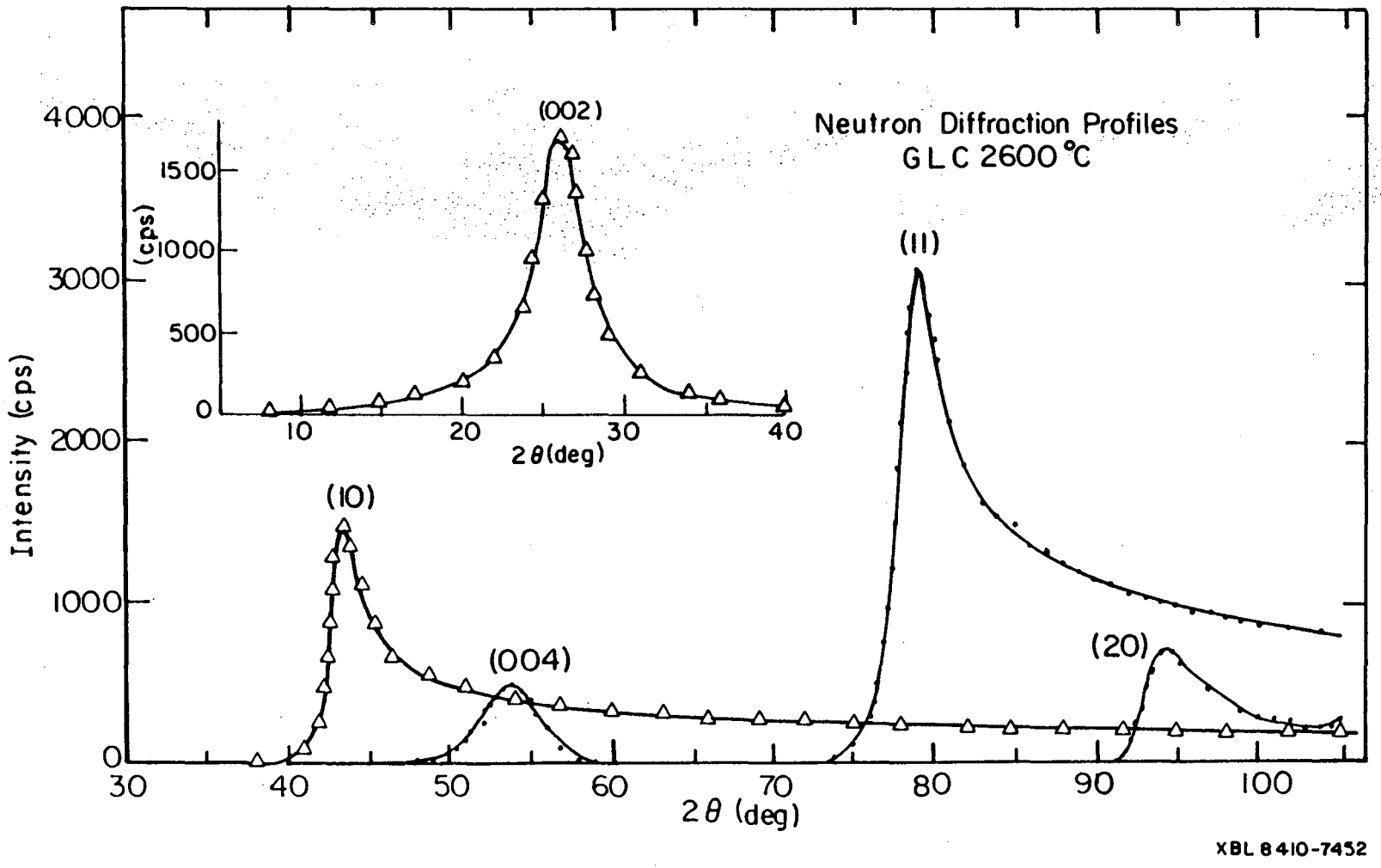
Neutron Diffraction Profiles
GLC 2600 °C
(002)
(11)
(10)
(004)
(20)
Intensity (cps)
2θ (deg)
(cps)
2θ(deg)
XBL 8410-7452

Fig. 4.1.S

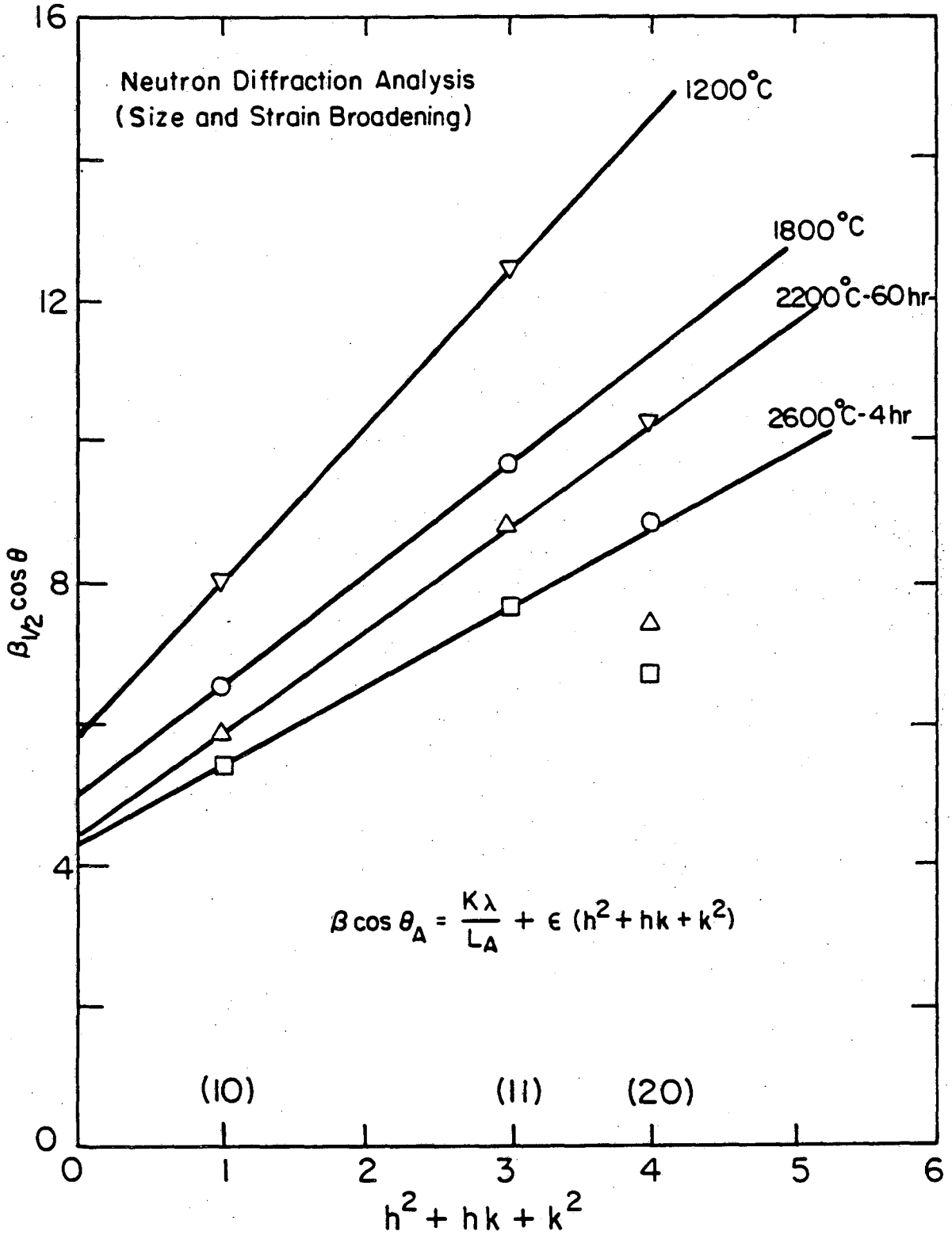

Fig. 4.1.T

XBL 8410-7453

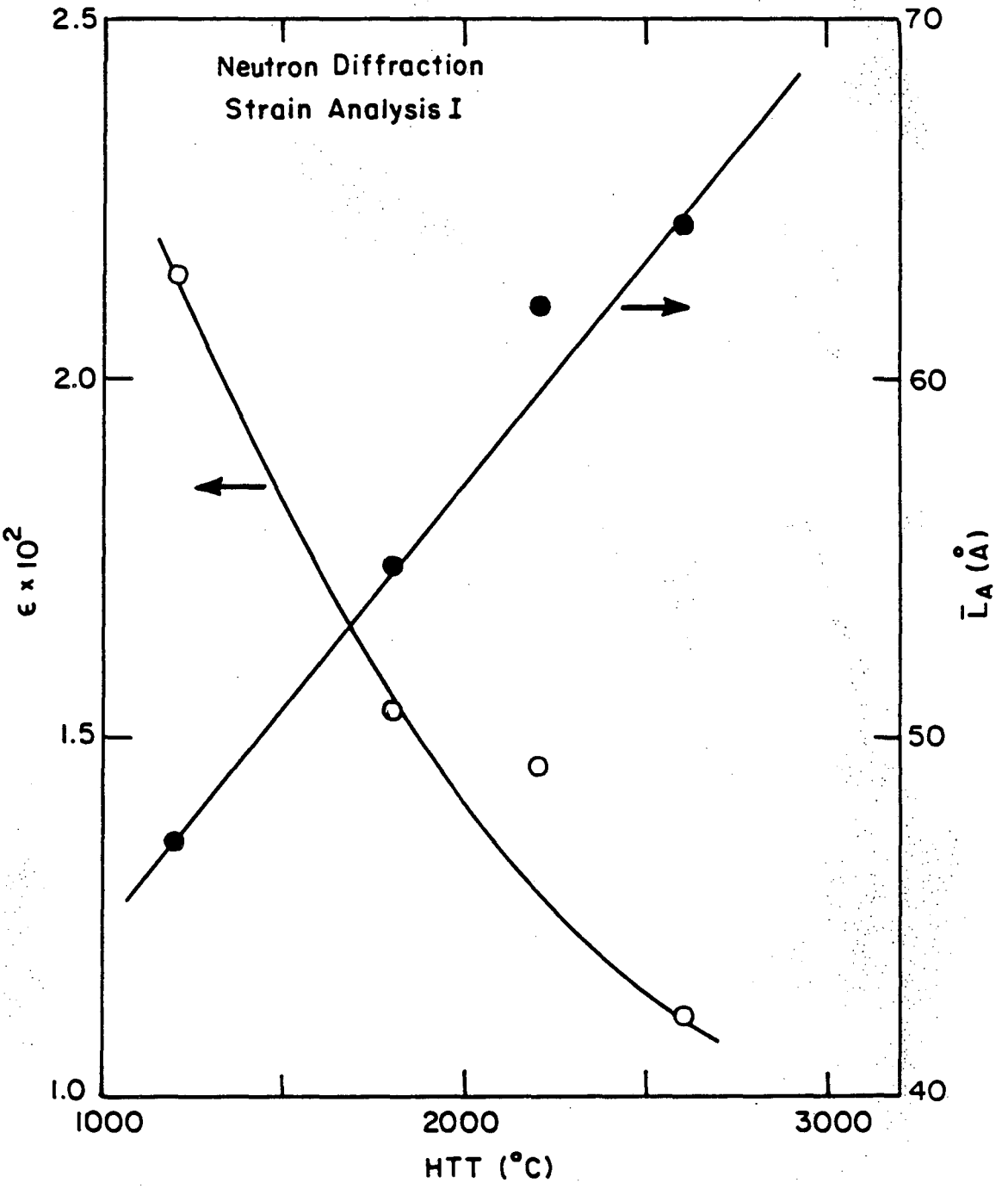

Fig. 4.1.U

XBL 8410-8249

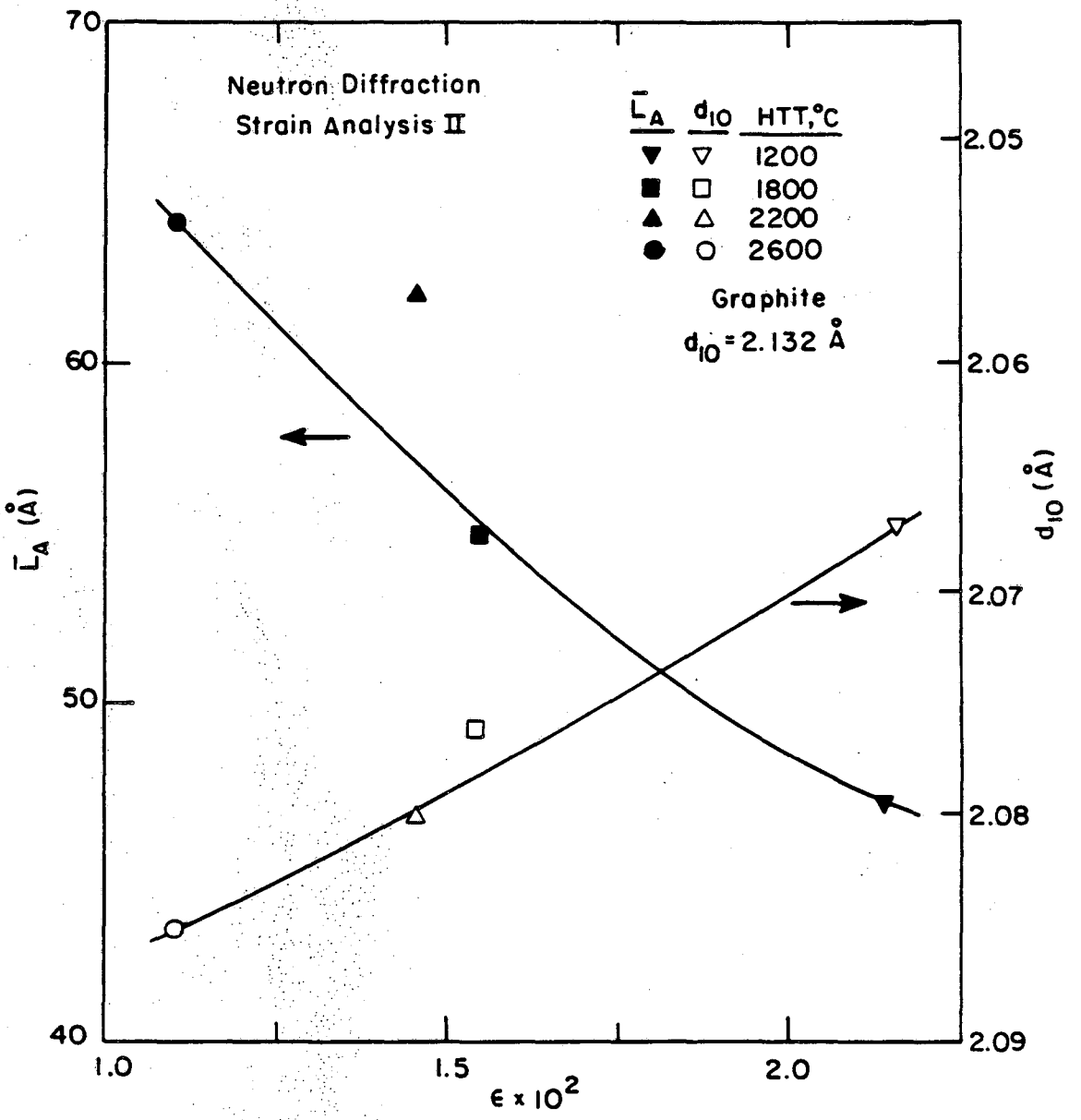
Neutron Diffraction
Strain Analysis II
$\bar{L}_A$ d_{10} HTT,°C
1200
1800
2200
2600
Graphite
d_{10} = 2.132 Å
$\bar{L}_A$ (Å)
d_{10} (Å)
70
60
50
40
2.05
2.06
2.07
2.08
2.09
1.0
1.5
2.0
$\epsilon \times 10^2$
XBL 8410-8250

Fig. 4.1.V

SAXS Data

Isointensity Contour Map

GLC 2600°C

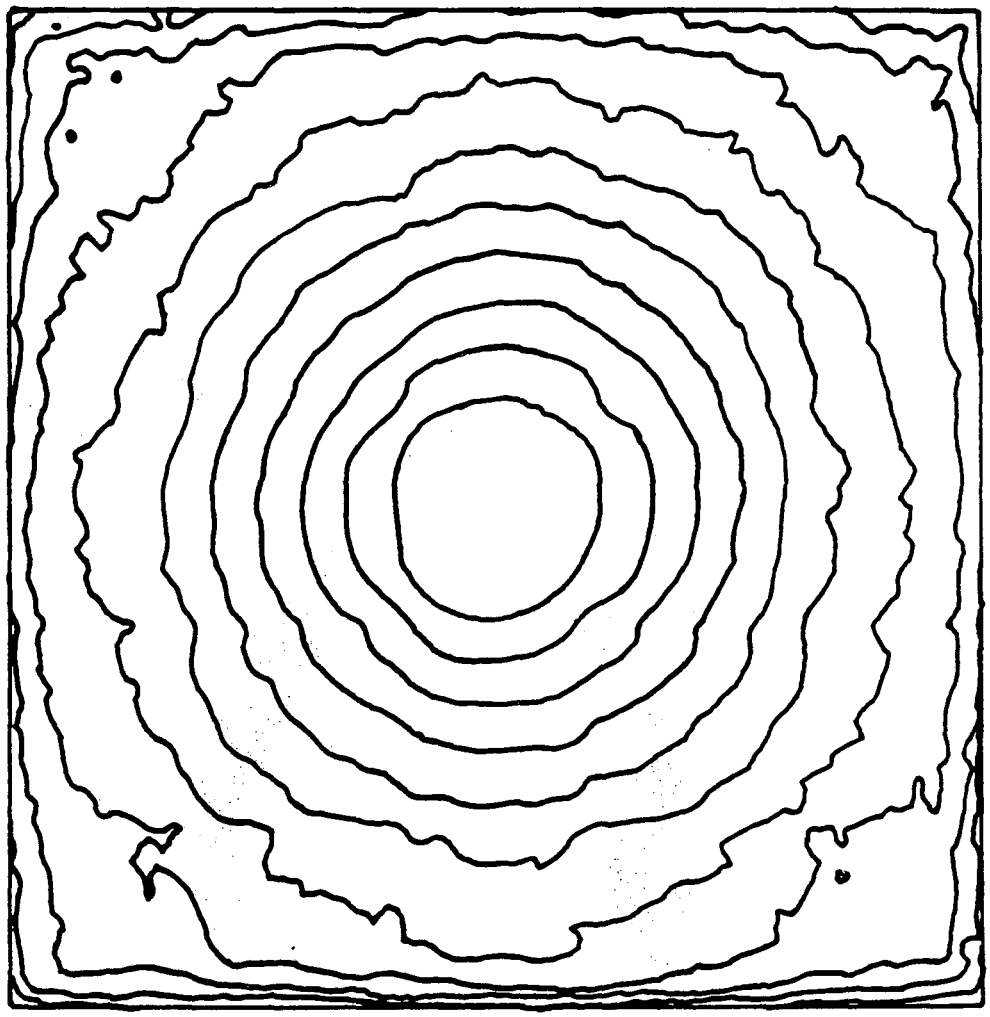

XBL 8410-7454

Fig. 4.4.A

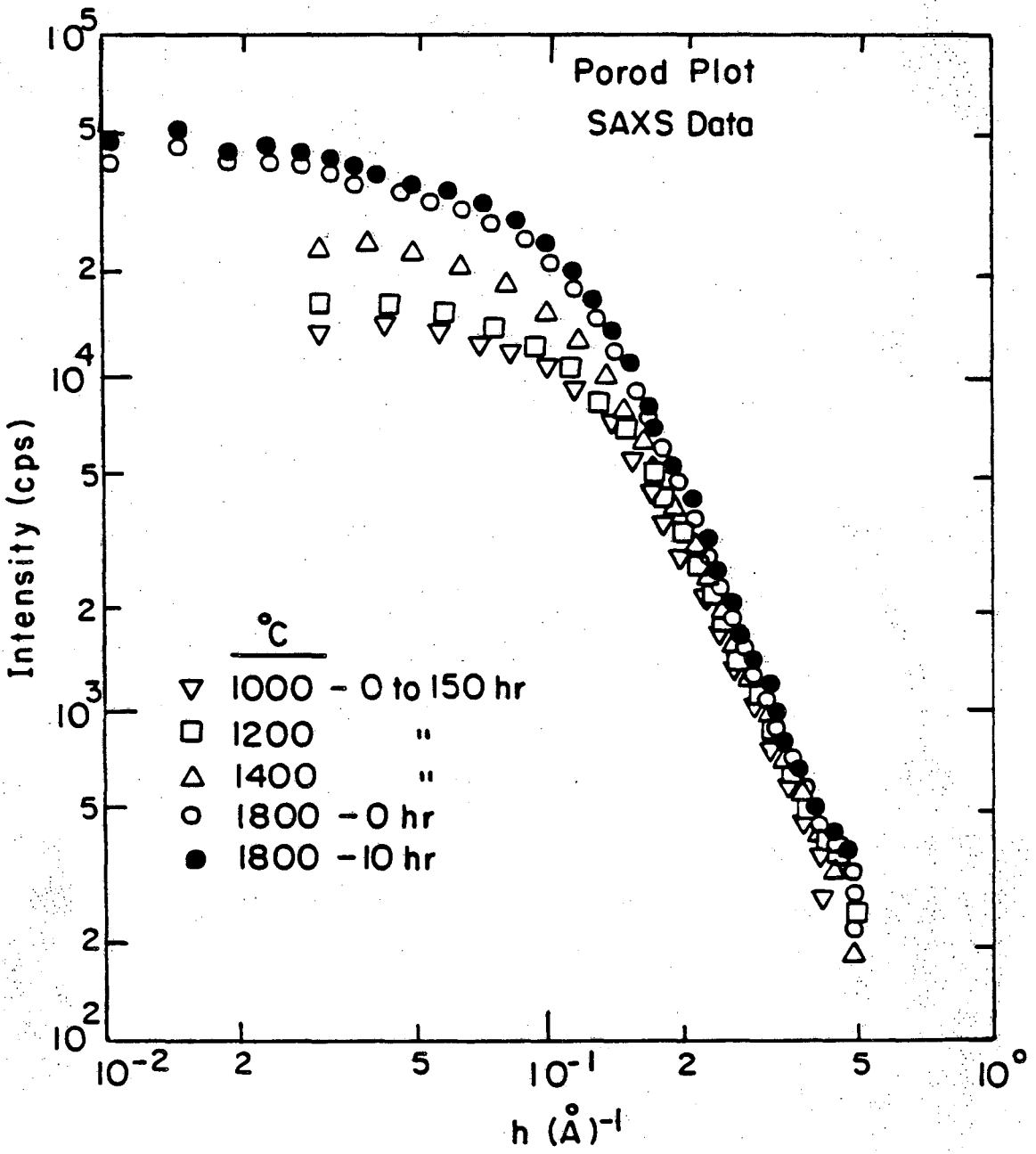

Fig. 4.4.B XBL 8410-7455

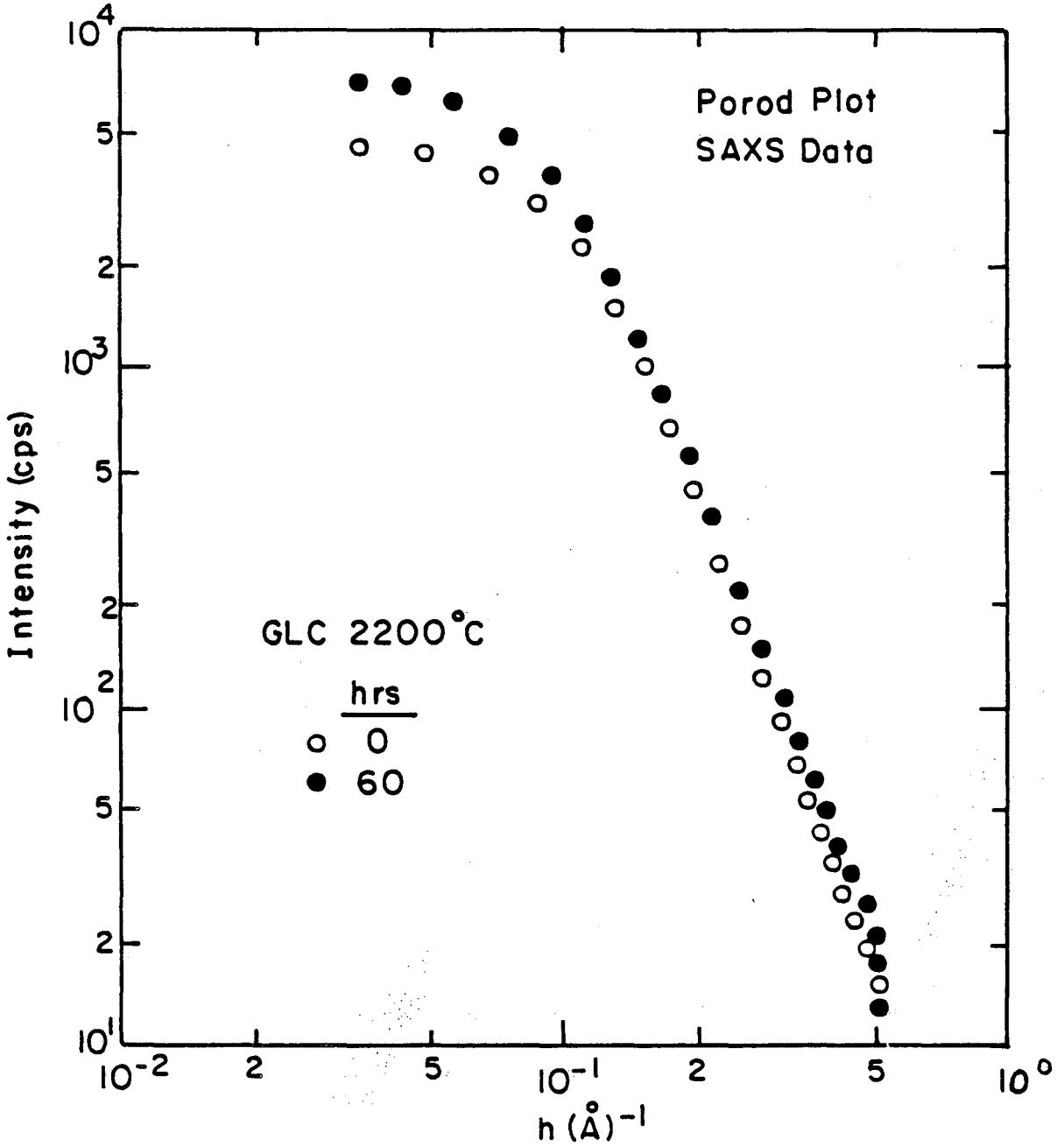

Fig. 4.4.C

XBL 8410-7456

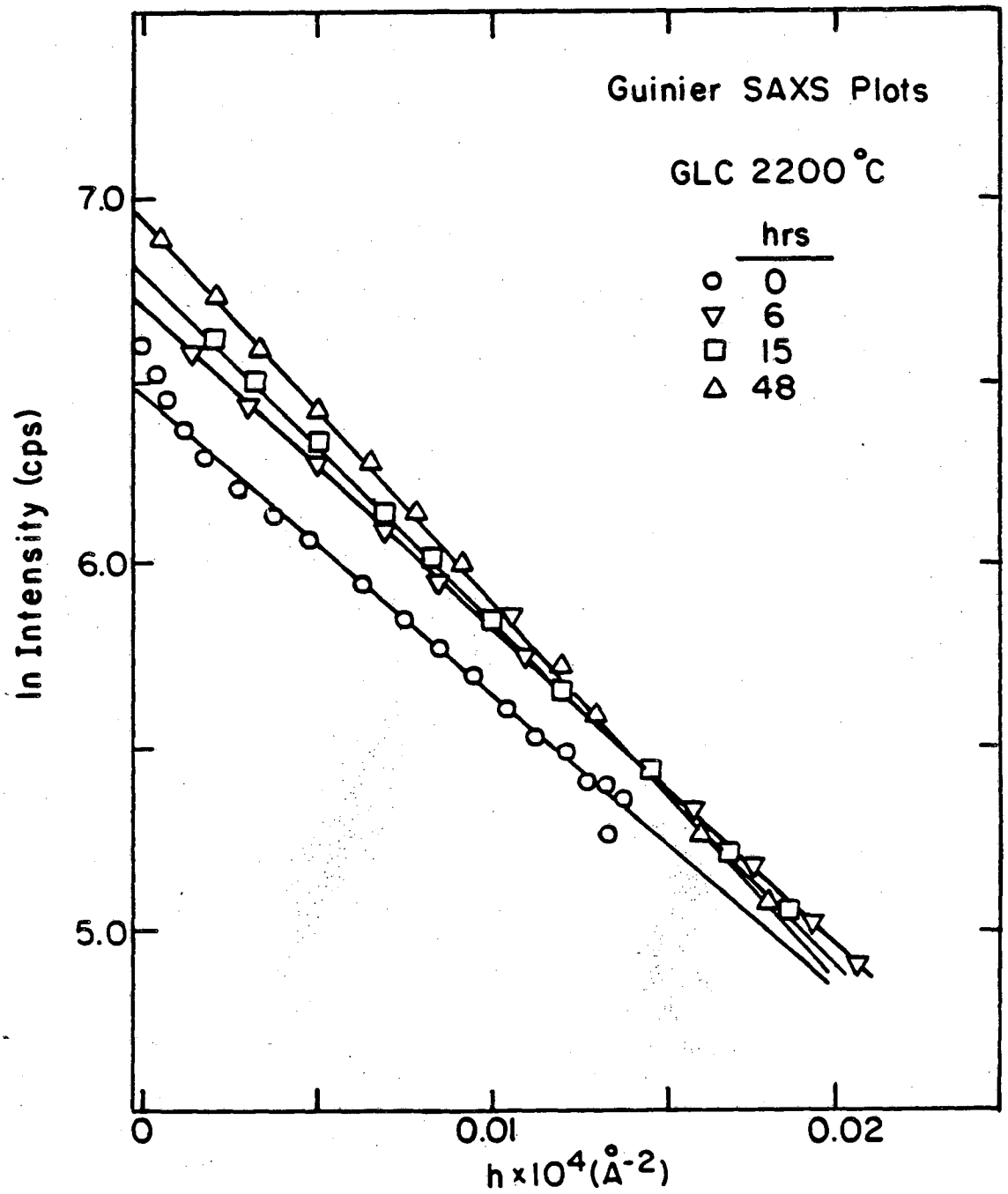

Fig. 4.4.D

XBL 8410-7457

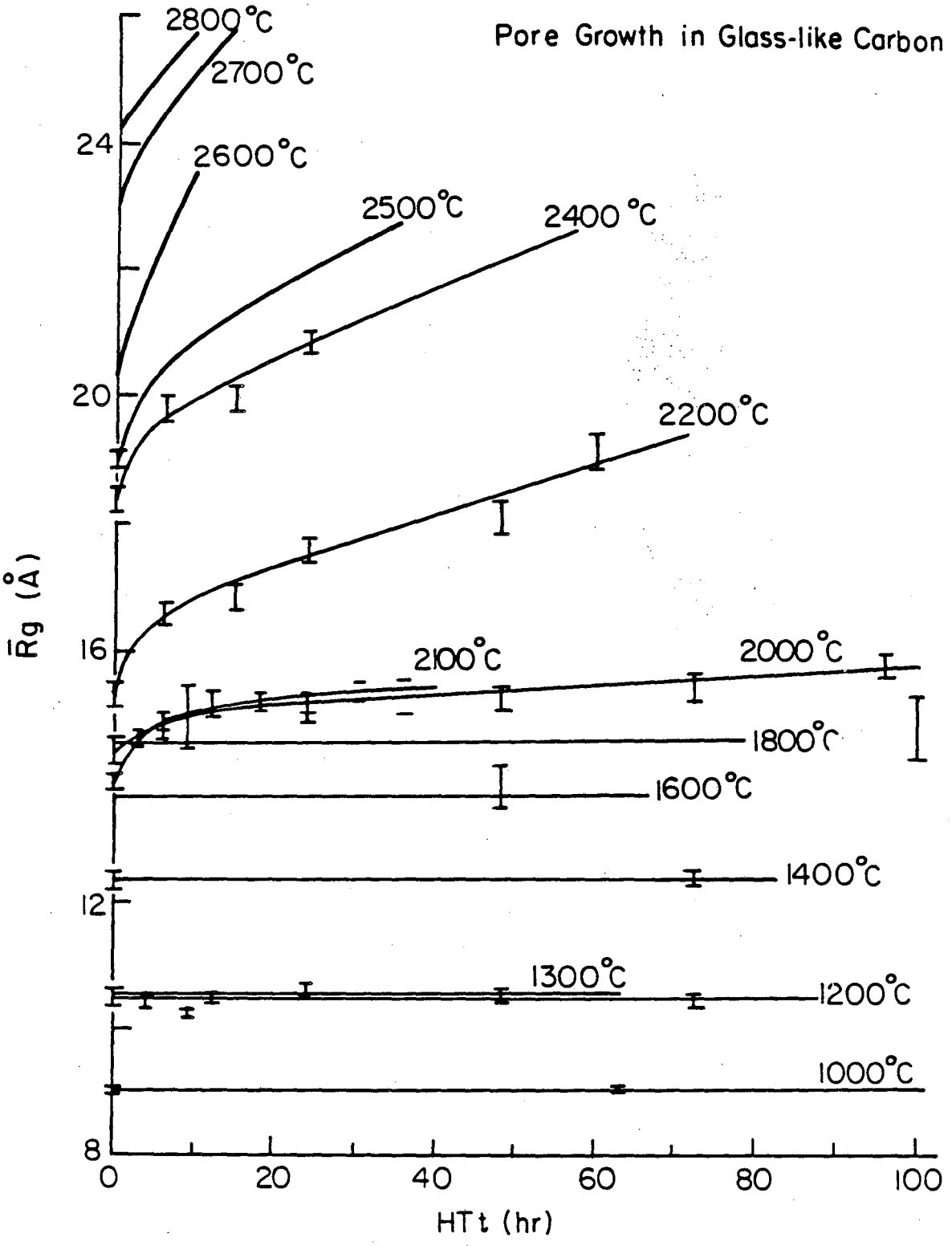

Fig. 4.4.E

XBL8410-7458

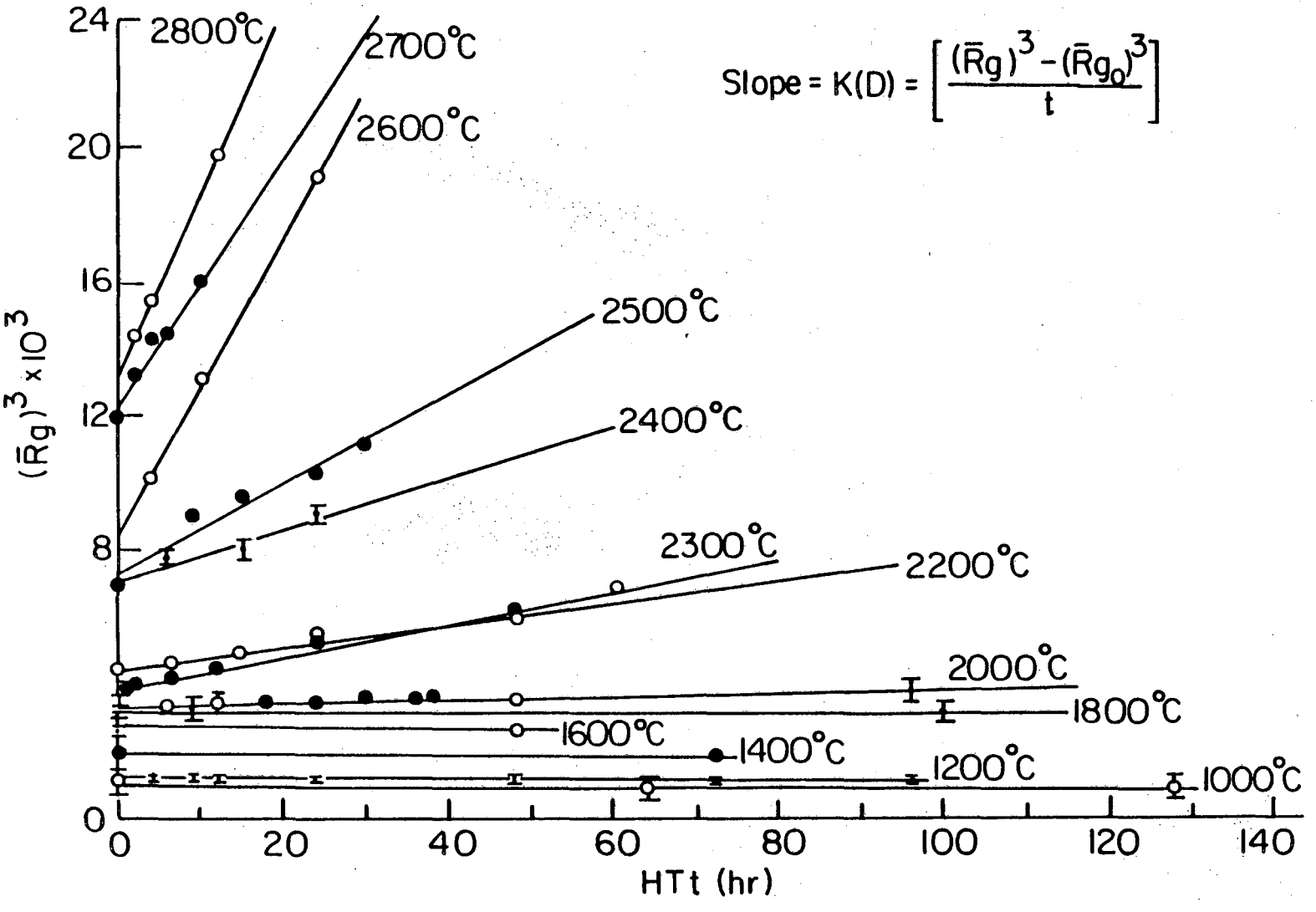

Fig. 4.4.F

XBL 8410-7459

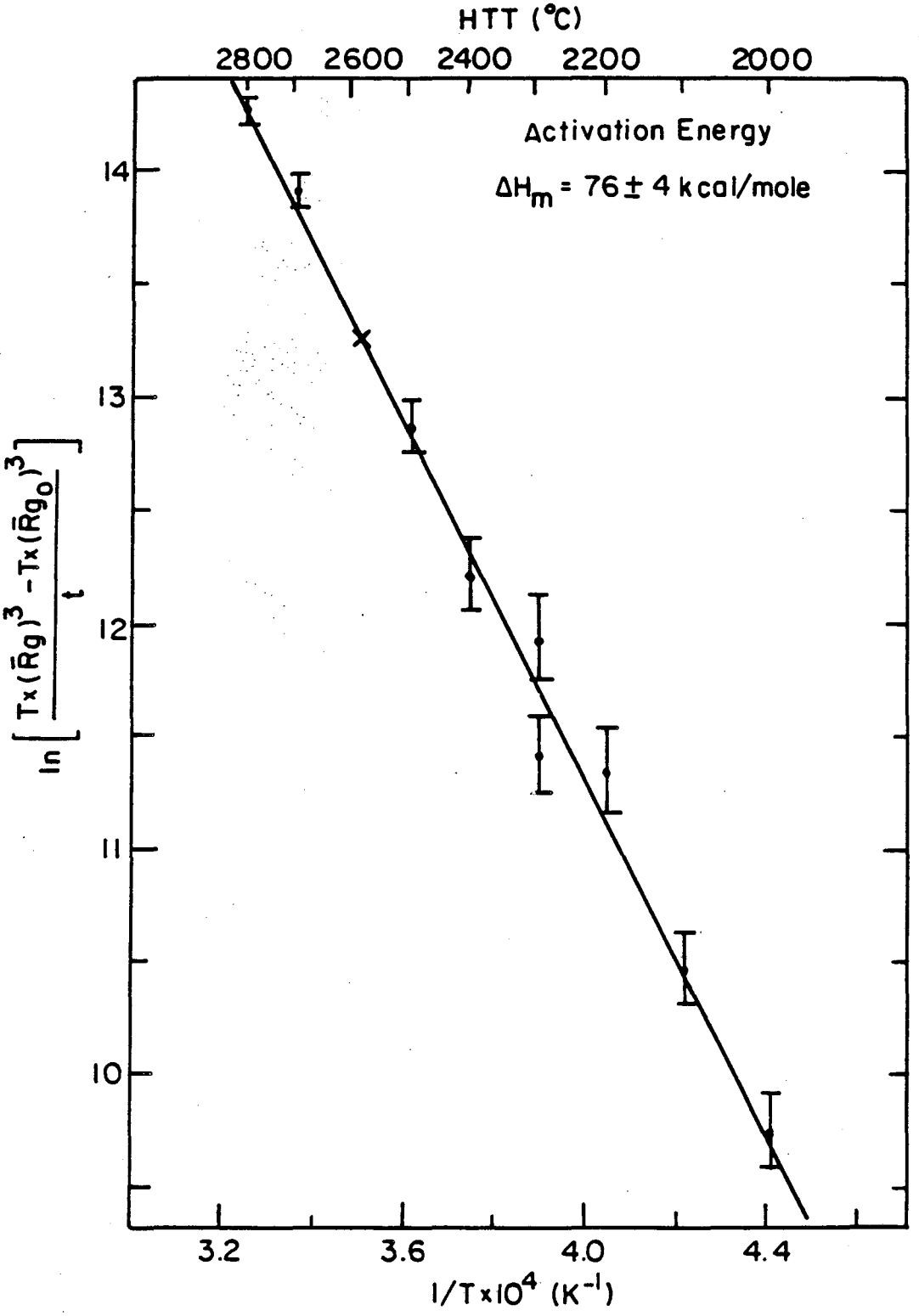

Fig. 4.4.G

XBL 8410-7460

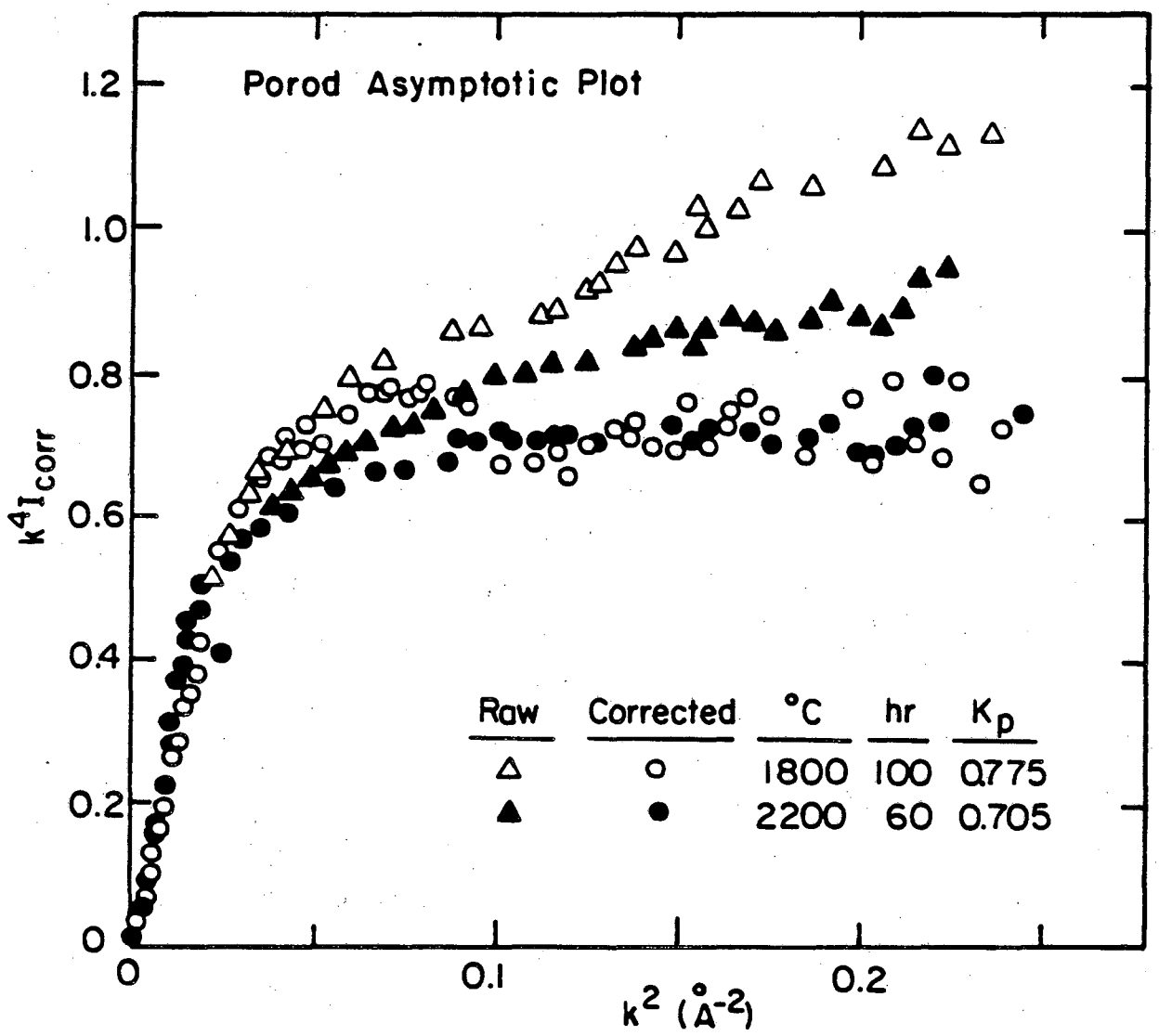

Fig. 4.4.H

XBL 8410-7461

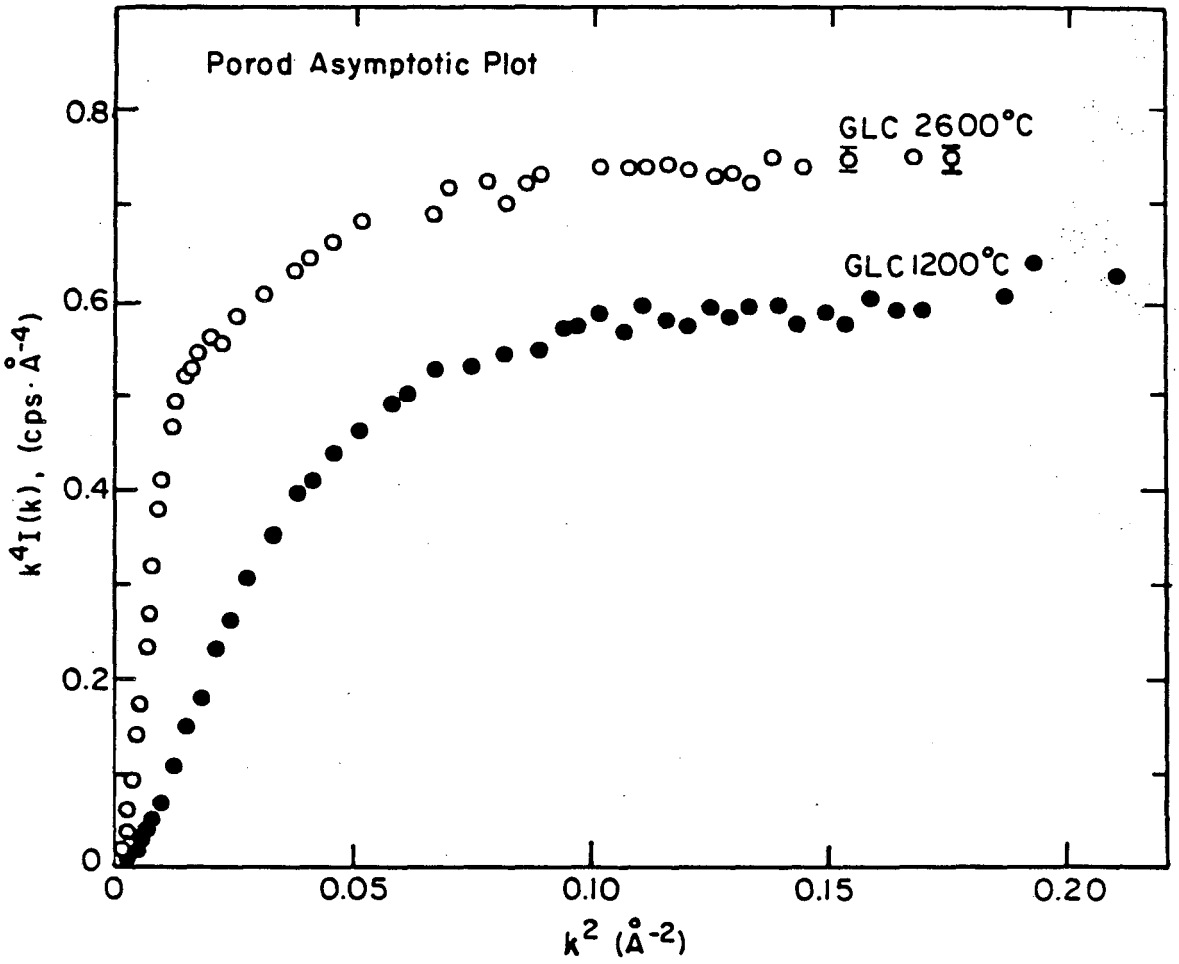

Fig. 4.4.I

XBL 8410-7462

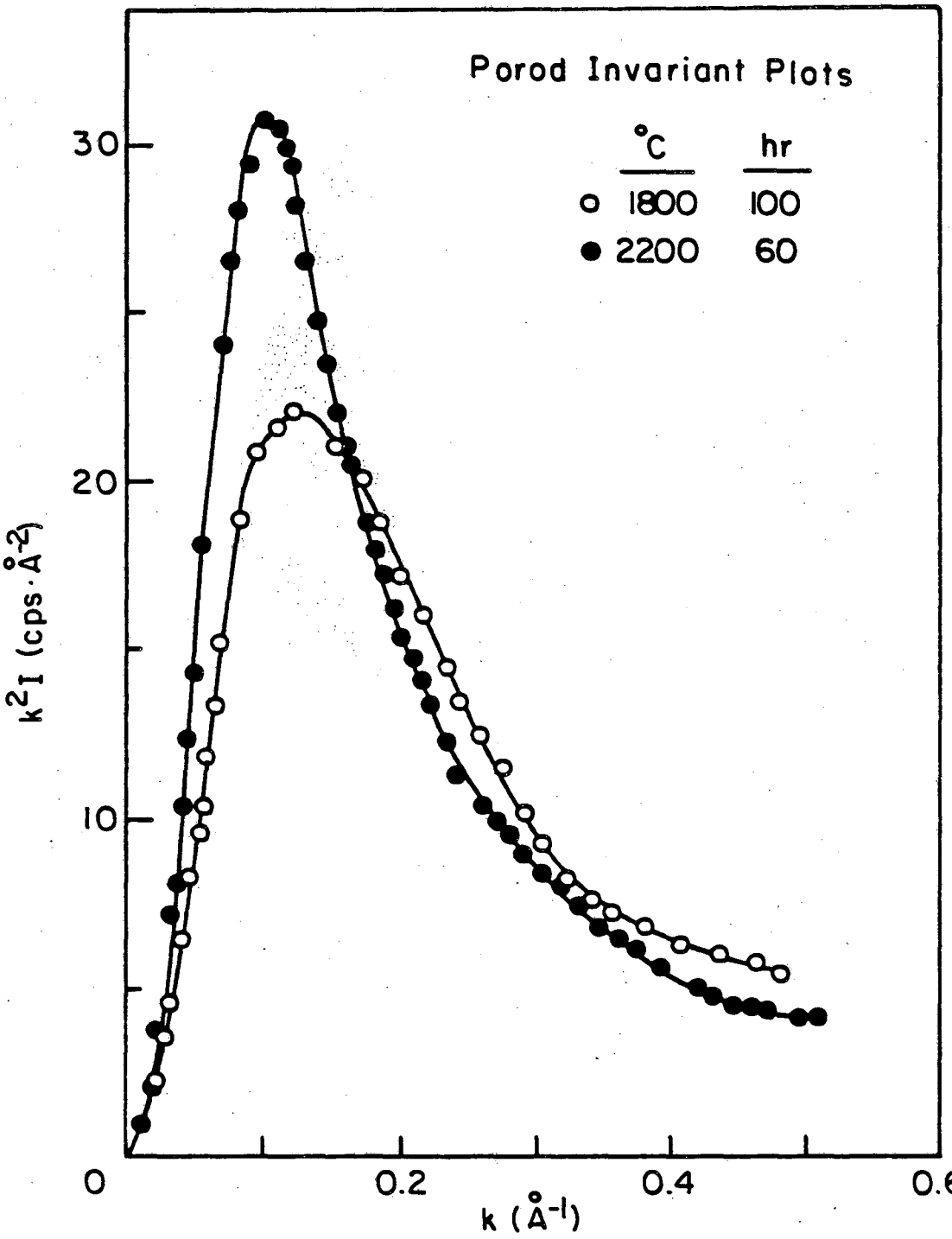

Fig. 4.4.J

XBL 8410-7463

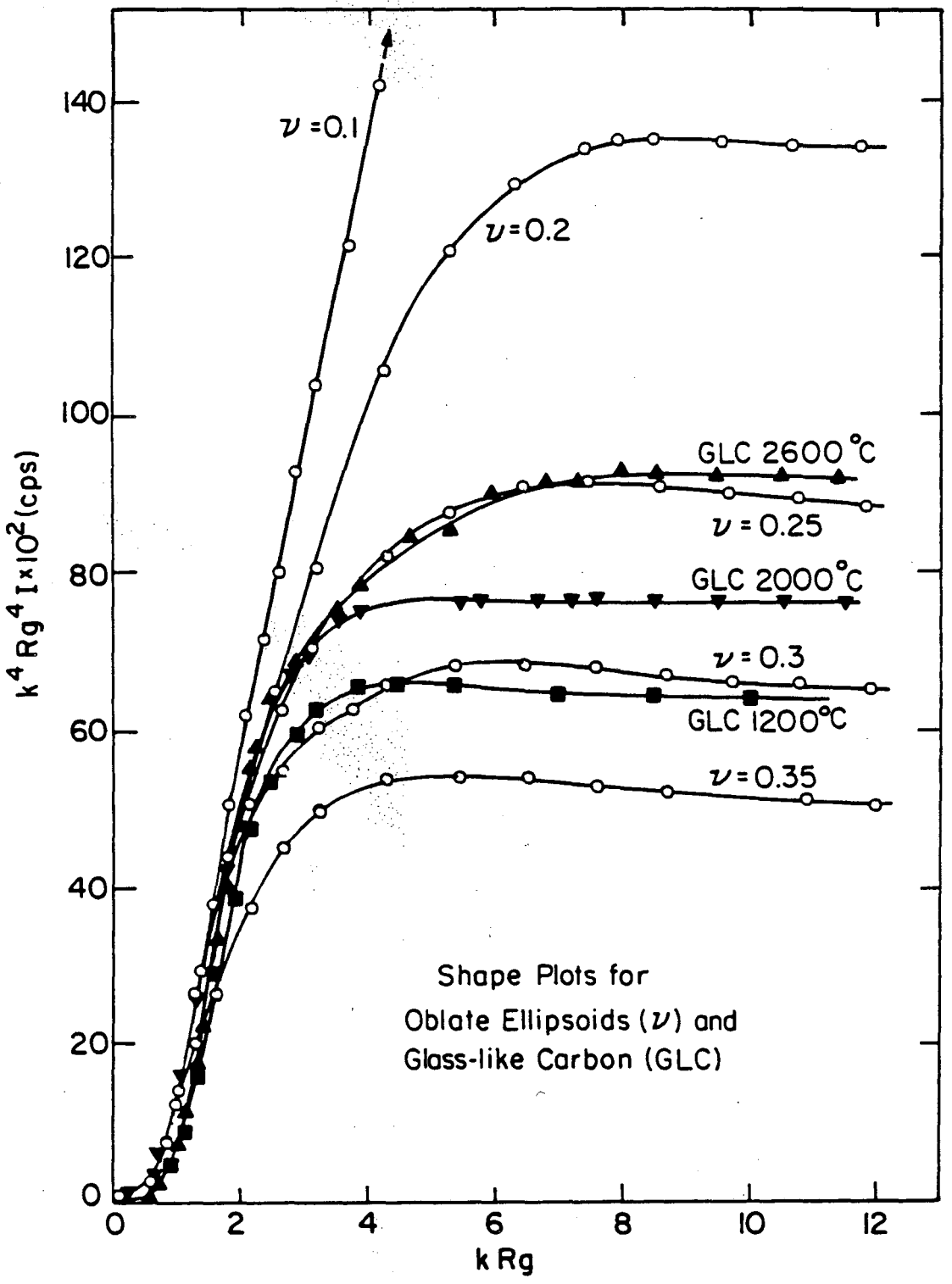

Fig. 4.4.K

XBL8410-7464

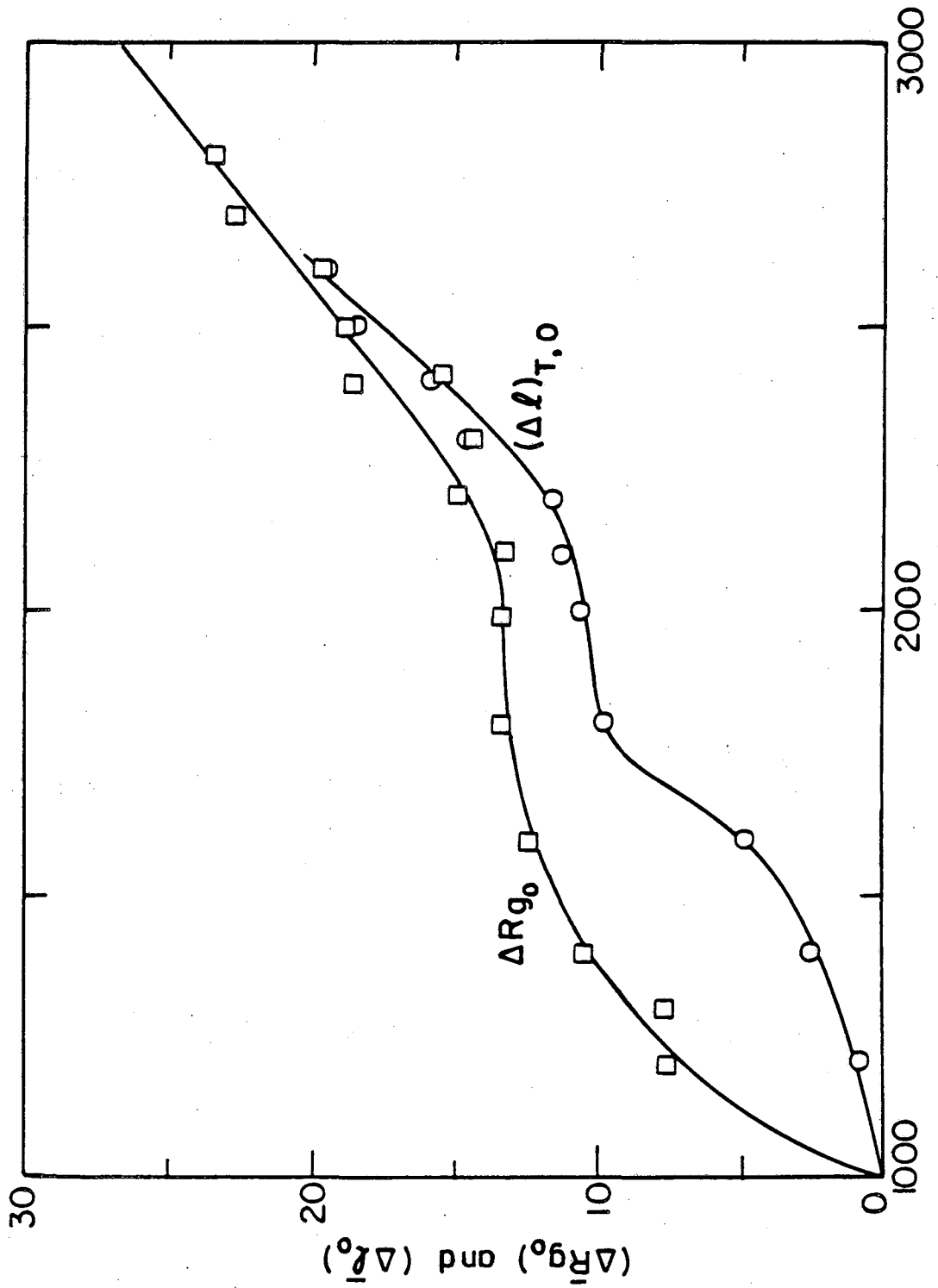
30
20
10
0
1000
2000
3000
HTT (°C)
$(\Delta \bar{R}g_o)$ and $(\Delta \bar{\ell}_o)$
ΔRg_o
$(\Delta \ell)_{T,o}$
XBL 8410-7465

Fig. 4.5.A

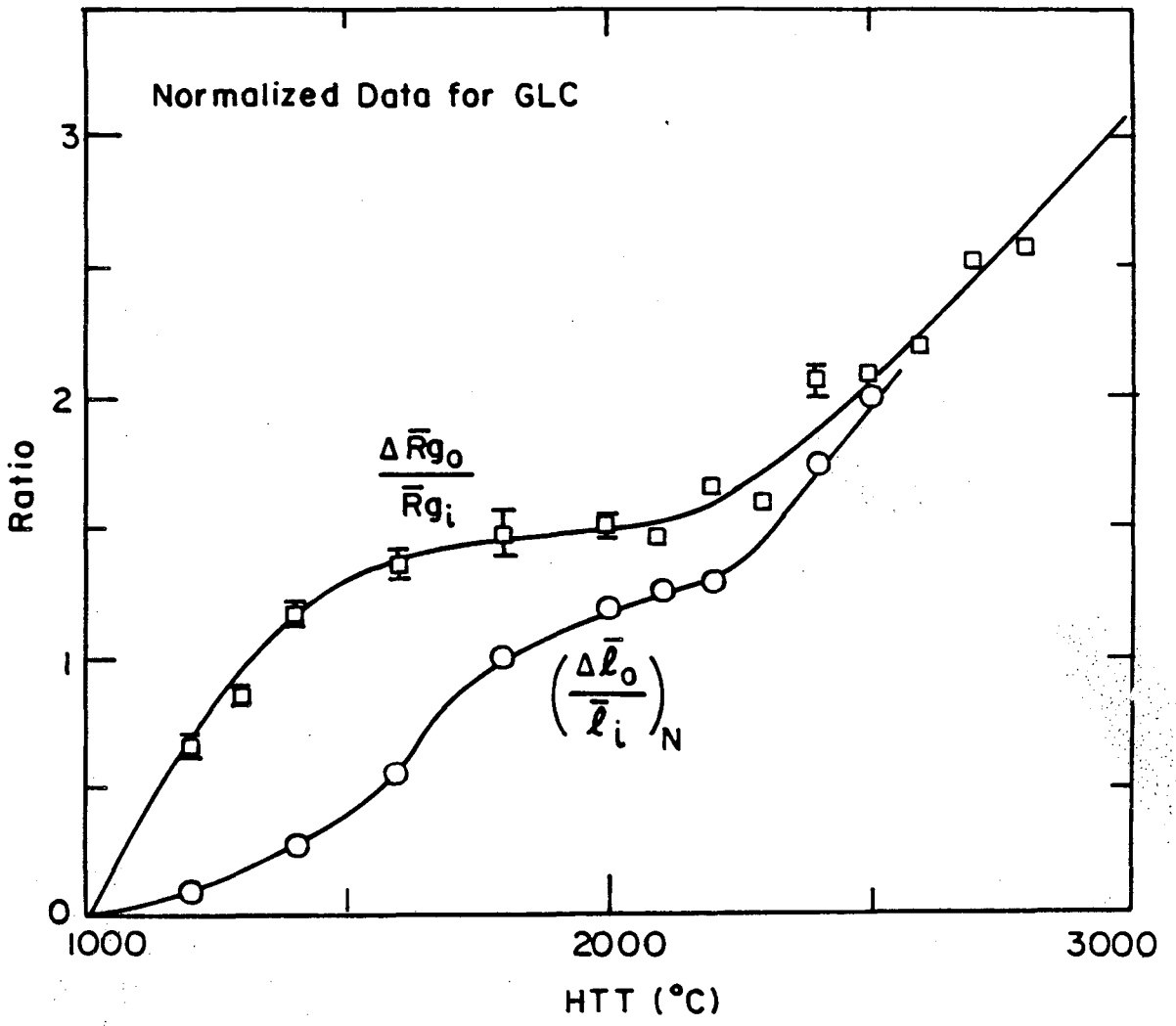

Fig. 4.5.B

XBL8410-7466

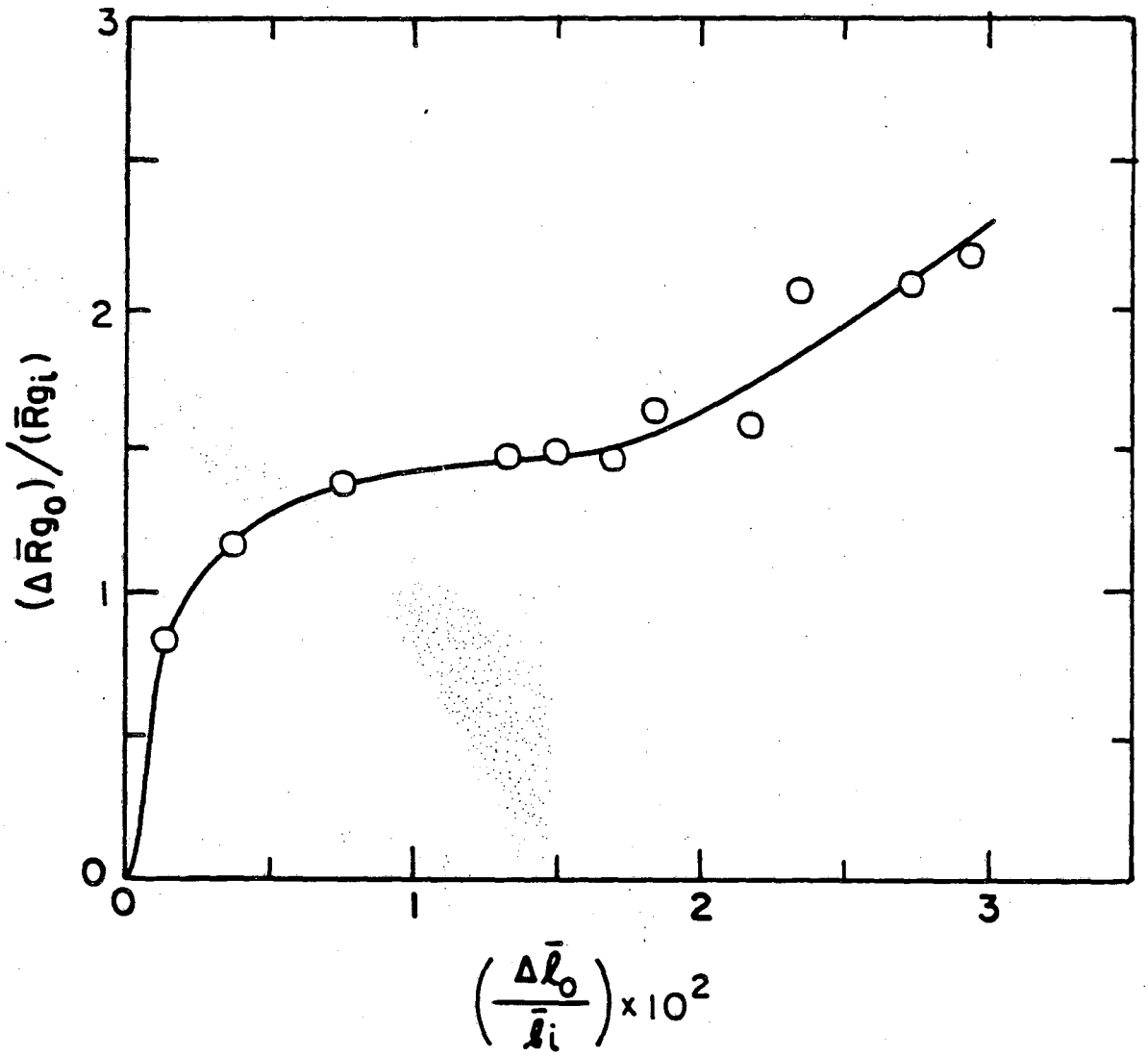

XBL8410-7467

Fig. 4.5.C

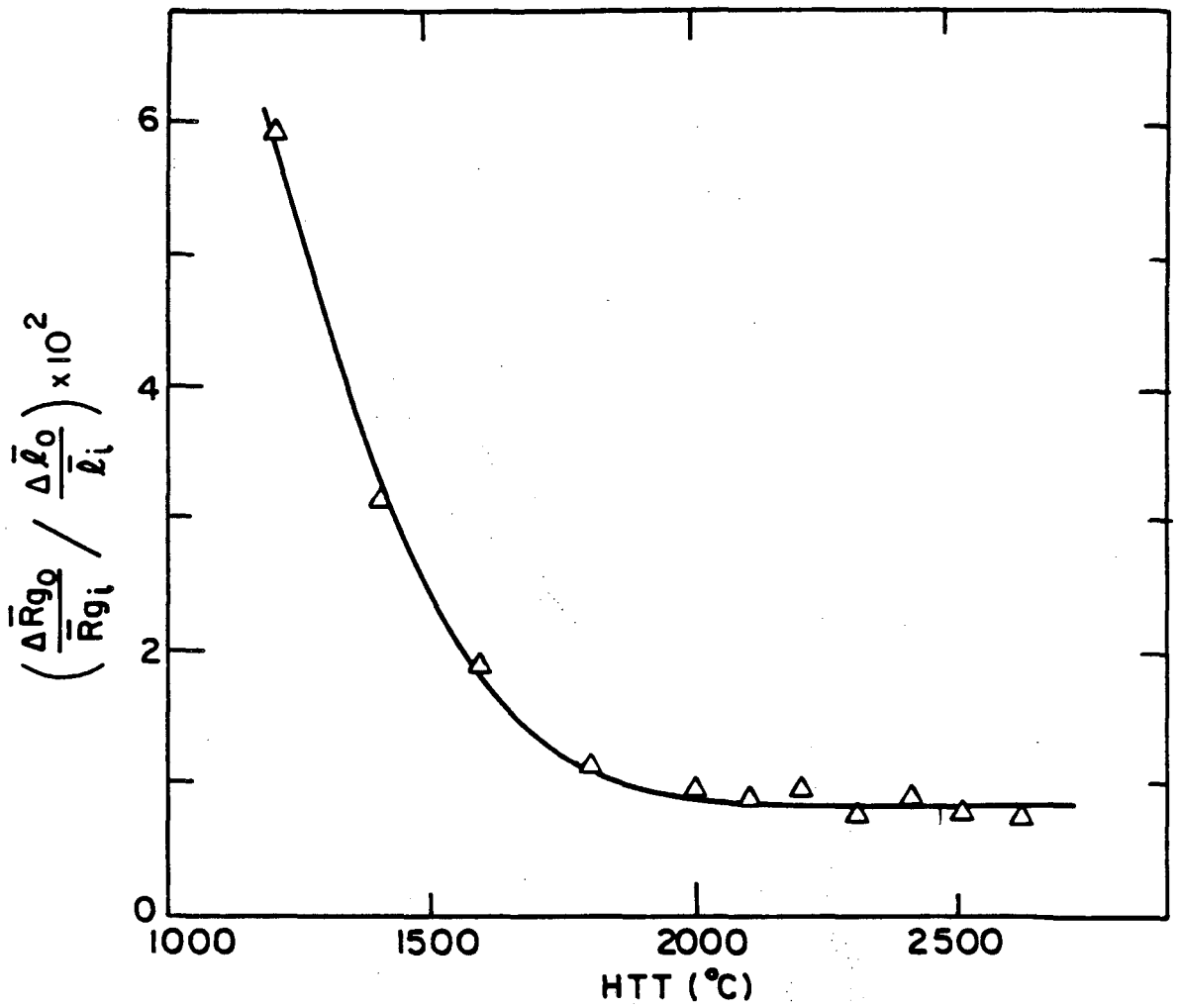

Fig. 4.5.D

XBL 8410-7468

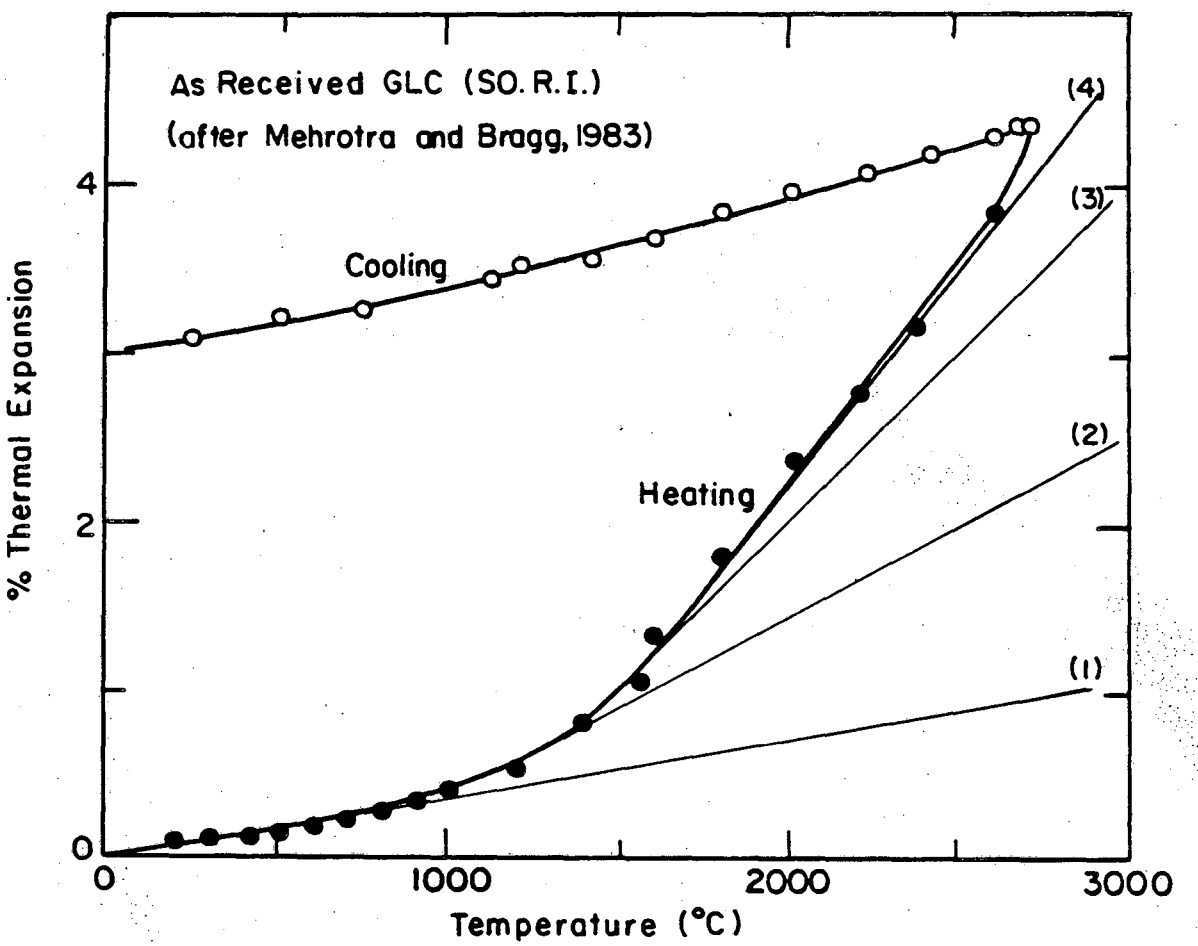

Fig. 5.8.A

XBL 8410-7469

LAWRENCE BERKELEY LABORATORY
TECHNICAL INFORMATION DEPARTMENT
UNIVERSITY OF CALIFORNIA
BERKELEY, CALIFORNIA 94720